Ferromagnetic Artificial Pinning Centers in Superconducting Niobium-Titanium Wires

A Dissertation
Presented to the Faculty of the Graduate School
of
Yale University
in Candidacy for the Degree of
Doctor of Philosophy

by
Nicholas David Rizzo

Dissertation Director: Professor Daniel E. Prober

May 1997

Abstract

Ferromagnetic Artificial Pinning Centers in Superconducting Niobium-Titanium Wires

Nicholas David Rizzo

1997

Ferromagnetic artificial pinning centers were used in superconducting NbTi wires to achieve a large critical current density (J_c) in a magnetic field. The wire processing was developed to make four wires that contained nanometer-sized arrays of Ni or Fe pins inside micron-sized filaments of a $Nb_{0.36}Ti_{0.64}$ alloy. The optimum pin size and spacing for maximum J_c was approximately 5 nm and 30 nm, respectively. A ferromagnetic pin volume of only 2% Ni produced J_c's (e.g., 2500 A/mm^2 at 5 T, 4.2 K) that were comparable to those of other NbTi wires that have pin volumes ranging from 12% to 20%. Therefore, ferromagnetic artificial pins are more effective than nonmagnetic pins for a given volume percent.

Saturation Magnetization measurements on the wires showed a correlation between an increase in the amount of Ni remaining ferromagnetic in the wires and an increase in J_c. These results suggest wires with larger volumes of Ni may have even higher J_c's. The critical temperature (T_c) of the best wire with Ni pins was only slightly depressed ($T_c \approx 8.6$ K) from the measured bulk value for $Nb_{0.36}Ti_{0.64}$ ($T_c \approx 9$ K), suggesting that proximity effects from the Ni are not severe.

Wires with small superconducting filament diameters (0.3 μm) displayed enhanced J_c at low fields ($B \leq 5$ T) that was attributed to pinning at the filament surfaces. Finally, for wires with large filaments, the optimum bulk pinning force (F_p) dependence on B was well described by the form $F_p \propto b^{1/2}(1-b)$ where $b = B/H_{c2}$ and H_{c2} is the upper critical field of the superconductor. This form is interpreted as a general result of the large optimum pin spacings in our APC wires.

This thesis research was the result of a collaboration between Yale University and IGC-Advanced Superconductors (Waterbury, CT).

Table of Contents

Acknowledgments

List of Abbreviations

List of Figures

List of Tables

Chapter 1. Introduction 1

1.1. Review of NbTi Wires with Nonmagnetic APCs 4

1.2. Ferromagnetic Artificial Pinning Centers 7

1.3. Organization of this Thesis 9

Chapter 2. Pinning in Type-II Superconductors 11

2.1. Ginzburg-Landau Theory 11

2.1.1. Magnetic Fields 12

2.1.2. Vortices 13

2.1.3. The Structure of a Vortex 14

2.1.4. Vortex Line Energy 14

2.1.5. Interactions Between Vortices 15

2.1.6. The Elasticity of the Vortex Lattice 16

2.2. Theory of Vortex Pinning 18

2.2.1. Core Pinning by Voids 19

2.2.2. Core Pinning by a Nonmagnetic Normal Metal 19

2.2.3. Core Pinning by a Magnetic Metal 21

2.2.4. Bulk Pinning Force (F_p) vs. Magnetic Field (B) for Core Pinning 25

2.2.5. Surface Pinning 26

2.2.6. Bulk Pinning Force (F_p) vs. Magnetic Field (B) for Surface Pinning 27

2.2.7. Ferromagnetic Dipole Pinning 29

Chapter 3. Wire Processing 32

3.1. NbTi-Pin Assembly 32

3.1.1. Interstitial Pins 33

3.1.2. Gun-Drilled Pins 34

3.1.3. Definition of Pin Spacing 35

3.2. Restack and Draw Processing 36

3.2.1. Bonding 42

3.2.2. Wire Geometry 44

3.3. Ni vs. Fe 45

3.4. Split Billets and other Gun-Drilled APCs 47

Chapter 4. Measurement Techniques 49

4.1. Critical Current (I_c) Measurements 49

4.1.1. High Current Cryostat at Yale 49

4.1.2. Magnets at Yale 52

4.1.3. Insert for Critical Current Measurements in High Magnetic Fields 52

4.1.4. Critical Current Measurements at IGC 54

4.2. Saturation Magnetization (M_{sat}) Measurements 55

4.3. Transport Measurements on Single Filaments 57

4.3.1. Single Filament Sample Preparation 57

4.3.2. Variable Temperature Cryostat 58

4.3.3. AC and DC Measurement Techniques 60

Chapter 5. Experimental Results 61

5.1. Critical Current Density (J_c) and Bulk Pinning Force (F_p) 61

5.1.2. Bulk Pinning Force Comparison 65
5.1.3. Surface Pinning and Size Effects 67
5.1.4. Bulk Pinning Force Comparison between Ferromagnetic and Nonmagnetic Pins 69
5.2. Saturation Magnetization versus Pin Diameter 72
5.3. The Shape of F_p vs. B 75
5.4. Single Filament Measurements 78
5.4.1. Proximity Effect Reduction of Critical Temperature (T_c) and Upper Critical Field (H_{c2}) 80
Chapter 6. Conclusions 83
6.1. Summary of Results 83
6.2. Future APC Designs 84
6.3. Coda 87
Appendix A. Determining the Superconductor Volume Percentage and Pin Volume Percentage 89
Appendix B. Cleaning During Wire Processing 91
References 92

Acknowledgments

There have been many people who helped me in the completion of this thesis research. To them, I would like to express my sincere gratitude.

Foremost, I would like to thank Professor Daniel E. Prober, my thesis advisor. Dan has patiently instructed me in the ways of experimental research and challenged me to achieve excellence. I hope that in the future, I can continue to develop my research abilities as much as I have during my years in Proberlab. I would also like to thank Dr. Leszek R. Motowidlo of IGC-Advanced Superconductors. who effectively served as a second thesis advisor. Lesh guided and encouraged me in my research, and provided a valuable glimpse in to the world of industrial research and development.

I would also like to thank the members of my thesis committee -- Professors Robert Grober, Karin Rabe, Peter Parker, and Professor Robert Wheeler -- for taking the time to read this thesis and give helpful commentary. I am also grateful to Professor David C. Larbalestier of the University of Wisconsin at Madison for serving as an outside reader and providing useful commentary.

There have been many others at Yale who have provided significant assistance and guidance in my completion of this thesis research. Dr. Jian Q. Wang helped me to better understand vortex pinning theory and also provided great assistance in making and measuring the wires described in this thesis. Dr. James D. McCambridge provided me with a brief but valuable introduction to thin film processing and measurement. In addition, Jim usually made my time in the lab (Jimlab) more enjoyable with his philosophical discussion, loud music, and unique sense of humor. Dr. Sean Ling provided the initial motivation to use ferromagnetic pins and also was an excellent teacher of vortex pinning theory. I would like to thank the members of Proberlab, all of whom provided assistance to me at one time or another.

There was a large number of people at IGC-AS who also provided significant assistance. This thesis research would not have been possible were it not for the interest and support of Lesh, Mr. Bruce Zeitlin, and Dr. Robert Sokolowski. Mr. Gennady A. Ozeryansky provided invaluable advice and instruction on wire processing. Mr. Robert Hlava took many a SEM picture for me and gave valuable assistance in metallography. There were many others, too numerous to mention specifically, who helped me at IGC. To them, I am grateful.

Other friends and family also provided significant and much appreciated support to me during the completion of this thesis research. I would especially like to thank Bob Beloin for his insightful advice, friendship, and (on the practical side) for providing a place to stay during the writing of this thesis.

I want to express my deepest appreciation to my parents, Nicholas and Helen, and my sister, Karen, who have supported and encouraged me for many years, and without whom the completion of this thesis research would certainly not have been possible.

And finally, I want to thank my wife Kathryn, for her love and support. Because of her, my happiness at Yale was increased far more than the increase of J_c by ferromagnetic pins.

List of Abbreviations

a	vortex lattice spacing
A	the magnetic vector potential
A	Amp
APC	Artificial Pinning Center
b	reduced magnetic field = B/H_{c2}
B	magnetic field
bcc	body-centered cubic
C_{ij}	Elastic moduli of the vortex lattice
C_{11}	compression modulus
C_{44}	tilt modulus
C_{66}	shear modulus
d_{fil}	filament diameter (point to point of the hexagon for our wires)
D_n	single electron diffusion constant
d_p	pin spacing
d_{pin}	pin diameter (of ferromagnetic core for our wires)
d_{rod}	NbTi rod diameter
d_{straw}	straw diameter
d_s	superconductor thickness
E	electric field
E_{comp}	compression energy
E_{int}	Interaction Energy
E_{pin}	pinning energy
E_{el}	elastic energy of a vortex displacement
emu	electromotive unit
f_p	elementary pinning force
fcc	face-centered cubic

FM	ferromagnet
F_I	force of attraction to image vortex
F_M	force of repulsion from Meissner currents
F_p	bulk pinning force
G	Gauss
GL	Ginzburg-Landau
GN	giga-newton = 10^9 Newtons
$h(0)$	magnetic field at vortex center
H	applied magnetic field
H_c	thermodynamic critical field
H_{c1}	lower critical field
H_{c2}	upper critical field
H_{en}	critical vortex entry field
H_{ex}	critical vortex exit field
HIP	Hot Isostatic Pressure
H_p	field for maximum F_p
H_s	critical vortex entry for B=0
I_c	critical current
I_o	magnetic exchange energy
I.D.	inner diameter
IGC	Intermagnetics General Corporation
I-V	current-voltage
J_c	critical current density
J_M	Meissner screening current density
J_p	Josephson tunneling current density
J_s	vortex circulating supercurrent density
k	wavevector

m	magnetic moment
M_{sat}	saturation magnetization
n_p	volume number density of pins
n_p^A	areal number density of pins
NbTi	$Nb_{0.36}Ti_{0.64}$ (Nb47wt%Ti) alloy unless another composition is specified
n_s	number density of superconducting electron pairs
O.D.	outer diameter
PSI	pounds per square inch
R	resistance
$\boldsymbol{R}_n$	equilibrium position of the nth vortex
SEM	scanning electron microscopy
SNS	superconductor-normal metal-superconductor
SQUID	superconducting quantum interference device
t	reduced temperature = T/T_c
T	Tesla
T	Temperature
T_c	critical temperature
T_{c0}	critical temperature in absence of proximity effects
T_{Cu}	Curie temperature
V_{pin}	pin volume
wt%	weight percent
α	first GL parameter; hexagonal close-packed phase
β	second GL parameter; pin volume fraction
Δ	superconducting interaction energy or energy gap
ΔF_p	difference in F_p between small and large filament wires
ε	vortex line energy; elastic strain components for a distorted vortex lattice
κ	GL parameter = λ/ξ

λ	magnetic penetration depth
μ	magnetic moment
ξ	GL coherence length
ξ_N	normal metal coherence length
ρ	weight density
ρ_N	normal state resistivity
Φ_o	the fluxoid
ψ	GL order parameter
ψ_∞	Spatially constant order parameter in zero field

List of Figures

Fig. 1.1. Cross section of conventional NbTi wire 2

Fig. 1.2. Cross section of filaments for different types of APC wires 5

Fig. 2.1. The structure of an isolated vortex 15

Fig. 2.2. The superconducting order parameter near a ferromagnetic pin 24

Fig. 2.3. Flux distribution for alternating slabs of superconductor and insulator 29

Fig. 3.1. Cross section of Interstitial and Gun-Drilled APC wire filaments 34

Fig. 3.2. Schematic flow chart of the APC restack and draw process 38

Fig. 3.3. Cross section of first stack wires after extrusion 39

Fig. 3.4. Cross section of second stack wires: small filament and large filament 40

Fig. 3.5. Typical cross section of third and fourth stack wires 41

Fig. 3.6. Cross section of fourth stack wire near optimum pin spacing 41

Fig. 3.7. Comparison of Ni and Fe interstitial pin shape after extrusion and drawing 46

Fig. 3.8. Diagram showing orientation of slip systems for a textured bcc metal 46

Fig. 4.1. High current cryostat used to measure wire critical currents 51

Fig. 4.2. Insert for high field critical current measurements at 4.2 K 53

Fig. 4.3. Variable temperature cryostat for measurements on single filaments 59

Fig. 5.1. Critical current density vs. magnetic field (B) for wire C at various pin spacings (d_p) 62

Fig. 5.2. Bulk pinning force density (F_p) vs. (B) for wires A and B 63

Fig. 5.3. F_p vs. B for wires C and D 64

Fig. 5.4. F_p vs. d_p at various magnetic fields 66

Fig. 5.5. F_p vs. B for the four different wires at optimum pin spacing 66

Fig. 5.6. Difference between the F_p of wires A and B at comparable ferromagnetic pin spacings vs. the inverse of the filament diameter of wire B 68

Fig. 5.7. Comparison of F_p vs. B for wire C (2% Ni) with the F_p of other wires that have large nonmagnetic pin volumes 70

Fig. 5.8. Average saturation magnetization vs. ferromagnetic pin diameter 73

Fig. 5.9. F_p at 5 T vs. the volume percentage of Ni that remained ferromagnetic in wires A and C 74

Fig. 5.10. Model to determine quantitative form for the decrease in the number of pins on each vortex 76

Fig. 5.11. F_p vs. B for wire C at decreasing pin spacing 77

Fig. 5.12. Upper critical field vs. temperature for single filaments of wire C at large and optimum pin spacing 79

Fig. 6.1. F_p vs. B for small NbTi filaments surrounded by either Cu or Nb 85

List of Tables

Table 1.1. Summary of NbTi APC wires with nonmagnetic APCs 7

Table 3.1. Description of wires made containing ferromagnetic APCs 42

Table 5.1. Description of wires made containing ferromagnetic APCs 62

Table 5.2. Comparison of single filament and bulk NbTi properties 81

Table 5.3. Summary of results of T_c and H_{c2} measurements 82

Chapter 1. Introduction

To achieve a high critical current density (J_c) in a magnetic field, a bulk type-II superconductor must have defects or second-phase inclusions that pin the vortex lattice. The strongest pinning, or highest J_c usually occurs when the pin spacing is *roughly* comparable to the vortex lattice spacing a (e.g., a ~ 22 nm at 5 T). (As will be seen below, the optimum pin spacing for maximum J_c in NbTi can actually vary quite substantially, from 3 to 40 nm.) The nanometer spaced pins can be produced in NbTi -- the dominant material used for commercial magnet applications -- using either the conventional approach or artificial pinning centers (APCs).

The conventional approach, used by commercial wire manufacturers, is a thermomechanical process that consists of applying long heat treatments (typically 80 hours at 420 °C, [Meingast (1989a)]) to a wire containing a homogeneous $Nb_{0.36}Ti_{0.64}$ (Nb47wt%Ti) alloy and then drawing the wire. (The term 47wt% in Nb47wt%Ti refers to the weight percent of Ti in the alloy. For the remainder of this thesis, the term NbTi will refer to the $Nb_{0.36}Ti_{0.64}$ alloy, unless otherwise specified.) The heat treatments cause submicron-sized particles (~ 0.2 μm) of α-Ti to precipitate out of the homogeneous NbTi matrix. The wire is drawn to reduce these Ti pins to the optimum nanometer thickness (~ 1-2 nm) and spacing (~ 3-6 nm) [Meingast (1989a)] (see Fig. 1.1). The maximum Ti pin volume that can be precipitated is thermodynamically limited to approximately 24% [Lee (1994)]. Wire manufacturers have successfully made long lengths of optimized conventional wire that typically has $J_c \approx 2500$ - 3500 A/mm^2 in a magnetic field of 5 T and at a temperature of 4.2 K (See Fig. 5.7). As a comparison, cold-worked NbTi that contains only grain-boundaries as pinning centers has $J_c \approx 500$ A/mm^2 (4.2 K, 5 T) [Lee (1990)].

In recent years, researchers have also used artificial pinning centers (APCs) as pins in NbTi wires. In the APC approach, pins are placed in the NbTi at a macroscopic size

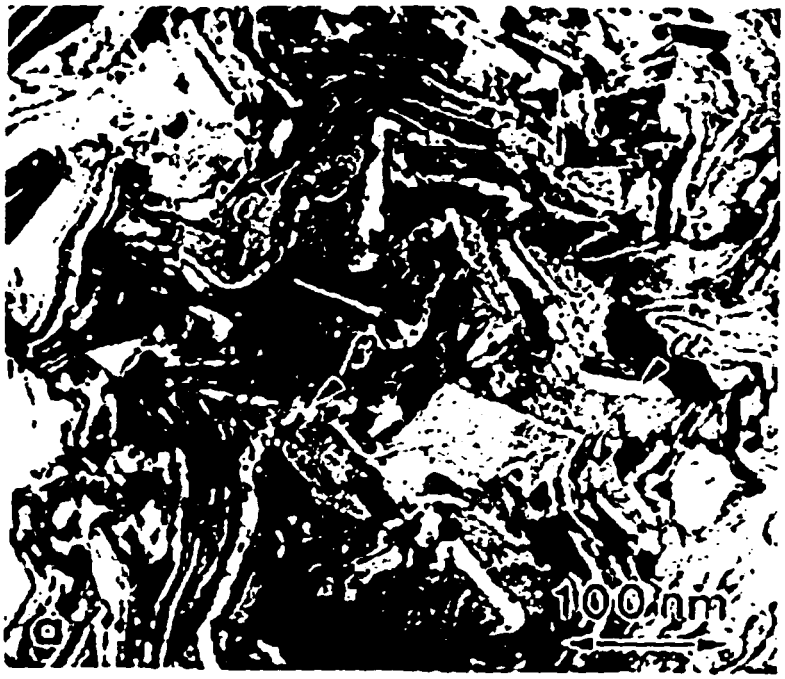

Fig. 1.1. *Cross section of conventional NbTi wire at optimum pin spacing for maximum J_c [from Cooley (1991)]. The lighter ribbon-like bands are the α-Ti pins and the darker areas are the superconducting NbTi.*

(~ mm) and then the composite wire of NbTi and pin material is repeatedly drawn to produce nanometer pin thickness and spacing. For example, one method of producing the initial APC composite is to stack rods of pin material along with rods of NbTi (see Fig. 3.1). Other types of pin shape and spatial distribution are discussed below, both of which make up what is referred to as the overall pin geometry. The subsequent drawing of the composite wire consists of a restack and draw process discussed in detail in chapter 3 (see Fig. 3.2 for a schematic of the APC process).

The APC approach has several advantages over the conventional process. First, there is actually a choice for the type of artificial pin material, while conventional pins are limited to α-Ti precipitates. In principle, an artificial pin material can be anything that has good ductility and a mechanical strength that is compatible with the strength of NbTi. Pin materials that have been used include Nb, Ti, or V [Dorofejev (1995)], Nb alloys [Cooley (1993), Heussner (1997a)] (all low-field superconductors), and Cu [Motowidlo (1992a)

(1992b)] (a normal metal). Second, the pin volume percentage can be varied over a greater range than in conventional wires. The APC volume percentage is only limited by the requirement of mechanical stability of the wire during drawing. In practice, the optimum pin volume has been found to be between 20% and 30%, although APC wires have been made that had a pin volume of up to 50% [Motowidlo (1992b)]. Finally, the pin shape and spacing can be better defined than the random distribution found in conventional wires. Presumably, a more uniform pin distribution would provide more uniform, stronger pinning in the APC wires. These advantages have made it possible to achieve much higher J_c's in APC wires than in conventional wires for magnetic fields $B \leq 6$ T. For example, an optimized APC wire with Nb pins has achieved a $J_c \approx 4600$ A/mm^2 at 5 T, 4.2 K [Heussner (1997b)].

APC wires are not without their disadvantages, however. Proximity effects from the nanometer-spaced artificial pins can reduce the upper critical magnetic field for superconductivity (H_{c2}) by several Tesla. (Homogeneous $Nb_{0.36}Ti_{0.64}$ has $H_{c2}(4.2\ K) \approx 11$ T. [Collings (1986)]) Therefore, the J_c of APC wires in high fields is also reduced because J_c goes to zero as the magnetic field B approaches H_{c2}. Conventional pins do not cause such a large reduction of H_{c2}. Therefore, while APC wires can have larger J_c's in low magnetic fields ($B \leq 7$ T), conventional wires usually have larger J_c's in higher fields because of their larger H_{c2}. The reasons for the absence of significant H_{c2} reduction by α-Ti pins are not presently understood.

An additional disadvantage of the APC process is that a much larger amount of wire drawing is necessary to reduce the large artificial pins to nanometer size and spacing. Work hardening of the pins and even hardening of the NbTi under such extreme strains can cause the wire to break up during drawing. In addition, even with ductile material, a poor overall wire geometry or a lack of bonding between the elements in the wire can also cause catastrophic wire breakage.

1.1. Review of NbTi Wires with Nonmagnetic APCs

In spite of these difficulties during processing, several APC wires have been made that had different types of pin materials and geometries. The APC concept was first successfully demonstrated by Dorofejev *et al.* (1985), who made NbTi wires that had Nb, V or Ti APCs in an island-type or barrier-type pin geometry (see Fig. 1.2a and 1.2b). The wire with 25% Nb pins in an island-type geometry achieved $J_c \approx 3500$ A/mm^2 (5 T, 4.2 K).

Motowidlo *et al.* (1992a, 1992b) also made NbTi wires that had Nb or Cu APCs in either island-type or barrier-type geometries. They achieved $J_c \approx 3000$ A/mm^2 (4.2 K, 5 T) for Nb, comparable to those obtained by Dorofejev. In addition, they made several different wires that had a range of Nb volume percentages and showed that the optimum pin volume was between 20 and 25%. The optimum pin spacing that produced maximum J_c in all the wires was calculated to be $d_p \approx 30$ nm. The wires had an H_{c2} between 8.5 and 9 T at optimum pin spacing, a significant reduction from the H_{c2} of bulk NbTi.

Cooley (1993) used $Nb_{0.98}Ti_{0.02}$ pins in an island-type design with a pin volume of 13% and achieved $J_c \approx 2700$ A/mm^2 (4.2 K, 5T). The optimum pin spacing was also found to be $d_p \sim 30$ nm and the reduction of H_{c2} was similar to that of the wires made by Motowidlo. He also performed an analysis of the pin microstructure using TEM and found significant distortion of the pin geometry at the optimum nanometer pin spacing. The round Nb pins had elongated into a planar shape. As will be discussed in chapter 3, this distortion is typical for materials that have a bcc crystal structure like Nb. With such distortion, the calculated pin spacings may not correspond to the actual pin spacing in the wires, but do reflect the average pin density.

Most recently, Heussner *et al.* (1997a, 1997b) have made NbTi wires that had Nb, $Nb_{0.96}Ta_{0.04}$ or $Nb_{0.95}W_{0.05}$ in island-type designs with a pin volume of 24%. The wire with 24% Nb achieved a $J_c \approx 4600$ A/mm^2 (5 T, 4.2 K), the highest yet observed for a

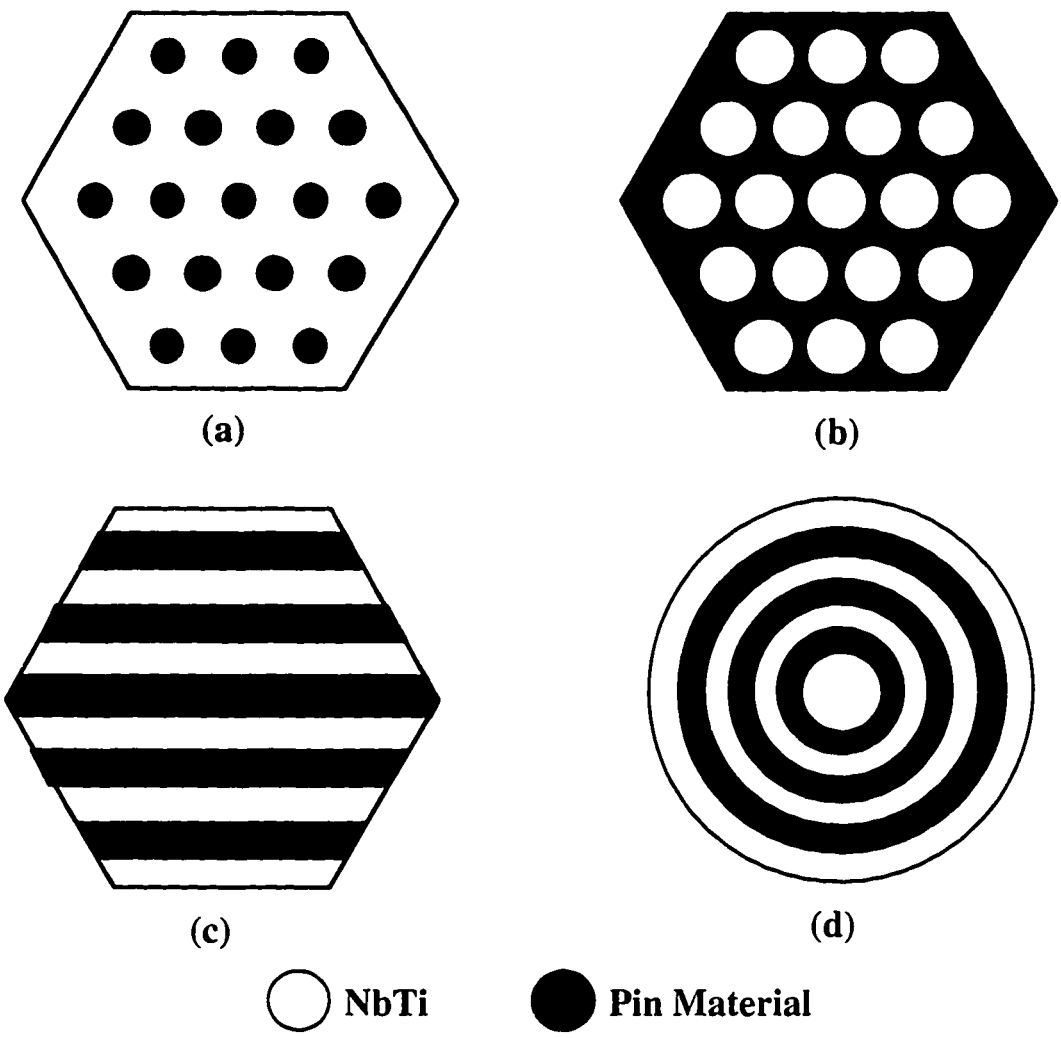

Fig. 1.2. *Cross-section of filaments for different types of APC wire: (a) Island-type (b) Barrier-type (c) Multilayer (Stacked plates) (d) Jelly roll. The optimum pin spacing for maximum J_c is approximately 30 nm. Actual wires usually contain thousands of these filaments stacked together so that the superconducting filament is several microns in diameter. The current travels along the filaments (into the page) and the magnetic field is perpendicular to the filaments (in the plane of the page).*

round NbTi wire. In this wire, the H_{c2} was again reduced to approximately 9 T. The optimum pin spacing was between 30 and 40 nm, and the usual pin distortions for nanometer-sized Nb pins were also observed.

Other APC wires have had different pin geometries, while still having Nb or Ti as the pin material. Matsumoto *et al.* (1994) stacked plates of NbTi and either Nb or Ti to

create a geometry similar to that of thin film multilayers [see Fig. 1.3c and McCambridge (1996)]. With a pin volume of 27% Nb, they achieved a $J_c \approx 4250$ A/mm^2 (5 T, 4.2 K). They also found H_{c2} was reduced to approximately 9 T for this wire. The optimum Nb layer spacing was calculated to be approximately 35 nm.

Rudziak *et al.* (1995) have used a jelly roll geometry (see Fig 1.2d), but with the innovation of using only pure sheets of Nb and Ti instead of a homogeneous NbTi alloy. The wire is heat-treated to cause partial diffusion that creates regions of superconducting NbTi while still having non-superconducting pin regions of Nb or Ti. The J_c's achieved by this approach have been comparable to that of conventional wire and there appears to be less reduction of H_{c2} compared to other APC wires. Interestingly, the optimum spacing of the layers was found to between 100 to 200 nm, indicating that the pinning mechanism may be different from that of the previously described APC wires. In any case, the large optimum layer spacing means that the wire requires less drawing than most APC wires and may be easier to make.

In another attempt to reduce the amount of drawing needed, Jablonski *et al.* (1994) attempted a powder metallurgy APC approach. In this approach, micron-sized NbTi and Nb powder were mixed together, sintered, and drawn. Less drawing was then required to reduce the micron-sized pins to nanometer size. Unfortunately, the J_c's obtained for 20% Nb pins were fairly low ($J_c \approx 2000$ A/mm^2 at 5 T, 4.2 K) and were attributed to the wide distribution of pin sizes intrinsic to this process.

The properties of all the different nonmagnetic APC wires discussed here are summarized in Table 1.1. Nb has been the most common pin material and the most successful in achieving a high J_c. The pin volume percentages have ranged from 12 to 50 %, with the optimum pin volume usually around 20 to 25 %. Various pin geometries have also been used, and are shown in Fig. 1.2. The optimum pin spacing for most of the wires was typically between 30 and 40 nm. At optimum pin spacing, the H_{c2} of the wires was

Table 1.1. *Summary of NbTi wires with nonmagnetic APCs. Boldface type in columns 1 through 3 designates the properties of the wire whose J_c is listed in column 4.*

Pin Material	Pin Type	Pin Volume %	J_c (A/mm^2) at 5 T, 4.2 K	Reference
Nb, Ti, V	Barrier, **Island**	**25**	3500	Dorofejev (1985)
Nb, Cu	**Barrier**, Island	12 to 50, **24**	3000	Motowidlo (1992a, 1992b)
$Nb_{0.98}Ti_{0.02}$	Island	13	2700	Cooley (1993)
Nb, $Nb_{0.96}Ta_{0.04}$, $Nb_{0.95}W_{0.05}$	Island	24	4600	Heussner (1997a, 1997b)
Nb, Ti	Multilayer	27	4250	Matsumoto (1994)
--	Jelly roll	--	3100	Rudziak (1995)
Nb	Powder metallurgy	20	2000	Jablonski (1994)

typically reduced to approximately 9 T. The range of J_c's achieved for these wires that had nonmagnetic APCs has been from 2000 A/mm^2 to 4600 A/mm^2 at 5 T, 4.2 K.

1.2. Ferromagnetic Artificial Pinning Centers

This thesis is a report on the properties of NbTi wires that contain ferromagnetic artificial pins. As will be shown, a pin's strength can depend on its ability to suppress superconductivity. Because a ferromagnet strongly suppresses superconductivity, even a small ferromagnetic region can be a strong pin. The coherence length for superconductivity penetrating into a ferromagnet is very short ($\xi_{Ni} \sim 1$ nm), compared to that for nonmagnetic pin materials ($\xi_{Cu} > \xi_{Ti} \sim \xi_{Nb} \sim 15$ nm) (See chapter 2 for a discussion of coherence lengths.) Therefore, a small ferromagnetic pin can significantly depress the order

parameter and create a large *effective* pin volume; this effect of ferromagnetic pins was observed in our wires.

There has been little previous research on the pinning properties of a ferromagnet in a type-II superconductor. Alden and Livingston (1966) produced and measured the J_c of a HgIn superconducting alloy that contained dispersions of small Fe particles (d_{Fe} ~ 10 nm). Their main conclusion was that the J_c, i.e., the pin strength depended on the magnetization direction of the of the Fe particles. Koch and Love (1969) measured the J_c produced by micron-sized ferromagnetic Gd particles in Nb and found no significant difference from the J_c produced by nonmagnetic (or weakly paramagnetic) Y particles of similar size in Nb. They concluded that Gd and Y were equally effective as pins. Yetter *et al.* (1982) measured the J_c produced by periodic antiferromagnetic Cr layers in thin films of superconducting PbBi. (As will be shown in Chapter 2, an antiferromagnet is expected to have pinning properties that are similar to that of a ferromagnet.) They found that Cr layers as thin as 2 nm significantly increased J_c compared to that of an unlayered film. These results are discussed in more detail in later chapters and contrasted with the results of this thesis.

More recently, Cooley *et al.* (1995) attempted to make two NbTi APC wires with ferromagnetic pins: one was made using the powder metallurgy approach and contained 10% Ni, another had an island-type geometry and contained 15% Fe. Neither wire was processed to the optimum pin size and spacing due to mechanical failures during drawing; Consequently, the J_c's were quite low.

For this thesis research, I developed the necessary wire processing (in close consultation with G.A. Ozeryansky and Dr. L.R. Motowidlo) and made wires containing nanometer-sized arrays of Ni or Fe artificial pins inside micron-sized filaments of a $Nb_{0.36}Ti_{0.64}$ alloy. Ni pins in NbTi produced J_c's (e.g., 2500 A/mm^2 at 5 T) that were comparable to those of conventional NbTi wire and other APC wires. However, the Ni pin volume was only 2%, in contrast to the optimum nonmagnetic pin volumes of 20-30%.

Therefore, ferromagnetic pins are more effective than nonmagnetic pins for a given volume percent. These results and those for other wires that I made containing Ni pins, also indicate that wires with larger volumes of Ni may have even larger J_c's.

This work was the result of a research collaboration between Yale University and Intermagnetics General Corporation - Advanced Superconductors (Waterbury , CT). The wires described here were made at the IGC-AS factory by myself and Dr. J.Q. Wang. We measured the wire properties at IGC, at Yale, and at other Universities.

1.3. Organization of this Thesis

The remainder of this thesis is organized into five chapters. Chapter 2 begins with a general description of the properties of type-II superconductors in magnetic fields using the Ginzburg-Landau theory. The latter half of the chapter is a discussion of the two types of pinning mechanisms that are relevant for interpreting our experimental results: core pinning by a ferromagnet and surface pinning at the interface between a superconductor and a normal metal. Surface pinning mechanisms are used to explain the size effects on J_c observed for the wires made that had NbTi filaments with submicron diameters.

Chapter 3 includes a general description of the wire processing. The two methods of combining the pins with the NbTi are described: the standard gun-drilled technique and the novel interstitial approach that was developed as part of this research. At the heart of the discussion is the standard restack-and-draw process. Also discussed is how that standard process was modified to improve APC wire drawability. The different behavior of the Fe and Ni pins during drawing is discussed and explained in terms of the different slip systems operating in the two materials. Finally, SEM and optical micrographs of the wire cross-section during processing are shown.

In chapter 4, the experimental techniques and the apparatus that were used to measure the wire properties are described. The standard four point measurements of the

wire J_c's using high current cryostats in magnetic fields from 1 to 9 T are described. In addition, the transport measurements that were made on single filaments of the wire using a variable temperature cryostat are described. The magnetization measurements that were made on the wires using a SQUID magnetometer are also discussed.

In chapter 5, the results of the wire measurements are given and interpreted. After accounting for filament size effects, the differences in pin strength between the wires are interpreted using the results of the J_c and magnetization measurements. The J_c's of these wires are compared with those of other APC wires that had nonmagnetic pins, in order to determine the relative effectiveness of ferromagnetic pins. In addition, the dependence of the pinning force on field in APC wires is explained using some simple arguments about the effective pin density in the wires.

Finally, in chapter 6, the conclusions of this thesis are summarized and some possible designs for future APC wires are proposed; the designs are based primarily on the observed trends for the J_c dependence on ferromagnetic pin volume and the J_c dependence on the superconducting filament size.

Chapter 2. Pinning in Type-II Superconductors

This chapter begins with a brief review of the essential theoretical concepts needed to discuss pinning in type-II superconductors. The subject is discussed using the phenomenological Ginzburg-Landau (GL) theory closely following the description given in Tinkham (1996). The chapter concludes with a basic discussion of vortex-vortex and vortex-pin interactions. The reasons for the effectiveness of ferromagnetic pins are discussed, as well as the mechanisms of core pinning in general. Surface pinning mechanisms are also discussed, along with a simple model that will be used later to understand size effects in our NbTi wires with small filaments. Finally, the possibility of a magnetic dipole pinning interaction between the vortices and the ferromagnetic pins in our wires is examined.

2.1. Ginzburg-Landau Theory

The basic postulate of GL theory [Ginzburg (1950)] is that the free energy density of the superconductor can be expanded in a series of the form:

$$f_s = f_{n0} + \alpha|\psi|^2 + \frac{\beta}{2}|\psi|^4 + \frac{1}{4m}\left|\left(\frac{\hbar}{i}\nabla - \frac{2e}{c}\mathbf{A}\right)\psi\right|^2 + \frac{h^2}{8\pi} \qquad (2.1)$$

where f_{n0} is the normal state free energy density, α and β are temperature dependent coefficients, m is the electron mass, e is the electron charge, c is the speed of light, $\mathbf{A}$ is the vector potential and h is the local magnetic field. ψ is the order parameter in the superconductor and $|\psi|^2 \propto n_s$, where n_s is the density of superconducting electron pairs in the superconductor. GL theory is strictly valid only near T_c (the superconducting critical temperature), where ψ is small and for slow spatial variations of ψ and field $\mathbf{A}$, but it does still give a good description of the superconducting behavior even at temperatures well below T_c. In zero magnetic field and for constant ψ, the minimum of f_s occurs at ψ^2 =

$-\alpha/\beta \equiv \psi_\infty^2$; Evaluating Eq. 2.1 at ψ_∞ gives the condensation energy associated with the superconducting state:

$$f_s - f_{n0} = \frac{-\alpha^2}{2\beta} = -\frac{H_c^2}{8\pi} \tag{2.2}$$

using the definition of the thermodynamic critical field H_c. As will be shown below, the condensation energy plays a crucial role in pinning.

In the case of boundary conditions that impose fields, currents, or gradients, ψ adjusts to minimize the overall free energy, so that a variation of the volume integral of Eq. 2.1 with respect ψ and **A** yields the two GL differential equations:

$$\alpha\psi + \beta|\psi|^2\psi + \frac{1}{4m}\left(\frac{\hbar}{i}\nabla - \frac{2e}{c}\mathbf{A}\right)^2\psi = 0 \tag{2.3}$$

$$\mathbf{J} = \frac{c}{4\pi}\nabla\times\mathbf{h} = \frac{e\hbar}{2mi}\left(\psi^*\nabla\psi - \psi\nabla\psi^*\right) - \frac{2e^2}{mc}|\psi|^2\mathbf{A} \tag{2.4}$$

where **J** is the supercurrent density in the superconductor. If the first GL equation (2.3) is considered in the absence of fields and without the nonlinear terms then:

$$\nabla^2\psi = \frac{4m\alpha}{\hbar^2}\psi = \xi^2\psi \tag{2.5}$$

so that $\psi \sim e^{-x/\xi}$. Thus, the characteristic length over which ψ may change is the GL coherence length ξ. For temperatures T near T_c, $\alpha(T) \sim 1-t$, then $\xi^2 \sim 1/(1-t)$, where $t = T/T_c$. In $Nb_{0.36}Ti_{0.64}$, $T_c \approx 9$ K and $\xi(4.2\text{ K}) \approx 5$ nm [Collings (1986)].

2.1.1. Magnetic Fields

In the case of a spatially constant ψ, the behavior of magnetic fields in the superconductor are described by the London equation:

$$\mathbf{h} = -c\nabla\times\left(\frac{m}{n_s e^2}\mathbf{J}\right) \tag{2.6}$$

Then a combination of Maxwell's equation $\nabla\times\mathbf{h} = \frac{c}{4\pi}\mathbf{J}$ with Eq. 2.6 (and using a vector identity) gives:

$$\nabla^2\mathbf{h} = \frac{4\pi n_s e^2}{mc^2}\mathbf{h} = \frac{1}{\lambda^2}\mathbf{h} \tag{2.7}$$

so that $h \sim e^{-x/\lambda}$ and the magnetic field is found to decay over a characteristic distance λ, the magnetic penetration depth. Near T_c, $\lambda^2 \sim 1/(1-t)$. For $Nb_{0.36}Ti_{0.64}$, $\lambda(4.2K) \approx 200$ nm [Collings (1986)].

Taking the ratio of λ to ξ yields the temperature independent GL parameter $\kappa = \lambda/\xi$. As will be discussed next, the behavior of a superconductor in magnetic fields dramatically depends on its value of κ. In $Nb_{0.36}Ti_{0.64}$, $\kappa \sim 40$-50 [Meingast (1988)].

2.1.2. Vortices

For $\kappa \lesssim 1$, the superconductor is type-I and will exclude magnetic fields up to H_c, when the superconductor then goes into the normal state. For $\kappa \gtrsim 1$, the superconductor is type-II and there is a negative surface energy which allows the entry of magnetic flux in a field $H \geq H_{c1}$ (the lower critical field). In this case, the superconductor will divide into normal and superconducting regions, allowing flux to penetrate. Qualitatively, the negative surface energy at the region boundary arises because as λ gets longer, the positive diamagnetic screening energy is reduced and as ξ gets shorter, the recovery of ψ away from the normal region of flux penetration occurs more quickly, providing more condensation energy. Since the surface energy is negative, the superconductor will divide so as to maximize the boundary surface area. The size of each normal region reaches a quantum limit when it encloses a magnetic flux of $\Phi_0 = hc/2e$; Φ_0 is known as the fluxoid. These normal flux-containing regions are called fluxons or vortices.

2.1.3. The Structure of a Vortex

The first GL equation (2.3) can be solved to find ψ near an isolated vortex. The result is shown in Fig. 2.1. As expected, ψ is zero in the center and recovers to its equilibrium value over a distance ξ. The vortex is often described quite well as having a

normal core of area $\pi\xi^2$. For $\kappa >> 1$, ψ can be approximated as a constant except over the small area of the normal core, so that the London equation (Eq. 2.6) can still be used to determine the field distribution in the superconductor which gives:

$$h(r) = \frac{\Phi_0}{2\pi\lambda^2} K_0\left(\frac{r}{\lambda}\right) \tag{2.8}$$

where K_0(r) is a zero-order Hankel function. The limiting forms for h(r) are:

$$h(r) \approx \frac{\Phi_0}{2\pi\lambda^2}\left(\frac{\pi}{2}\frac{\lambda}{r}\right)^{\frac{1}{2}} e^{-\frac{r}{\lambda}} \qquad r \to \infty \tag{2.9}$$

$$h(r) \approx \frac{\Phi_0}{2\pi\lambda^2}\left[ln\left(\frac{\lambda}{r}\right)\right] \qquad \xi << r << \lambda \tag{2.10}$$

As expected, the exponential decay of the field occurs over a characteristic distance λ. Using Maxwell's equation $\nabla \times \mathbf{h} = \frac{c}{4\pi}\mathbf{J}$, the field gradient implies that a supercurrent circulates around the vortex with spatial dependence $J_s \sim \partial h(\mathrm{r})/\partial r \sim 1/r$. As will be shown, the circulating supercurrent is the main contributor to the line energy of vortices, as well as the interactions between them.

2.1.4. Vortex Line Energy

Associated with each vortex is a line energy per unit length ε_1, given by (for $\kappa >> 1$):

$$\varepsilon_1 = \frac{1}{8\pi}\int\left(h^2 + \lambda^2|\nabla \times \mathbf{h}|^2\right)dS \tag{2.11}$$

where the first term is the field energy and the second term is the energy of the circulating supercurrents. A comparison of the two terms using the expression for h(r) from Eq. 2.10 shows the second is larger by a factor of order $(\kappa/\ln\kappa)^2$. Evaluating the integral (Eq. 2.11) gives:

$$\varepsilon_1 = \left(\frac{\Phi_0}{4\pi\lambda}\right)^2 ln\,\kappa = \frac{H_c^2}{8\pi} 4\pi\xi^2 ln\,\kappa \tag{2.12}$$

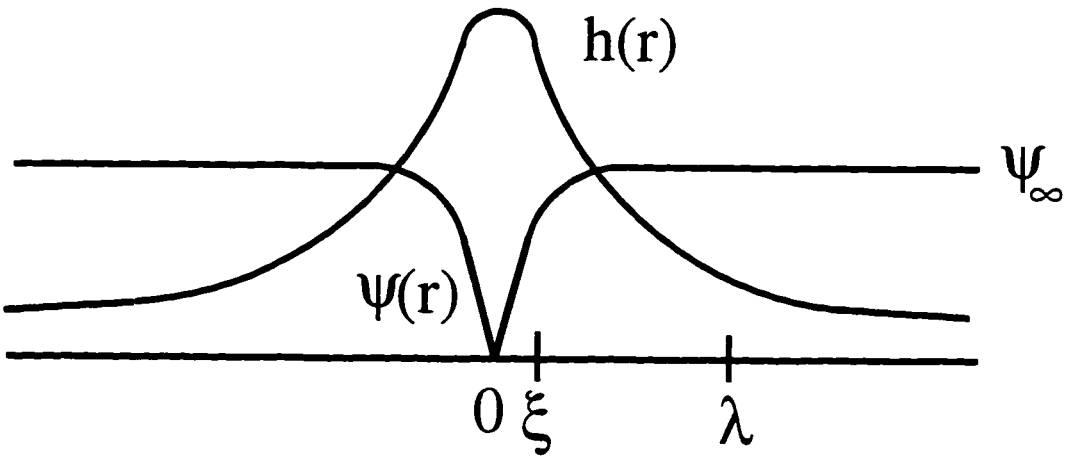

Fig. 2.1. *The structure of an isolated vortex for κ ~ 5 [after Tinkham (1996)]. The order parameter ψ(r) goes to zero in the center, producing a normal core of radius ξ. The magnetic field h(r) decays approximately exponentially over a distance λ.*

This result shows that the energy associated with the supercurrents is of the same order of magnitude as the condensation energy lost in the core. It is not surprising, therefore, that pinning mechanisms that use the core energy (core pinning) and those that involve the supercurrent energy (surface pinning) can be of similar strength.

2.1.5. Interactions between Vortices

The supercurrents circulating around a vortex give rise to an interaction between vortices. The Lorentz force on one vortex is $f = J_s \times \Phi_0/c$, where J_s in the supercurrent density due to another vortex a distance r away. The force between the vortices is repulsive for parallel flux and attractive for anti-parallel flux. From the force, the corresponding interaction energy (E_{int}) between the vortices can be derived:

$$f = \frac{\Phi_0}{c} J_s(r) = -\frac{\Phi_0}{4\pi}\frac{\partial h(r)}{\partial r} = -\frac{\partial E_{int}}{\partial r} \quad \Rightarrow \quad E_{int} = \frac{\Phi_0}{4\pi} h(r) = \frac{\Phi_0^2}{8\pi^2\lambda^2} K_0\left(\frac{r}{\lambda}\right) \quad (2.13)$$

These formulas generalize to the case of many vortices in a straightforward manner.

When there are many vortices in the superconductor (without defects), the vortices form a lattice because by symmetry, the net force on each vortex is then zero. The lattice spacing a is given by the requirement that each unit cell enclose a fluxoid $\Phi_0 = Ba^2$, so that the lattice spacing decreases as B increases. The upper critical field for superconductivity (H_{c2}) can then be understood as field for which the vortices are so close that the normal cores begin to overlap; At this point $a \approx 2\xi$, then $H_{c2} \approx \Phi_0/4\xi^2$. (A more exact calculation yields $H_{c2} = \Phi_0/2\pi\xi^2$.) In $Nb_{0.36}Ti_{0.64}$, $H_{c2}(4.2\ K) \approx 11$ T [Collings (1986)].

2.1.6. The Elasticity of the Vortex Lattice

A displacement of a vortex from its equilibrium position in the lattice will have an associated energy cost and the vortex will then experience a restoring force. For small displacements, linear elasticity theory (i.e., the harmonic approximation) can be used to describe the interaction between vortices and calculate the energy cost for deformations of the vortex lattice [Brandt (1977a)].

The displacement field $s(z)$ of a deformed lattice is defined as [Brandt (1977a)]:

$$s_n(z) = r_n(z) - R_n = Re\, s_0\, exp(ik \bullet R_n) \qquad (2.14)$$

where $\boldsymbol{r}_n(z)$ and $\boldsymbol{R}_n$ are the distorted and undistorted positions of the nth vortices, respectively. Also, $\boldsymbol{s}_0$ is a constant vector and $\boldsymbol{k}$ is the wavevector of the periodic displacement field. An actual displacement field may have a range of $\boldsymbol{k}$, but here only one Fourier component is considered for simplicity. The strains associated with the displacement field are ε_i, where i ranges from 1 to 6 corresponding to the coordinate combinations xx, yy, zz, yz, xz, and xy, respectively. The strains are derived from $s(z)$ by the following relation [Landau (1986)]:

$$\varepsilon_{\alpha\beta} = \frac{1}{2}\left(\frac{\partial s_\alpha}{\partial x_\beta} + \frac{\partial s_\beta}{\partial x_\alpha}\right)$$

where α and β designate Cartesian coordinates.

For a given lattice displacement and the associated strains, the elastic energy cost of the displacement is [Landau (1986), Brandt (1977a)]:

$$E_{el} = \int \frac{1}{2} C_{ij} \varepsilon_i \varepsilon_j dV \approx \frac{1}{2} C_{ij} s_0^2 k^2 V \tag{2.16}$$

where C_{ij} are the elastic moduli of the vortex lattice and V *is* the volume of the distortion. For systems with hexagonal symmetry, there are only five nonzero moduli. In addition, strains along the direction of the vortices (ε_3 for vortices in the z direction) do not cost energy, since the line tension does not depend on the vortex length [Campbell (1972)]. As a result, it can be shown that there are only three independent non-zero moduli: C_{11} -- the compression modulus, C_{44} -- the tilt modulus, and C_{66} -- the shear modulus [Landau (1986), Campbell (1972)].

The general form for the elastic moduli can be obtained by considering the interaction force between vortices [Tinkham (1996)]. For example, the Lorentz force density on a vortex from the supercurrent of another vortex a distance r away is $F \approx J_s B \sim B/r$, then $C \sim dF/dr \sim B/r^2 \sim B^2$, where we have used $r \sim a$, the vortex lattice spacing. More rigorous calculations by Brandt (1986) [see also Brandt (1977a, 1977b)] using linearized GL theory showed that the elastic moduli also depend on the characteristic wave vector $\boldsymbol{k}$ of the lattice displacement. His results are (for $\kappa >> 1$):

$$C_{11}(k) \approx C_{44}(k) \approx \frac{B^2}{4\pi} \left(\frac{1}{1 + (k\lambda')^2} \right) \tag{2.17}$$

$$C_{66} \approx \frac{H_{c2}^2}{32\pi\kappa^2} b(1-b)^2 \left(1 - 0.58b + 0.29b^2\right) \tag{2.18}$$

where $b = B/H_{c2}$ and $\lambda' = \lambda/(1\text{-}b)^{1/2}$. Therefore, the elastic moduli decrease as $C \sim 1/k^2$ for $k >> 1/\lambda$, i.e., for displacement wavelengths much less than the penetration depth. In this case, the energy cost for tilt or compression does not increase with k, but rather $E_{el} \sim Ck^2 \approx$ constant. The lattice is then said to be "softer", because the elastic energy cost is less than it would be if the $k = 0$ values of the elastic moduli were used to calculate E_{el}.

2.2. Theory of Vortex Pinning

Although the net force on a vortex from all the other vortices in the lattice is zero, an external current density will cause a nonzero Lorentz force per unit length of $\boldsymbol{f} = \boldsymbol{J} \times \Phi_0/c$ on each of the vortices , or a Lorentz force density of $\boldsymbol{F} = \boldsymbol{J} \times \boldsymbol{B}/c$. If the vortices move, they will induce an electric field $\boldsymbol{E} = \boldsymbol{B} \times \boldsymbol{v}/c$, where $\boldsymbol{v}$ is the vortex velocity [Tinkham (1996)]. ($\boldsymbol{E}$ can be derived by a Lorentz transformation from the rest frame of the vortices to the lab frame where they have a velocity $\boldsymbol{v}$.) Power is then dissipated since $P \propto \boldsymbol{E} \cdot \boldsymbol{J}$, and energy is lost. So, a type-II superconducting NbTi wire can carry large currents in large magnetic fields without energy dissipation only if the vortices are strongly "pinned" down. The pins hold down the vortices until the Lorentz driving force density exceeds the bulk pinning force density F_p that holds down the vortices. At the critical current density J_c (the maximum current density for zero voltage), the two forces are equal and we have $F_p = \boldsymbol{J}_c \times \boldsymbol{B}/c$. Thus, by measuring J_c, F_p is determined.

There are several different ways to pin down vortices to produce a finite F_p. In general, any spatial inhomogeneity that locally changes the bulk superconducting properties will act as a pin. Local changes in ξ, λ, κ, or H_c cause changes in the line energy and core energy of the vortex so that some areas become positions of lower energy for the vortex. (See Campbell (1972) for a discussion of the different types of pinning not discussed here). Different types of pins include voids, insulating or normal metal inclusions, weaker superconductors (H_{c2}(pin) < H_{c2}(superconductor)), surfaces and grain boundaries.

Most pins interact with vortices in one of two ways: either through the condensation energy lost in the vortex core (Core pinning) or through the kinetic energy of the circulating supercurrents (Surface or Magnetic pinning.) A special case of pinning interaction that does not directly depend on the pin changing the superconducting parameters is a dipole attraction (or repulsion) between vortices and ferromagnetic pins. These pin mechanisms are discussed in more detail below.

2.2.1. Core Pinning by Voids

As discussed previously, a vortex can be approximately described as having a normal core of area $\pi\xi^2$, so that a condensation energy per unit length of magnitude $(H_c^2/8\pi)(\pi\xi^2)$ is lost due to the presence of the vortex in the superconductor [Tinkham (1996)]. If the vortex line passes through a void (or insulator) of dimension $d_{pin} \leq 2\xi$ instead of passing through the superconductor, then part of the core condensation energy is regained by the superconductor. The void of volume V_{pin} will then pin with a force:

$$f_p \approx \frac{\Delta E}{\Delta r} = \left(\frac{H_c^2}{8\pi} V_{pin}\right)\frac{1}{\xi} \approx \left(\frac{H_c^2}{8\pi} d_{pin}^3\right)\frac{1}{\xi} \qquad (2.19)$$

where the term in parentheses is the condensation energy difference (ΔE) between when the vortex sits on the pin and when the vortex sits away from the pin in the superconductor. The characteristic distance over which the energy change occurs was taken to be ξ, since the vortex size is approximately 2ξ. For the maximum core condensation energy to be regained by the superconductor, the pin diameter (d_{pin}) should be approximately equal to the diameter of the normal vortex core, so that $d_{pin} \sim 2\xi$. In practice, voids, or equivalently, insulators are not used as pins in NbTi wires, since their presence inside the NbTi would drastically decrease the wire ductility and make the present process of drawing long lengths of wire impractical.

2.2.2. Core Pinning by a Nonmagnetic Normal Metal

The most common type of pin material is a ductile nonmagnetic normal metal or weak superconductor (H_{c2}(pin) << H_{c2}(superconductor)). For these pins, the order parameter can be finite in the pin, particularly when the pin size is less than the coherence length for penetration of superconductivity into the pin. For example, metals that have been used as pins in NbTi wires are Nb or Ti (weak superconductors) and Cu (clean

normal metal) [Dorofejev (1985), Motowidlo (1992)]. Cold-worked Nb that has $H_{c2} \approx 1$ T implies $\xi_{Nb} \approx 15$ nm. The coherence length for bulk Ti can be estimated from the formula for the normal metal coherence length (ξ_N) in the dirty limit [Collings (1986)]:

$$\xi_N(T) = \left(\frac{\hbar D_N}{2\pi k_B T}\right)^{\frac{1}{2}} = 5.46\times10^{-7}\left(\rho_N \gamma T\right)^{-1/2} \qquad (2.20)$$

where D_N is the single electron diffusion constant, ρ_N is the normal state resistivity in units of $\mu\Omega$ cm, γ is the electronic specific heat coefficient in units of erg/cm^{3}K^2, so that the formula gives ξ_N in units of cm. Using $\rho_{Ti} \sim 5$ $\mu\Omega$ cm [Heussner (1996)] and $\gamma_{Ti} = 3150$ erg/cm^{3}K^2 [Kittel (1986)], gives $\xi_{Ti}(4.2K) \approx 20$ nm $\geq \xi_{Nb}$. Similarly, it follows $\xi_{Cu} \geq \xi_{Nb}$, given the much smaller resistivity of bulk Cu compared to Ti at low temperatures [Fickett (1983)]. Therefore, thin pins of these materials ($d_{pin} \leq 2\xi \sim 10$ nm) will have substantial penetration of superconductivity.

In contrast to the negative condensation energy of a real superconductor, there is a positive condensation energy associated with the proximity-induced superconductivity in the normal pin that increases the free energy of the superconductor [Matsushita (1983)]. Thus, when a vortex sits on a nonmagnetic normal metal pin, the free energy is lower because of two effects. As for a void, the core condensation energy is regained by the superconductor. In addition, the normal vortex core destroys the superconductivity in the pin and the positive condensation energy is reduced to zero, lowering the free energy even further.

Matsushita (1983) estimated the magnitude of pinning expected for a nonmagnetic normal metal pin by approximating the positive condensation energy in the pin as $f \approx \alpha_n|\psi|^2$. In the case of a thin pin ($d_{pin} << \xi_N$), the order parameter is a constant $|\psi_\infty|^2$ across it and the pinning force will be:

$$f_p \approx \left[\left(\frac{H_c^2}{8\pi}\right)d_{pin}^3\right]\frac{1}{\xi} + \left[\left(\alpha_n|\psi_\infty|^2\right)d_{pin}^3\right]\frac{1}{\xi} \approx \left[\left(\frac{H_c^2}{8\pi}\right)d_{pin}^3\right]\frac{1}{\xi} + \left[\theta\left(\frac{H_c^2}{8\pi}\right)d_{pin}^3\right]\frac{1}{\xi} \qquad (2.21)$$

where $\theta \approx -\alpha_n/\alpha \approx \xi/\xi_N$ ($\theta << 1$ for NbTi with most pin materials). The first term is the usual pinning energy from having the vortex core sit on the pin rather than in the

superconductor. The second term is the additional energy gained when the vortex core drives the pin normal.

Upon comparing Eq. 2.21 to Eq. 2.19, it is seen that a thin normal metal is predicted to have roughly the same core pinning force as that of a void of similar size. As for a void, the pin width must be 2ξ to take full account of the condensation energy of the core. Therefore, the nonmagnetic pins must be large in size or large in number to provide a large pinning volume and, consequently, strong pinning in NbTi wires.

2.2.3. Core Pinning by a Magnetic Metal

In contrast to a clean nonmagnetic normal metal, a magnetic material (ferromagnetic or antiferromagnetic) has an extremely short coherence length. This property of magnetic materials can be understood by considering the interaction energy of an electron with a magnetic impurity: $E_{int} = I_0 (\boldsymbol{S}_e \bullet \boldsymbol{S}_i)$,where I_0 is the magnetic exchange energy, $\boldsymbol{S}_e$ is the spin of the electron, and $\boldsymbol{S}_i$ the spin of the magnetic impurity [de Gennes (1966)]. The superconducting electrons are pairs that have spins anti-aligned, so that the interaction energy has the opposite sign for each electron. Therefore, a lower value of magnetic energy would occur with a spin flip of one electron. Since the magnetic exchange energy ($I_0 \sim$ 100 meV) is much larger than the pairing interaction energy ($\Delta \sim$ 1 meV) [de Gennes (1966)], the *total* energy of the pair is also lower with a spin flip, which means that the electron pair will break apart. Hence, a magnetic impurity, or more generally, a magnetic material is a strong superconducting pairbreaker so that any order parameter in it will quickly decay over short distances, i.e., the coherence length is small. Radovic *et. al* (1988) used a quasiclassical theory of superconductivity to determine the general form for the coherence length in a ferromagnet :

$$\xi_{FM} = \left(\frac{4\hbar D_N}{I_0} \right)^{\frac{1}{2}} \tag{2.22}$$

Upon comparing to Eq. 2.19, it is clear $\xi_{FM} << \xi_N$ in general, since $I_0 >> \Delta \sim k_B T_c$.

The approximate values of the coherence lengths for several magnetic materials have been experimentally determined. Koorevaar *et al.* (1994) concluded that $\xi_{Fe} \approx 0.6$ nm; They measured the T_c of V/Fe thin film multilayers and found no change for Fe thicknesses greater than 0.6 nm (and constant V thickness), indicating that the superconducting V layers had already been decoupled from one another. (See chapter 5 for a discussion of T_c depression by a ferromagnet). Hauser *et al.* (1966) used theoretical fits to the data for T_c depression of Superconductor (Pb)/Ferromagnet bilayers and also found $\xi_{Fe} \approx 0.6$ nm and $\xi_{Ni} \approx 0.6$ nm. Using the same methods, they also determined the coherence length for Cr, an antiferromagnet, to be $\xi_{Cr} \approx 0.5$ nm.

With such a short coherence length, even a small ferromagnetic pin ($d_{pin} < 2\xi$) can significantly depress the order parameter and create a large effective pin volume. The order parameter will recover from near zero at the pin boundary to the bulk value of ψ_∞ within a distance ξ, so that the effective pin diameter is 2ξ. Thus, it is expected that a small ferromagnetic volume can pin as strongly as a large void or nonmagnetic volume.

As part of this research project, Dr. J.Q. Wang determined the behavior of the order parameter near a ferromagnetic pin using a quasiclassical approach based on the work of Radovic (1988) [See Wang (1997)]. Within this analysis, the order parameter is assumed to be small in the ferromagnet, so that its behavior is described by a linearized equation similar to the 1st GL equation (2.3):

$$\nabla^2 \psi(\vec{r}) = \frac{4i}{\xi_{FM}^2} \psi(\vec{r}) \tag{2.23}$$

Consider the case of an infinite cylinder of ferromagnet that has a diameter d_{pin} and is surrounded by a superconductor. This is a good model for the situation in our wires, where the ferromagnetic pins are rods that are continuous along the wire axis. Then in cylindrical coordinates, the solution to Eq. 2.23 for the order parameter in the ferromagnet is:

$$\psi(\vec{r}) = J_0\left(\frac{2e^{i\pi/4}|\vec{r}|}{\xi_{FM}}\right) \tag{2.24}$$

where J_0 is the zeroth-order Bessel function and $\boldsymbol{r}$ is the 2-dimensional radius vector. Because of translational and azimuthal symmetry, there is no explicit z or ϕ dependence in ψ. In the superconductor, ψ was assumed to satisfy 1st GL equation including the nonlinear term. The equation was solved numerically using Mathematica, subject to the simplifying assumption that ψ and its spatial derivative are continuous across the pin boundary. The order parameter was calculated and is shown in Fig 2.2 for three cases: a Ni pin of diameter 3 nm, a Ni pin of diameter 4 nm, and a Fe pin of diameter 4 nm. These dimensions were chosen because the ferromagnetic pin diameter in our wires with maximum J_c was calculated to be $d_{pin} \approx 4$ nm.

In the calculation, it was assumed that $\xi_{Fe} = 0.6$ nm and $\xi_{Ni} = 0.9$ nm. Although Hauser (1966) found $\xi_{Ni} \approx 0.6$ nm $\approx \xi_{Fe}$, the measurements by Koorevaar *et al.* (1995) of T_c depression in superconductor/ferromagnet multilayers clearly showed Fe to have a stronger pairbreaking ability than Ni. Therefore, we expect $\xi_{Ni} > \xi_{Fe}$. If it is assumed that the Curie Temperature of a ferromagnet (T_{Cu}) is proportional to its exchange energy I_0 [Kittel (1986)], Eq. 2.22 can be used to determine ξ_{Ni} relative to a given value of ξ_{Fe}. Using T_{Cu}(Ni) = 627 K, T_{Cu}(Fe) = 1043 K [Kittel (1986)] and ξ_{Fe} = 0.6 nm gives $\xi_{Ni} \approx (1043/627)^{1/2}\xi_{Fe} \approx 0.8$ nm, where the electron diffusion constant was assumed to be the same for Fe and Ni. Therefore, the assumption that $\xi_{Ni} = 0.9$ nm may be a slight overestimate, but serves to give greater contrast between the results for Fe and Ni pins.

In any case, the results in Fig. 2.2 show that the qualitative description of the behavior of the order parameter was correct. The small ferromagnetic pins create large effective pin volumes by pulling down the order parameter to near zero. The order parameter recovers over a distance ξ, giving an effective pin diameter of 2ξ. Note, however, that the order parameter can penetrate somewhat into the pins.

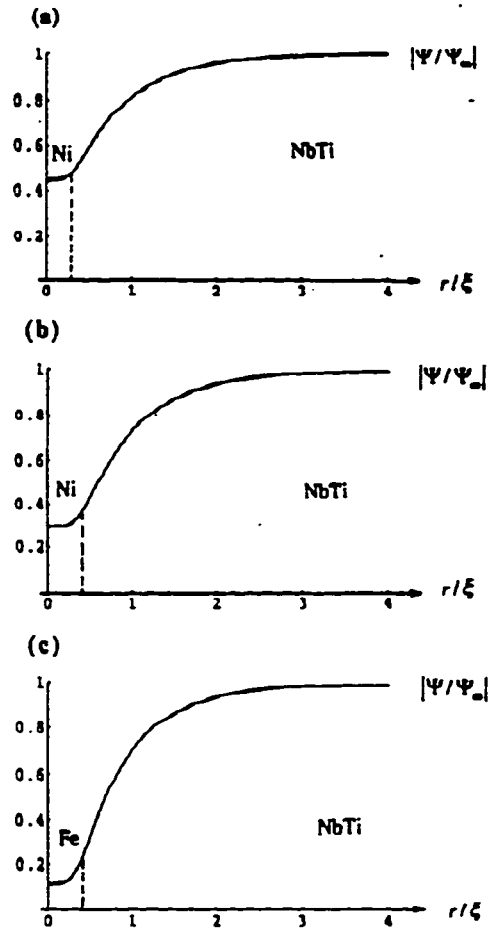

Fig 2.2. *The superconducting order parameter (normalized to ψ_∞) near a cylindrical ferromagnetic pin [from Wang (1997)]. (a) A Ni pin of diameter d_{pin} = 3 nm (b) A Ni pin of diameter d_{pin} = 4 nm. (c) A Fe pin of diameter d_{pin} = 4 nm.*

As will be seen, the experimental results of this thesis research are consistent with the theoretical description given above. It will be shown that a ferromagnetic pin volume of 2% Ni can provide a pin strength comparable to that for nonmagnetic pin volumes of 20-25%. In addition, the pin strength was found to depend on the amount of ferromagnet in the wires, indicating the pins had not completely suppressed the order parameter. These results are discussed in more detail in chapter 5.

2.2.4. F_p vs. B for Core Pinning

To determine the dependence of F_p on B, a direct summation of pin strengths is used [Collings (1986)]. In direct summation, the interaction between vortices is ignored so that each pin holds the vortices with its maximum strength f_p. Direct summation is expected to be a reasonable approximation for a system of strong core pins with spacing comparable to the vortex spacing [Meingast (1989a)]. Then the elastic energy costs for the vortex lattice to distort and adjust to the pinning centers will be small compared with the pinning energy. The bulk pinning force density can then be defined as $F_p = n_p f_p$, where n_p is the effective number of pins/unit volume, or equivalently $n_p =$ (vortices/unit area)(pins/unit vortex length). The vortices/unit area = $1/a^2 \propto B$, so that if the pins/vortex length is constant then $n_p \propto b$, where $b = B/H_{c2}$. For core pinning, one also has $f_p \propto (1-b)$, which reflects the loss of condensation energy as B approached H_{c2}. Thus, it is expected expect $F_p \propto b(1-b)$.

This form for the field dependence of F_p fits the experimental data quite well for conventional NbTi wires, but not for APC wires (see Fig. 5.7). In conventional wires, the optimum pin spacing (d_p ~ 3-6 nm) that gives maximum J_c is much smaller than the vortex lattice spacing for most fields. Then since the pin number density is much larger than the vortex density, one can assume that the average number of pins/unit vortex length is approximately constant, regardless of the vortex position. However, as will be shown, in APC wires the optimum pin spacings (d_p ~ 30 nm) are much larger (i.e., the pin number densities are smaller), so that the average number of pins per unit vortex length may not be constant in large fields; Therefore, n_p and the dependence of F_p on B will be different for APC wires than for conventional wires. This is discussed further in chapter 5.

The approximate magnitude of F_p expected for core pinning in NbTi APC wires can also be estimated using direct summation. In APC wires, the artificial pins are rods that are continuous along the length of the wire and are perpendicular to the vortices (See Fig. 3.1).

To estimate n_p, an exact matching of pin spacing (d_p) and vortex spacing is assumed, so that $n_p \approx 1/a^2(1/d_p) \approx 1/d_p^3$. A reasonable estimate is $d_p \approx 30$ nm, the typical optimum pin spacing in APC wires; this spacing for vortices corresponds to a field of $B \approx 3$ T.

To estimate f_p, the effective pin volume must be determined. The effective pin area perpendicular to the vortices is $A \approx (2\xi)d_{pin}$ for $d_{pin} \leq \xi$. The length of pin parallel the vortices is d_{pin}, so that for $d_{pin} \sim 2\xi$, the effective pin volume is $V_{pin} \approx d_{pin}^2(2\xi) \approx (2\xi)^3$. This V_{pin} is used in the estimate of f_p for a void (Eq. 2.19) along with the typical superconducting parameters for NbTi. Finally, a field dependence of $f_p \propto (1\text{-}b)$ is assumed as above, and f_p is evaluated at $B \approx 3$ T where the vortex lattice spacing $a \approx d_p$. These estimates for n_p and f_p give $F_p \sim 50$ GN/m^3. This simple estimate for F_p does give the same order of magnitude as the F_p observed in APC and even conventional NbTi wires.

2.2.5. Surface Pinning

In addition to core pinning by a normal metal inside the superconductor, pinning can also occur at the surface of a superconductor. As will be seen in chapter 5, this surface pinning mechanism can be used to understand the superconducting filament size-effects on the F_p of our wires. The following description of the vortex interaction with a surface (the surface barrier) follows the description given originally by Bean and Livingston (1966) and de Gennes (1966).

A vortex that is inside a superconductor and near the surface will experience two forces: an "image" force attracting the vortex towards the surface and a "Meissner" force repelling the vortex away from the surface. The attractive force results from the interaction of the vortex supercurrents with the surface. The boundary condition of zero current normal to the surface is satisfied by adding an image vortex (of opposite flux) outside the superconductor. The image vortex outside and the real vortex inside are equidistant from

the superconductor surface. The vortex will be attracted to its image with the interaction energy given approximately by Eq. 2.13. The attractive image force $F_I(r)$ is then:

$$F_I = -\frac{1}{2}\frac{\partial E_{int}}{\partial r} \approx \frac{\partial}{\partial r}\left[\left(\frac{\Phi_o}{4\pi\lambda}\right)^2 \ln\left(\frac{\lambda}{2r}\right)\right] = \left(\frac{\Phi_o}{4\pi\lambda}\right)^2 \frac{1}{r} \qquad (2.25)$$

where $r \geq \xi$, as required by the limits of the London approximation used to derive E_{int}. The additional factor of 1/2 in front of our previous expression for E_{int} arises because in this case, the integral to calculate the system energy is over the superconductor volume only, while the image vortex is located outside the superconductor [de Gennes (1966)]. The vortex will also be repelled from the surface by a Lorentz force due to the Meissner shielding current $J_M = c/4\pi(dH/dr) \approx c/4\pi(H/\lambda)e^{-r/\lambda}$, so that the repulsive force $F_M(r)$ is:

$$F_M = J_M \frac{\Phi_o}{c} = \frac{\Phi_o}{4\pi\lambda} H e^{-\frac{r}{\lambda}} \qquad (2.26)$$

The competition between these two forces creates the celebrated Bean-Livingston [Bean (1966)] surface barrier to vortex entry in the superconductor. If $B = 0$ inside the superconductor, a vortex will not enter the superconductor until the repulsive Meissner force can push the vortex past the attractive image force. The critical vortex entry field ($H_{en}(0)$) is the field when these two forces are equal. Equating the two forces at the superconductor surface gives $F_I(\xi) = F_M(\xi)$, so that $H_{en}(0) \approx \Phi_o/4\pi\lambda\xi \equiv H_s \approx H_c$. Clem (1974) extended the calculation to nonzero B, taking into account the effects of the vortices already in the superconductor as well as their corresponding image vortices. He found that $H_{en}(B) \approx (H_s^2 + B^2)^{1/2}$ for $B >> H_{c1}$. (This result was also derived independently by Ternovskii and Shekhata (1972)). Therefore, the surface barrier (or surface pinning) is still significant even in large fields well above H_c.

2.2.6. F_p vs. B for Surface Pinning

To determine what values of F_p are possible from this type of surface pinning, the results of Clem (1974) are quoted, who considered a model system of alternating slabs of

type-II superconductor and insulator. With the superconductor initially containing no magnetic flux and the field subsequently raised to H_0, the field will be distributed as in Fig. 2.3; the surface barrier at each interface causes a drop in the field ~ H_s. (The exit field is $H_{ex}(B) \approx B$.) Using the critical state model, the average critical current density of a slab corresponds to its critical field gradient through Maxwell's equation $J_c = c/4\pi(dH/dr)$; the result is

$$J_c(B) = \frac{c}{4\pi D}\left(H_{en}(B) - H_{ex}(B)\right) = \frac{c}{32\pi D}\frac{H_s^2}{B} \qquad (2.27)$$

for $B >> H_s$. For $D = 0.3$ μm (~ λ), $F_p = J_c B \approx 6$ GN/m^3. Therefore, it is expected that a surface barrier can provide significant pinning. In fact, pinning of this magnitude was observed in our wires that had an array of small NbTi filaments of diameter $d_{fil} \sim \lambda$ separated by Cu (see Fig. 3.3). The applicability of Clem's model system to our wires is further discussed in Chapter 5.

The surface barrier model discussed above is expected to apply only for large pins at large spacings ($d_p \geq \lambda$), where it is possible to define an equilibrium value for H and B in each slab away from the surface. However, it has recently been proposed that even thin ($d_{pin} \leq \xi$) elongated planar pins (such as α-Ti precipitates or grain boundaries) can also have a strong surface-type pinning interaction with vortices [Gurevich (1994), Cooley (1996)]. In this model the thin planar pins are considered to be similar to SNS Josephson junctions that have a tunneling critical current density J_p. As the vortex moves near the surface of the pin (assuming the vortex parallel to the planar surface of the pin), the circulating supercurrent density ($J_s \sim 1/r$) will exceed the J_p of the proximity coupled pins. Then the planar pin will behave similar to a surface and will block or divert the supercurrent, thereby creating the usual image force that attracts the vortex to the surface. However, in this case, there is no Meissner current repelling the vortex from the pin surface, since the pin is deep inside the superconductor. The pinning force is then approximately the force of image attraction (Eq. 2.25) which can provide J_c of the order of the depairing current density for $r \sim \xi$. This model is not expected to apply for the case of

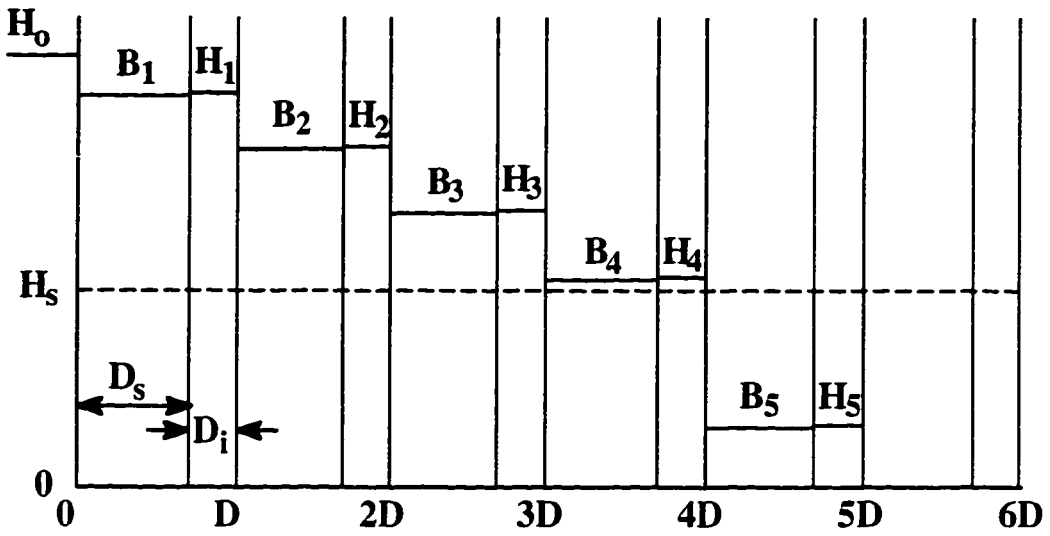

Fig. 2.3. *Flux distribution for alternating slabs of superconductor (thickness D_s) and insulator (thickness D_i) using the surface barrier model proposed by Clem (1972) described in the text.*

our ferromagnetic pins; the ferromagnetic pin diameter is approximately 4 nm at optimum size and probably cannot be considered as planar defect when compared to the characteristic vortex dimension λ.

2.2.7. Ferromagnetic Dipole Pinning

A third type of pinning may arise from the dipole attraction between a vortex and a ferromagnetic pin [Alden (1966), Autler (1972)]. The vortex lattice has gradients between the field maximum at the vortex center ($h(0)$) and the field minimum that is located halfway between the vortex cores. A vortex will then be attracted to (or repelled by) a pin of magnetic moment μ with a pin strength $f_p \approx \mu(\Delta h/\Delta r)$, where Δh is the magnitude of the change in the microscopic magnetic field over a distance Δr in the superconductor. This dipole pinning was directly observed by Alden and Livingston (1966) for Fe particles in a $Hg_{0.87}In_{0.13}$ alloy ($\kappa \approx 1$). They measured the difference between J_c with the moments of Fe particles aligned parallel to the vortex field (attraction), and J_c with the moments

antiparallel to the vortex field (repulsion). The moment could remain aligned against the applied field because the small Fe particles (d_{pin} ~ 10 nm) had large coercive fields (~ 500 G) compared to H_{c2} (2 K) ~ 400 G.

An experimental measurement similar to that of Alden and Livingston to observe this effect is not possible for our wires. The coercive field is nearly zero for the ferromagnetic pins in a field perpendicular to the wire axis, so that the pin moments cannot remain aligned antiparallel to the vortex field. However, the expected magnitude of F_p from dipole pinning in our wires can be estimated by using a simple theoretical model for f_p along with direct summation.

To estimate f_p, $\Delta h/\Delta r$ and the effective pin volume must be calculated. The variation Δh can be estimated at intermediate fields ($\Phi_0/\lambda^2 \leq B << \Phi_0/\xi^2$) by assuming a sinusoidal variation in $h(r)$ so that $\Delta h = 2(h(0) - B)$, which follows from the result that the spatial average of h(r) is equal to B [de Gennes (1966)]. The expressions for the free energy density of the superconductor can be used to determine $h(0)$ in terms of B [Tinkham (1996), de Gennes (1966)]:

$$F = \frac{Bh(0)}{8\pi} = \frac{B^2}{8\pi} + \frac{BH_{c2}}{16\pi\kappa^2} ln\left(\frac{\alpha H_{c2}}{B}\right) \tag{2.28}$$

where α is a numerical factor of order unity. Therefore:

$$\Delta h = 2(h(0) - B) \approx \frac{H_{c2}}{\kappa^2} ln\left[\alpha\left(\frac{H_{c2}}{B}\right)\right] \tag{2.29}$$

Using H_{c2} ~ 10 T and κ ~ 40 for NbTi at B = 3 T, gives Δh ~ 75 G, for example. The distance over which Δh occurs is taken to be $\Delta r \approx (1/2)a$. The effective pin volume of ferromagnet (needed to calculate $\mu \approx M_{sat} V_{pin}$) that interacts with the vortex is approximately $V_{pin} \approx (d_{pin})^2 a$. This is the volume for a cylinder of the ferromagnetic pin that has a length along the wire equal to the vortex lattice spacing a. Recall that the vortices are perpendicular to the symmetry axis of the pins.

To calculate F_p, a direct summation model is used as before, along with the assumption that the vortex spacing and pin spacing are approximately equal, so that $n_p \approx$

$1/d_p^3$. In our wires, a pin volume of 2% ferromagnet was used, so that $d_{pin} \approx 4$ nm at $d_p \approx$ 30 nm. Using these parameters in the expressions for n_p and f_p gives $F_p \sim 14$ GN/m^3 for Fe pins ($M_{sat} \approx 1700$ emu/cm^3) and $F_p \sim 4$ GN/m^3 for Ni pins ($M_{sat} \approx 500$ emu/cm^3), where the bulk values for M_{sat} at low temperature have been assumed. Note that the estimate of F_p for Fe pins is slightly smaller than that quoted by Wang *et al.* (1996). The smaller value follow from keeping closer track of the numerical constants in the calculation of Δh.

These results indicate that dipole pinning might be significant in an ideal case. However, as will be shown in chapter 5, the average M_{sat} of the pins in our wires is significantly reduced at $d_{pin} \approx 4$ nm: for Ni, $M_{sat} \sim (1/2)M_{sat}$(bulk) and for Fe, $M_{sat} \sim (1/5)M_{sat}$(bulk). Therefore, the effects from dipole pinning are probably not significant in the wires that have been made to date, but may be significant in future wires that have a larger volume of ferromagnet.

Chapter 3. Wire Processing

Frequently, a good geometry can fix a bad bond.

Never a good bond can fix a bad geometry.

-- Gennady's Law of the Wire Drawing.

This chapter describes the process that was used to make the NbTi wires that had ferromagnetic artificial pins and also describes the structure of all the wires that were produced. The processing was developed by myself, in close consultation with G.A. Ozeryansky of IGC-AS. The wires described here were made at the IGC-AS factory by myself and Dr. J.Q. Wang. I was the primary worker on the wires with Ni pins (wires A, B, and C) and Dr. Wang was the primary worker on the wire with Fe pins (wire D).

In general, the APC wire process consists of combining the pins with the NbTi at a macroscopic size, and then repeatedly drawing the composite of NbTi and pin material to reduce the pins to nanometer size and spacing. The heart of the process was a standard restack and draw procedure. To this process were added some non-standard procedures that were believed to significantly contributed to the success in making the wires. These procedures are discussed in detail below.

3.1. NbTi-Pin Assembly

Four wires were produced; each had an approximate ferromagnetic pin volume of 2%. Wires A, B, and D had a total pin volume of 3%: 2% Ni or Fe, with 1% Cu. Wire C had a total pin volume of 5%: 2% Ni with 3% Cu. (The Ni rods were 99.995% pure, the Fe rods were 99.9985% pure. By using such pure material, the possibility of impurities causing excessive work-hardening during cold-drawing was reduced.) Each pin consisted of the ferromagnetic core surrounded by a Cu sleeve. The sleeve was added by placing a

rod of ferromagnet inside a Cu tube and then either drawing or swaging the tube to the proper pin dimensions. The Cu sleeve was a diffusion barrier that prevented brittle intermetallics from forming between the ferromagnet and the NbTi during the hot processing of the wires (See below).

3.1.1. Interstitial Pins

A novel method was developed to put the pins into the NbTi matrix for wires A, B, and D. (This interstitial approach was originally conceived of by Dr. X.S. Ling.) Sixty-one NbTi rods were stacked in a hexagonal close-packed pattern and 96 pin rods were put in the interstitial spaces (see Fig. 3.1(a)). (The number of pins needed for a given number of NbTi rods is: $6(n\text{-}1)^2$ where n is the number of NbTi rods along one edge of the hexagon.) It can be shown from the geometry of Fig. 3.1(a) that $d_{pin} = ((4/3)^{1/2} - 1)d_{rod} \approx 0.15d_{rod}$. Thus, in theory the maximum possible interstitial pin volume percentage for these wires was approximately $100(96/61)(0.15)^2 \approx 3.5\%$. In reality, the maximum possible pin volume was slightly less than 3% because some clearance was necessary to slide the pins into the interstitial holes and the NbTi rods were not perfectly round. In any case, this interstitial approach was an elegant way to produce small pin percentages (1-3%) without the need to drill holes in the NbTi rods for the pins. This was an advantage since NbTi has a gum-like consistency even worse than that of Cu, so that machining it is quite difficult.

Of course, there are also some disadvantages to the interstitial approach. Clearly, the total pin volume is limited, and with a Cu diffusion barrier, the *ferromagnetic* pin volume is limited to about 2%. Also, after the rods were compacted, the pins were sometimes distorted into a triangular shape. This distortion may contribute to pin degradation at nanometer sizes (see Chapter 5).

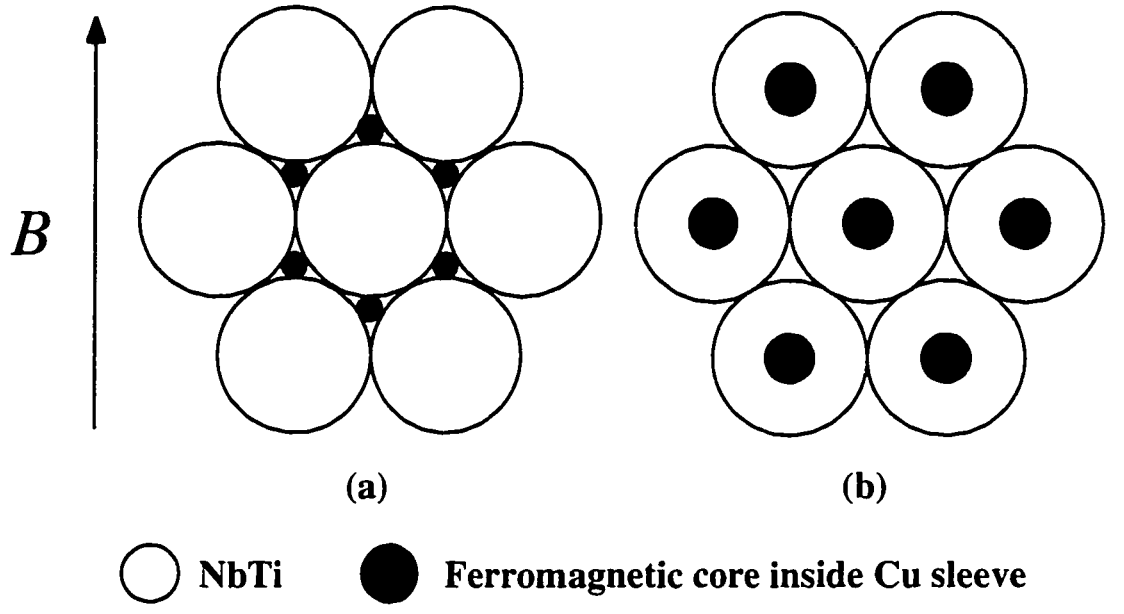

Fig. 3.1. *Cross section of APC wire filaments before extrusion. (a) Interstitial approach: pin fills interstitial hole between NbTi rods, (b) gun-drilled approach: pin fills gun-drilled hole in center of NbTi rod. Actual filaments contain 96 pins (wires B and D) or 5551 pins (wires A and C) along with the appropriate number of NbTi rods. The magnetic field B is perpendicular to the rod axis (in the plane of the page) and the current travels along the rod axis (into the page).*

3.1.2. Gun-Drilled Pins

For wire C, a hole was gun-drilled in a NbTi rod (3.8 cm O.D.) and the pin rod (Cu sleeve and Ni core) was put inside. This composite rod of NbTi and one pin was placed in a Cu can and hot isostatically pressed (HIPed) for 3 hours at a pressure of 30 kPSI and a temperature of 650 °C. After the HIP, the billet was pre-heated to 650 °C for 2 hours (at atmospheric pressure), and was then extruded with a 16:1 area reduction ratio. After cold-drawing to reduce its diameter further, the composite rod was cut into 91 pieces, the Cu (can) cladding was etched away, and the pieces were stacked in a hexagonal pattern (see Fig 3.1(b)). In this way, the number of pins in the first stack was approximately the same as in the first stack of the interstitial approach.

The gun-drilled approach has several advantages over the interstitial method. First, the pin percentage can be any value as defined by the size of the drilled hole. This allows the pin percentage to be varied over a large range to optimize J_c. Second, the pin maintains a rounder shape after extrusion. Thus, the pin can have a thicker Cu diffusion barrier without a decrease in the amount of ferromagnet, *and* the barrier is also more uniform. Our results indicate the rounder shape and thicker barrier have helped to enhance the pin strength (see chapter 5).

A disadvantage of using the gun-drilled approach (other than drilling holes in NbTi) is that an additional HIP and extrusion was necessary compared to the interstitial approach. Thus, the wire with gun-drilled pins took a few weeks longer to make. Because of this additional time required and because of the large amount of time necessary to produce any APC wires in general (in our case, at least 2 to 3 months), four types of gun-drilled APC wires were made at the same time using split billet designs. The other wires that were made and the split billet process are described in section 3.4.

3.1.3. Definition of Pin Spacing

Since the interstitial and gun-drilled pins have a different geometry, it is useful to define a pin spacing (d_p) using the areal pin number density (n_p^A) of the wire cross-section, rather than the specific pin geometry in the wires. By defining $n_p^A = 1/((\pi/4)(d_p)^2)$, d_p is then the diameter of a circle whose area is equal to the filament (NbTi and pin) cross-sectional area per pin. By defining d_p in this manner, wires that have the same d_p will have the same areal pin density, regardless of pin geometry. Thus, differences in F_p between the wires that have the same d_p are more likely to be the result of real differences in pin strength f_p, rather than the result of differences in pin density.

For the gun-drilled pins, inspection of Fig. 3.1(b) shows that $n_p^A = 1/((\pi/4)(d_{rod}^2))$, so that $d_p = d_{rod}$, where d_{rod} is the diameter of a single NbTi rod from the 1st stack of 91.

This result for d_p is not surprising since the nearest-neighbor pin spacing for the gun-drilled pins is equal to d_{rod}. For the interstitial pins, the unit cell of the filament cross-section is an equilateral triangle defined by lines that connect the centers of 3 rods that are in contact with each other. This triangle encloses the area of 1 pin and 3(1/6) = 1/2 the area of a NbTi rod so that $n_p^A = 1/((\pi/4)(0.5d_{rod}^2+d_{pin}^2)) \approx 2/((\pi/4)(d_{rod}^2))$. Therefore, for the wires with interstitial pins, $d_p = d_{rod}/(2)^{1/2}$. For either type of wire, d_{rod} (and hence d_p) is calculated using the total wire diameter and the superconductor volume percentage determined from a standard etch-and-weigh technique (See Appendix A).

3.2. Restack and Draw Processing

For all the wires, a standard restack and draw process was used to reduce the pins to nanometer size and spacing. The hexagonal bundle of rods was again placed into a Cu can, HIPed (3 hrs, 30 kPSI, 650 °C) and then extruded (2 hr pre-heat at 650 °C, 16:1 area reduction). Cold-drawing was used to reduce the diameter of the wire further. The wire was cut into pieces (usually 61) that were then restacked in another hexagonal pattern in one of two ways: with the Cu (can) cladding left on (wires B and D) or with the cladding chemically etched off (wires A and C). Thus, wires A and C had a superconducting filament diameter (d_{fil}) that was approximately 10 times larger than that of wires B and D. (A hexagonal stack of 61 rods has 9 rods across its point to point diameter.) Subsequent wire processing was identical for all wires. Each hexagonal bundle was placed in a Cu tube and again cold-drawn to reduce the wire diameter. Leaving the Cu (tube) cladding on, the restack and draw process was repeated two more times and ultimately the multifilamentary wire was reduced to a diameter as small as 0.1 mm. The pin spacing (d_p) in these smallest wires was approximately 8 to 10 nm.

A schematic flow chart of the restack and draw process described above is shown in Fig. 3.2. Pictures of the wire cross section at each stage of the process were taken using optical and SEM microscopy and are shown in Figs. 3.3-3.6.

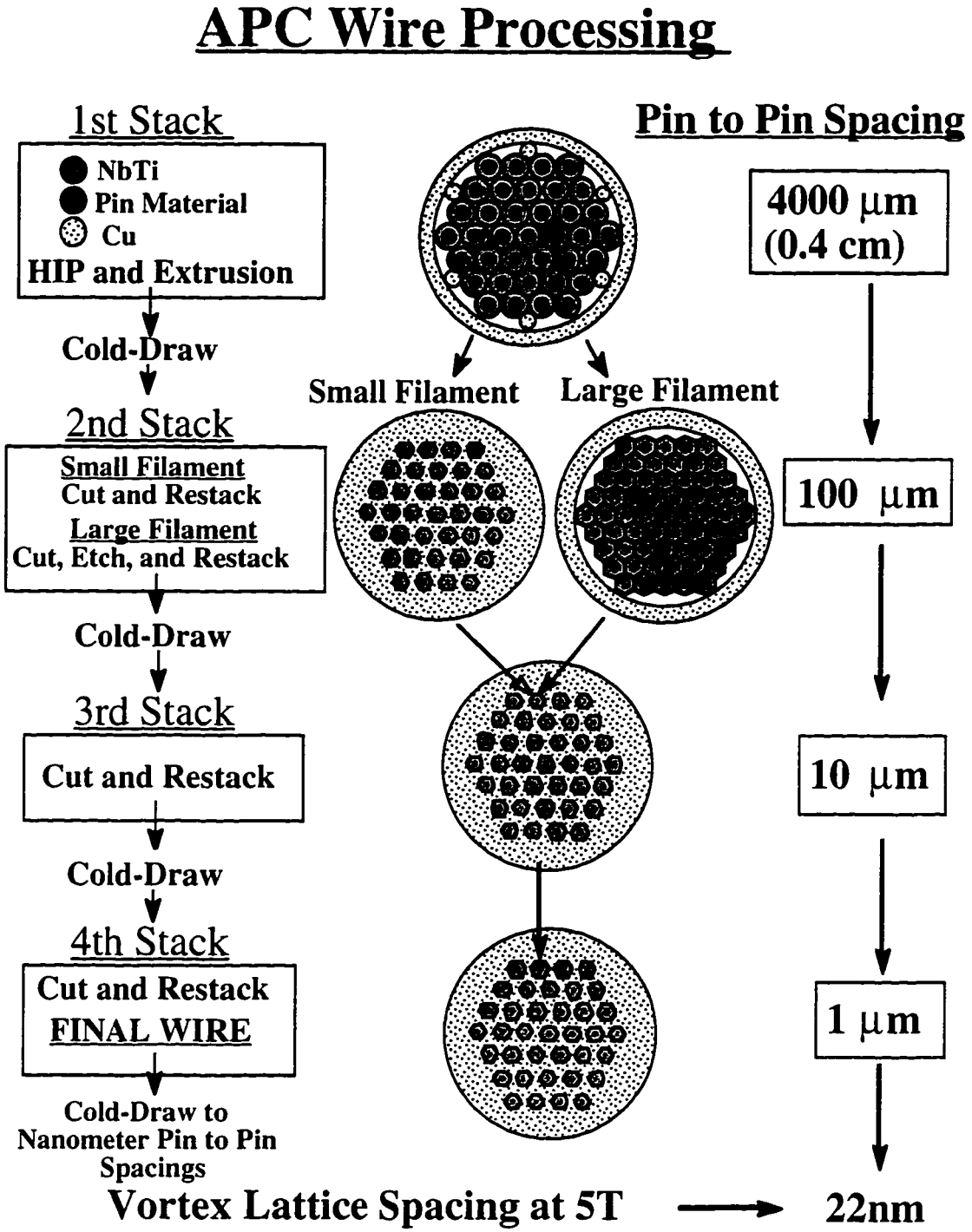

Fig 3.2. *Schematic flow chart of the APC restack and draw process. The center to center pin spacing in the boxes on the right is the pin spacing for the wire when it in the corresponding processing box on the left. The final optimum pin spacing is typically around 22 nm.*

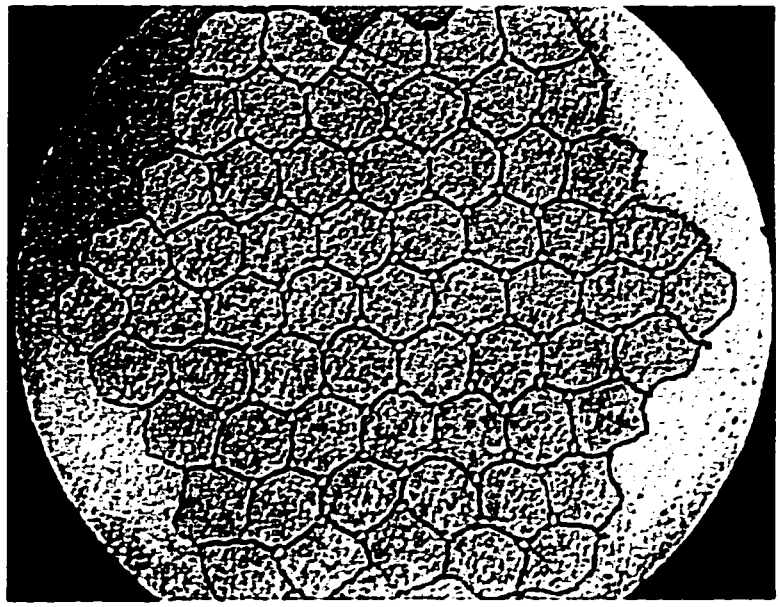

(a)

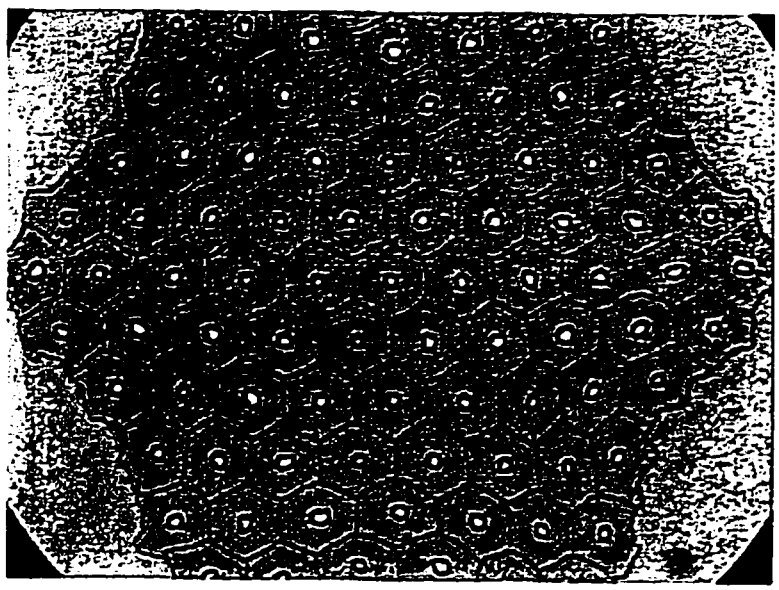

(b)

Fig 3.3. *Cross section of 1st stack wires after extrusion. (a) Interstitial approach: Ni pins in interstitial spaces between NbTi rods, (b) gun-drilled approach: Ni pins fill gun-drilled hole in center of NbTi rods. Both types of pins have a Cu diffusion barrier surrounding it. A Cu can surrounds the hexagonal filaments in both cases. The magnification is approximately 50X.*

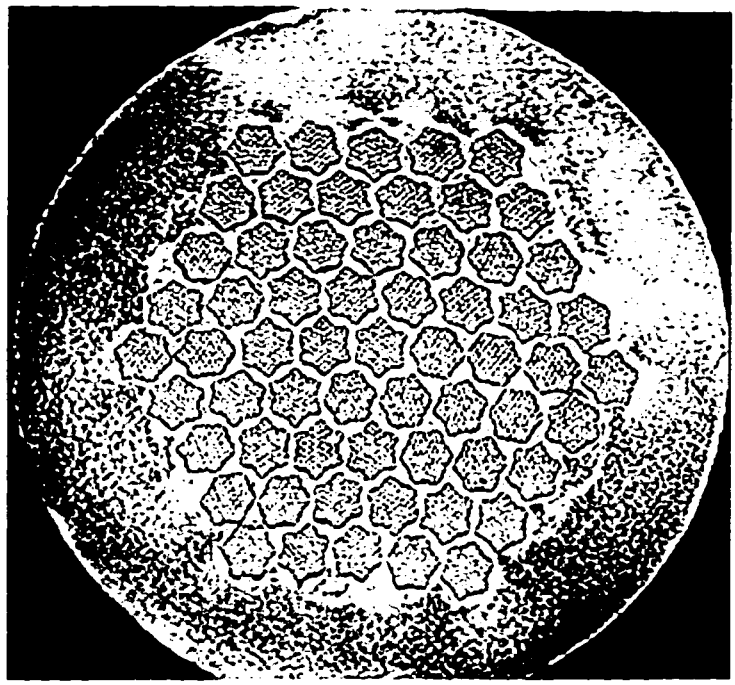

(a)

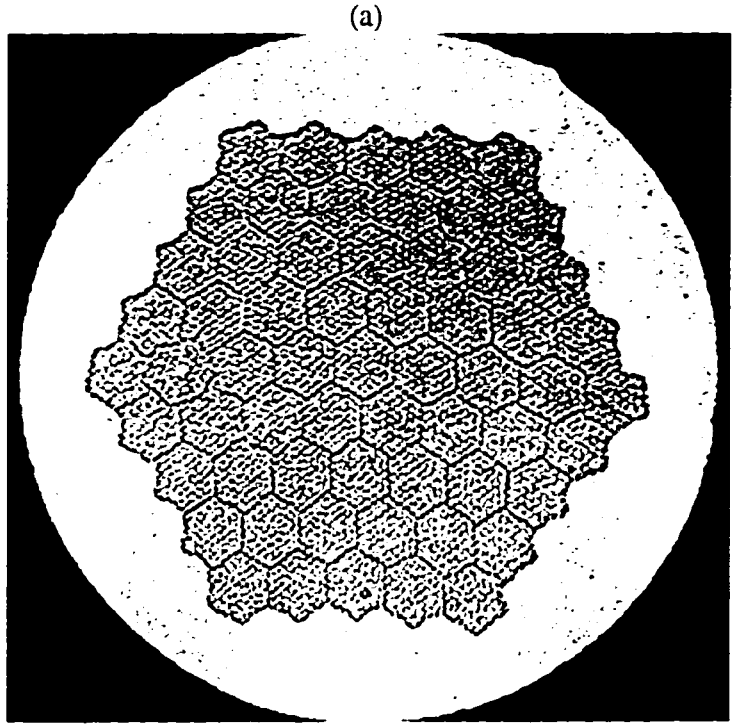

(b)

Fig 3.4. *Cross section of 2nd stack wires. (a) Small filament: the Cu cladding from the 1st Stack extrusion is left on and surrounds the hexagonal NbTi filaments, (b) Large filament: the Cu cladding is etched off before restacking so that the superconducting filament is approximately 10 times larger in area. Magnification ≈ 50X.*

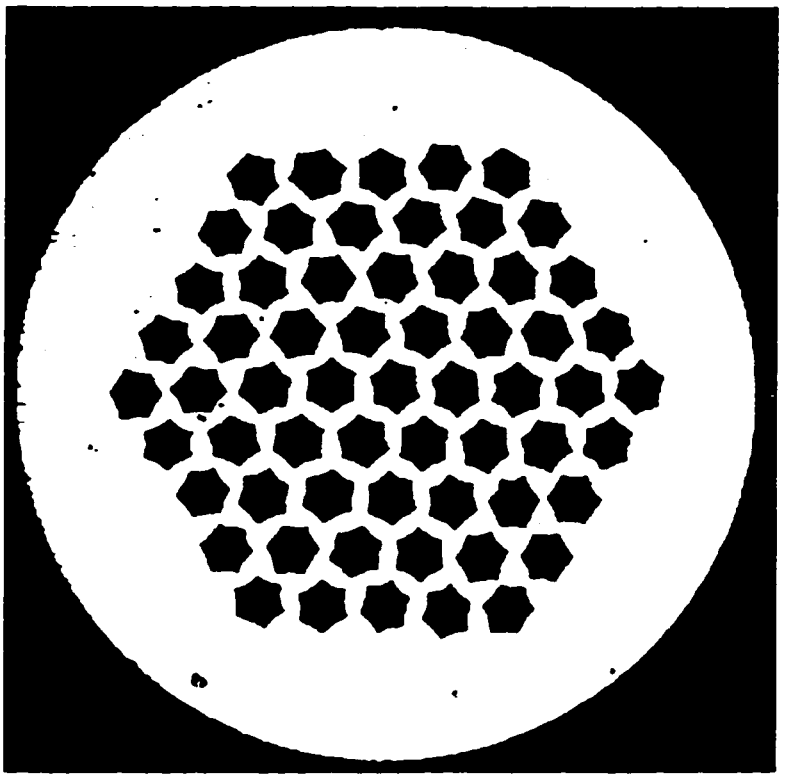

Fig 3.5. *Typical cross section of wire for 3rd and 4th stacks. The Cu between the filaments of the first and second stacks is too small to be seen. Magnification ≈ 50X.*

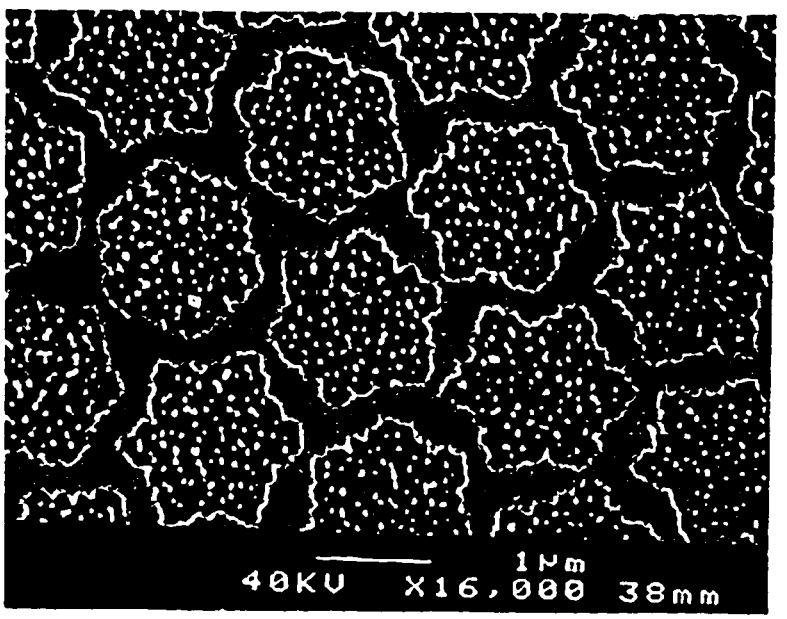

Fig 3.6. *SEM micrograph of a 4th stack small filament wire with Ni pins (wire B) near the optimum pin spacing for maximum J_c. The white dots inside the dark hexagons are the interstitial Ni pins inside the NbTi matrix. The pin spacing is approximately 150 nm.*

Table 3.1. *Description of wires made.*

Wire	Pin Material (vol. %)	Pin type	Filament type	Filament diameter at F_p^{max} (μm)	SC vol. % (NbTi+pins)
A	Ni/Cu (2/1)	interstitial	large	3	14.8
B	Ni/Cu (2/1)	interstitial	small	0.3	5.3
C	Ni/Cu (2/3)	gun-drilled	large	3	12.8
D	Fe/Cu (2/1)	interstitial	small	0.3	4.3

A description of all the wires made is given in Table 3.1. The approximate filament diameters listed here are slightly larger than those previously quoted in Rizzo *et al.* (1996), and more accurately reflect the actual point-to-point filament diameters in the wires. The volume percentage of superconductor (NbTi and pin volume) for each wire is given in column 6 of the table. All the wires listed in Table 3.1 were processed through a range of 4th stack diameters -- always including the diameter that gave optimum pin spacing for maximum J_c -- with no significant breakage. This ease of processing is unusual for new APC wires designs. This success can be attributed not only to the intrinsic ductility of the materials used, but also to several changes that were made to the standard APC restack and draw process. The changes were made to improve both wire bonding and geometry.

3.2.1. Bonding

With good bonding, a stack of NbTi rods and pins rods are more likely to respond together to drawing forces and will deform uniformly [Ozeryanksy (1996)]. This is desirable since a slip between rods can cause a non-uniform strain (or stress) in the wire and consequential wire breakage [Avitzur (1983)]. Bonding was established in our wires with a combination of HIP and hot extrusion. As mentioned previously, all of the large

(1st stack) billets were HIPed prior to extrusion. The HIP eliminates the spaces between the rods inside and begins to establish some measure of a diffusion bond between them. With good contact between the elements, good diffusion bonding is assured upon extrusion, where a high reduction ratio produces heat and pressure that greatly exceeds that of the HIP [Ozeryansky (1996), Avitzur (1983)]. Typical post extrusion diffusion lengths in NbTi are on the order of microns [Taillard (1994)].

The bonding proved to be crucial in successfully making the large filament wires. If the first stack was made by cold-drawing alone, a large filament wire would catastrophically break up during the third stack. (Dr. X.S. Ling and I painfully learned this after two unsuccessful attempts to make large filament wires that had gun-drilled Ti or interstitial Ni pins.) Since NbTi is a hard material, the bond established between two NbTi surfaces by cold-drawing is quite poor. The hard NbTi does not deform and mechanically "lock in" to the valleys on the other surface -- hence, no bond [Avitzur (1983)]. (Conversely, Cu is soft, so that Cu to Cu bonds are good even when established by cold-work alone.) Therefore, the first and second stacks of a cold-drawn large filament wire create many poor bonds between the NbTi rods (1st stack) and bare NbTi filaments (2nd Stack). In addition, on the third stack the large filament wire becomes multifilamentary, i.e., there is Cu between filaments of NbTi. The drawing force is then less uniform across the wire than for the monofilaments of the first and second stacks.

The combination of the nonuniform strength for the multifilamentary wire and the large number of poor bonds was the most likely cause of the observed wire breakage. Apparently, for the successful large filament wires, the HIP and extrusion reduced the number of poor bonds to a reasonable level for drawing of the multifilamentary wire. These results are consistent with those of Motowidlo (1992a, 1992b), who successfully made small filament APC wires using cold-drawing only. The small filament process has fewer poor NbTi to NbTi bonds since the Cu cladding is left on for all restacks. Therefore,

the transition to a multifilamentary wire on the second stack did not cause the wire to break up.

3.2.2. Wire Geometry

The wire geometry is defined as the cross-sectional spatial distribution of the different types of material in the wire. A good or bad geometry can drastically affect the wire drawability, even with excellent bonding. A good geometry is symmetric (e.g., a hexagonal pattern) to prevent asymmetry in the drawing forces across the wire. A good geometry does not have a hard core (high tensile strength) surrounded by a thick soft (lower tensile strength) shell. Upon passage through a die, the thick soft shell can begin to flow plastically, while the harder core is stressed but does not deform. Since the wire velocity is larger upon die exit than at entrance, the core will fracture and form a void (the so-called central burst) [Avitzur (1983)]. Clearly bad bonding between dissimilar elements will only aggravate the effects of a bad geometry, since the elements would be less likely to deform together.

The geometry of our wires was improved simply by using less Cu and high reductions in area. The general rule that was followed was to keep the local ratio of Cu:NbTi to be less than 1:1 [Ozeryansky(1996)]. (In fact, the high ratio of Cu:Ni for the gun-drilled pins could be causing the fluctuations in pin diameter; See Fig. 3.3(b).) With less Cu, the drawing force would be better transmitted to the core. A thin Cu shell was used for the extrusion billet ($\approx$ 25% by volume) and the Cu tubes used for the cold restacks were machined from an O.D. of 1.9 cm down to an O.D. of 1.7 cm. (The tubes had an inner diameter of 1.27 cm). At the beginning of each restack, several dies were used that had a higher area reduction to create larger drawing forces so that everything would deform together. In addition, the higher area reductions would cause the Cu to work harden more quickly and reduce its strength difference with the NbTi [Ozeryansky (1996)].

Of course, it is not clear which, if any, of these geometry improvements were absolutely *crucial* in successfully drawing the wires; however, since my interest was in examining the pinning force of ferromagnetic pins, the more subtle questions of processing were set aside, as long as the wires would draw.

3.3. Ni vs. Fe

The behavior of the Ni and Fe pins was quite different during processing. The Fe pins deformed under mechanical strain even at intermediate size, while the Ni pins remained relatively round (see Fig. 3.7) The imiscibility of Fe in Cu cannot account for the severe deformation of the pin. An Fe pin surrounded by Ni, with which Fe does form an alloy, still distorted upon drawing. The distortion of Fe *can* be attributed to the difference in grain deformation between body-centered cubic (bcc) Fe and face-centered cubic (fcc) Ni.

In bcc metals, wire drawing causes the grains to orient themselves with the [011] direction parallel to the drawing axis (this is known as texturing [Thornton (1985)]). With such a grain orientation, only two of the four <111> slip directions can contribute to extension along the wire axis (i.e, two slip directions have a projection onto the wire axis; see Fig. 3.8). Thus, plane strain elongation is possible, along with the subsequent formation of elliptical grain cross-sections. Hosford (1959) demonstrated that plane strain does, in fact, cost less energy than axially symmetric flow that involves all the slip directions. Therefore, the grains of textured bcc metals like our Fe pins undergo plane strain elongation, develop elliptical cross-sections, and must bend to maintain contact with neighboring grains, all of which causes the Fe core shape to distort. This explanation has also been used to account for the distortion of bcc Nb pins in a bcc β -NbTi APC wire, as well as the refinement of α -Ti (hcp) precipitates in conventional NbTi wire [Heussner (1995)]. The grain distortion may also impede the dislocation flow needed for good

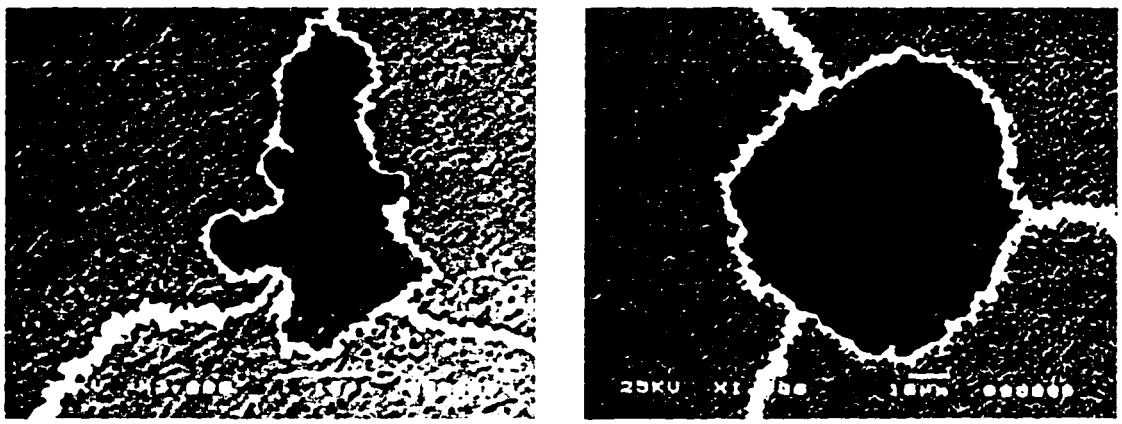

(a) (b)

Fig. 3.7. *Comparison of pin shape after extrusion and drawing for (a) an Fe interstitial pin (wire D) with magnification ≈ 2000X and (b) a Ni interstitial pin (wires A or B) with magnification ≈ 1000X. The Fe distortion is attributed to the texturing of its bcc crystal structure (Ni is fcc). See text.*

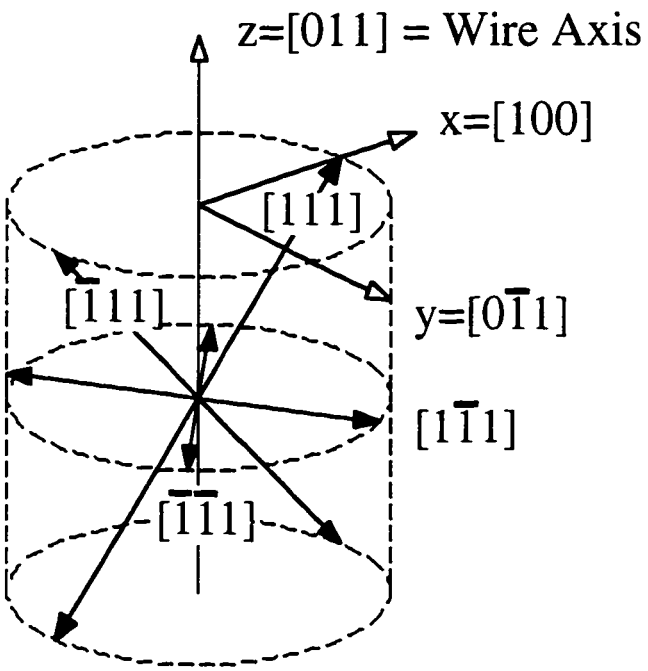

Fig. 3.8. *Diagram showing that for bcc grains oriented with the [011] direction parallel to the wire axis, only two of the four <111> slip direction can contribute to extension along the axis. From Hosford (1964).*

ductility and cause the increase in the rate of strain hardening observed for textured bcc materials after high area reductions [Peck (1964)].

In contrast, Ni has a fcc crystal structure and can have grains textured with either the [111] or [100] directions parallel to the wire axis. The <110> slip directions then have three and four-fold symmetry about the wire axis (compared to the two-fold plane-strain symmetry) so that axially symmetric flow can occur [Hosford 1964)]. Therefore, Ni pins maintain a round shape during drawing and probably a lower rate of strain hardening, as well.

3.4. Split Billets and other Gun-Drilled APCs

As was mentioned in sec. 3.1.2, four types of gun-drilled APC wires were made at the same time using split billet designs for all the HIPs and extrusions. In a split billet design, the first half of the billet contains one type of pin, the second half contains a second different type of pin. The billet is cut in half after each extrusion to separate the different types of pin material for restacking. The split billet design was used so that more types of pin designs could be examined given the finite number of 3.8 cm O.D. NbTi rods that were available. In the case of the gun-drilled Ni pin described above (wire C), the second half of the NbTi rod contained a pin that had an Fe core (2% by volume) surrounded by the Cu sleeve (3% by volume) -- Fe 2/3 in the terminology used above. This Fe 2/3 sample was not processed past the first stack because of severe Fe core distortions. It seemed unlikely that the F_p would be different from that of the interstitial Fe 2/1 sample (wire D). The relationship of pin shape to F_p is discussed in chapter 5. The other split billet also contained Fe pins: 2% Fe surrounded by 11% Cu (Fe 2/11) and 4% Fe surrounded by 9% Cu (Fe 4/9). Dr. J.Q. Wang processed these wires with some difficulty and the F_p results were inconclusive. These wires will not be further discussed.

The main disadvantage of using the split billets was that there was less good steady state material available for restacking after the extrusion. The 3.8 cm O.D. rods were 15 cm in length. If they contained only one type of pin, there was enough good material left over after extrusion for at least two separate attempts at processing a wire to optimum pin spacing. For split billets, the amount of material per type of pin was obviously reduced by at least a factor of two given the fixed length of the NbTi rods. In addition, the pin transition region in the middle of the billet produced unsteady flow and unusable material. The result was that there was only enough of the best steady state material (as determined by optical microscopy) to make one wire. Considering the length of time required to make a wire, and the number of places where errors can occur in processing, it is a bad idea to only have enough material for one attempt. In the future, the entire 15 cm length of the NbTi rod will be dedicated to one type of pin.

Chapter 4. Measurement Techniques

The primary goal of the wire measurements was to determine the J_c for a range of pin spacing and in a range of magnetic fields. Other DC and AC transport measurements were also made to determine T_c, H_{c2}, and ρ_N (normal state resistivity). These additional measurements gave information about proximity effects from the pins, as well as about the basic superconducting properties of the wire. Finally, the saturation magnetization (M_{sat}) of the pins was measured which gave information about the pin quality at nanometer size. Described below are the experimental methods that were used to measure these different wire properties at Yale, IGC, and at other Universities.

4.1. Critical Current (I_c) Measurements

The critical currents (I_c) of all the wires were measured by myself and Dr. J.Q. Wang both at Yale and IGC. The I_c's were always measured using the standard 4-probe technique at a temperature of 4.2 K and in magnetic fields from 1 to 9 T that were transverse to the wire axis. (These fields encompassed the potential field range of MRI magnets and accelerator magnets made of the NbTi alloy.) A resistivity criterion of $10^{-12}\,\Omega$ cm was used to determine I_c. J_c was defined as I_c divided by the combined area of the NbTi and the pins (ferromagnetic core with Cu sleeve); this area was determined using a standard etch and weigh technique (see Appendix A). Recall that F_p is the bulk pinning force density of the wire and is defined as $F_p = J_c B$, where B is the applied magnetic field.

4.1.1. High Current Cryostat at Yale

Dr. J.D. McCambridge and I constructed a high current cryostat to make I_c measurements of wires at 4.2 K in magnetic fields (See Fig. 4.1). The cryostat was

immersed directly in liquid helium. Four brass tubes served as the current leads from room temperature down into the helium. Brass was used because of its large thermal resistance. The heat leak from room temperature at the top, through the brass tubes and down into the helium at the bottom was greatly reduced, compared to that expected for Cu tubes. Consequently, the boiloff rate of helium was also reduced and the run time for measurements before needing to transfer more helium into the dewar was increased. Boiloff was an issue because the dewar for the smaller 6 T magnet (see below) held a relatively small amount of helium (~ 5 liters) To minimize boiloff from Ohmic heating, superconducting wire was soldered onto the lower half of the brass tubes. Therefore, during measurement the current was shunted through the wire, rather than through the resistive brass. The maximum current measured with the cryostat was approximately 120 Amps. A total of three wires could be measured at the same time (3 separate current leads, one common ground).

The APC wires were located at the bottom of the cryostat. The wires were wrapped and soldered onto cylinders (1.27 cm O.D.) that had 0.005 cm thick brass shim around a phenolic core. The shim provided better thermal contact to the helium bath and also shunted the current when the wire became highly resistive; The wire was then less likely to burn from hot spots caused by Ohmic heating. The cylinders screwed into the bottom of the cryostat. The distance of the wires from the top of the cryostat could be increased by screwing a phenolic extension rod into the bottom. The extension was necessary so that the cryostat could be used to make measurements in two different magnets (and dewars) discussed below.

The APC wire was connected to the brass current leads through a solder connection to standard superconducting wire. The voltage taps were twisted pairs of 38 gauge wire, soldered down approximately 10 to 12 cm apart and at least 1 cm inside the current leads. The total length of a wire measured was approximately 15 cm. A total of 5 twisted pairs were available, attached to a 10-pin connector at the top of the cryostat.

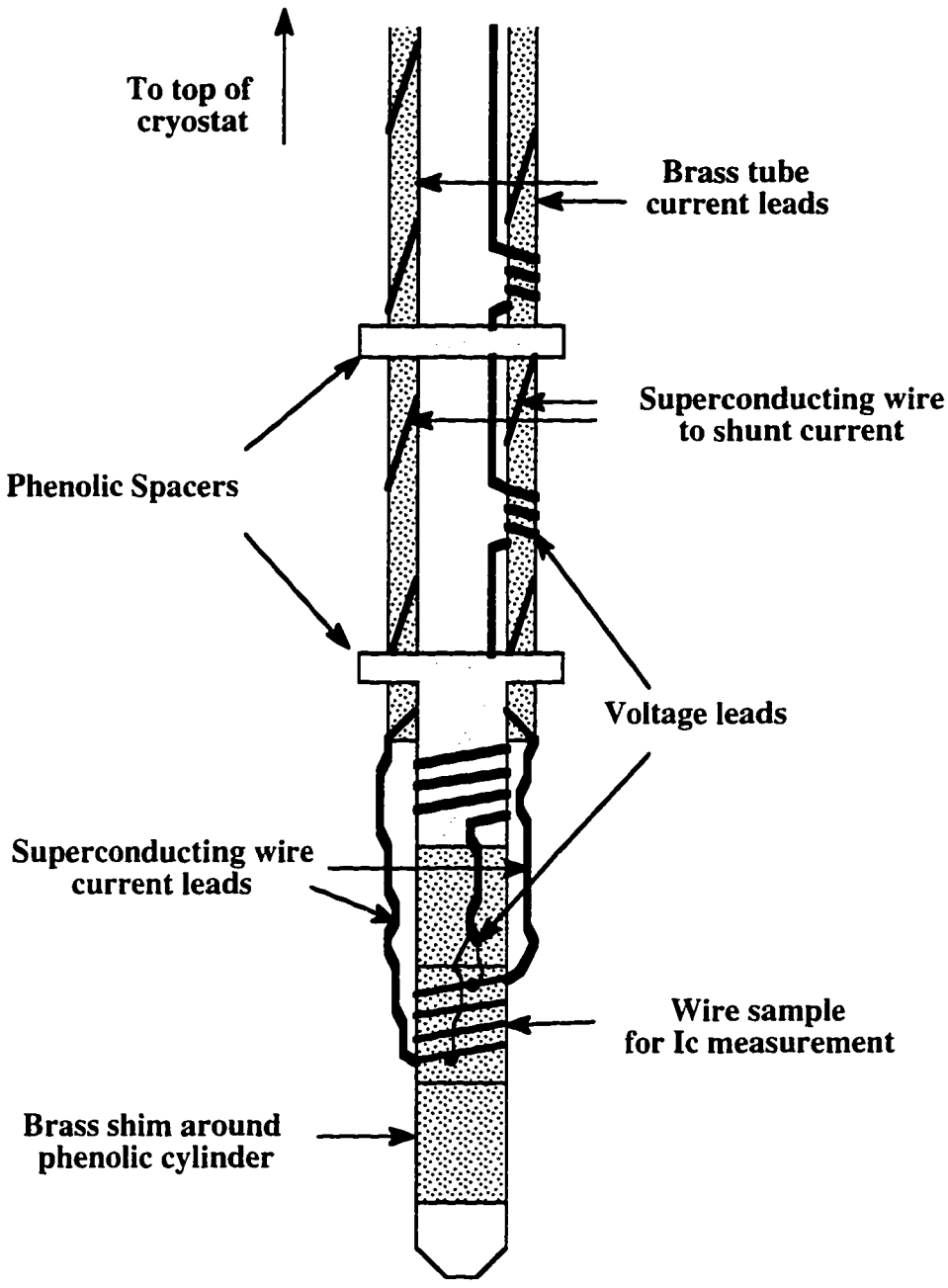

Fig. 4.1. *High current cryostat used to measure wire I_c's at Yale*

The wire voltage was measured using a Keithley 127 nanovolt null detector with a PAR 113 preamplifier on the output. The current was supplied with an HP 6259B 12V/55A power supply.

4.1.2. Magnets at Yale

The I_c measurements were made in two separate superconducting magnets. The first was a superconducting NbTi magnet (Magnet Corp. of America), that had a 2.54 cm bore and maximum fields of 6 T at 4.2 K or 8 T at 1.8 K. (The helium temperature could be reduced to as low as 1.2 K by pumping on the helium bath.) The field center was 103 cm from the top of the Cajon vacuum fitting on top of the dewar, and was homogeneous to within 5% over a distance of 2 cm away from the field center [McCambridge (1995)]. The second magnet was a superconducting NbTi magnet (Oxford Scientific Instruments) with peak fields of 9 T at 4.2 K and 11 T at approximately 2.2 K. The magnet bore was 50 mm in diameter and the field was homogeneous to less than 1% over a length of 2 cm along the magnet axis. In this case the field center was approximately 130 cm from the top of the dewar. (I made an extension for the high current cryostat so that it could be used for measurements in this magnet.) The power supply for both magnets was a Lakeshore model 601 5V/120A power supply.

4.1.3. Insert for I_c Measurements in High Magnetic Fields

Although the Oxford magnet needs to be at 2.2 K for fields from 9 to 11 T, it was possible to use this magnet to measure the wire I_c at 4.2 K in fields up to 11 T. One (expensive) way to accomplish this feat would have been to buy a variable temperature insert from Oxford. I chose an easier way and made a stainless steel insert that separated some 4.2 K helium in the magnet bore, from the 2.2 K helium surrounding the magnet. (See Fig. 4.2.) The insert works because of the properties of the lambda coil.

The magnet is cooled to 2.2 K by a "lambda" coil above the magnet. The lambda coil is a coiled tube with a needle valve on one end, and a big vacuum pump on the other end (at room temperature). Opening the valve allows helium into the tube where it is then

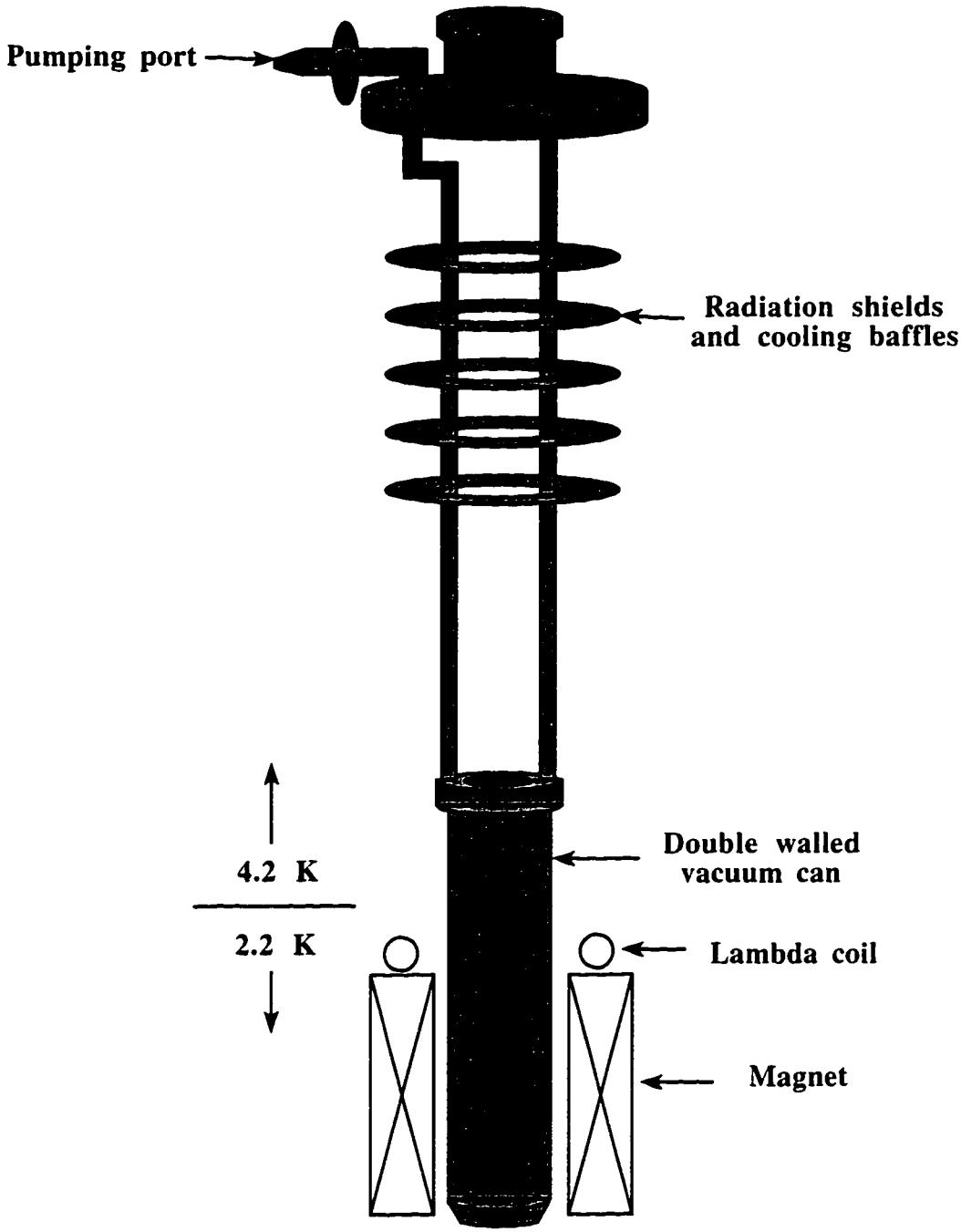

Fig. 4.2. *Insert to allow high field I_c measurements at a temperature of 4.2 K while the magnet is at a temperature of 2.2 K.*

pumped on to reduce its temperature. The helium bath outside is then also cooled through contact with the coil (like a refrigerator). However, not all the helium is cooled to 2.2 K. The 2.2 K helium, being higher density than 4.2 K helium, sinks to the bottom of the dewar and cools the magnet. The 4.2 K helium above the coil is relatively unaffected. According to Oxford [J. Betts, Private communication], a quasi-phase boundary is established between the two temperature regions.

The insert makes use of this phase boundary. At the bottom of the insert is a double walled can that is open at the end closer to the top of the insert. The space between the can walls is evacuated through a tube that is connected to a pumping port at the top. The inner and outer walls are then thermally insulated from one another. The top of the can is high enough above the coil that only 4.2 K helium spills into it. Therefore, the wire to be measured is inside the can surrounded by 4.2 K helium and at the field center of the magnet, while the magnet sits outside the can happily in 2.2 K helium.

The insert worked quite well, although not perfectly. Upon initial cooldown to 2.2 K, the helium inside the can also cooled slightly to 3.8 K, but stabilized at that temperature. Current was passed through a resistor (2 Watt maximum) at the end of the cryostat to heat the helium back up to 4.2 K. After turning off the current, the helium temperature remained stable at 4.2 K for the I_c measurements in high magnetic fields. The lack of a real phase boundary between the two types of helium (particularly upon initial cooldown) might be the source of the undesired cooling inside the can. Another possibility is that the four contact points required to space the inner and outer walls of the can also provided some cooling.

4.1.4. I_c Measurement at IGC

We also measured I_c at IGC. Their experimental setup was designed to quickly measure the I_c's of large numbers of their conventional production wires, so that measuring

the I_c of a few APC wires was a little easier than at Yale. The NbTi magnet had a maximum field of 9 T, but had a large bore diameter (> 10 cm). The IGC cryostat was also large, which made the wires easy to attach and measure. The wires were wrapped in grooves on a large stainless steel cylinder (10 cm O.D.) at the bottom of the cryostat. Up to 8 wires could be mounted at a time. The voltage taps were 62.5 cm apart and were permanently attached to the cylinder. A little dab of solder was necessary for the wire to have good electrical contact to the tap located in the groove beneath the wire. Also, the maximum possible current was much higher, so that even wire of large diameter (up to 0.18 mm) could be measured down to 1 T. IGC had an 800 Amp power supply as well as a 4000 Amp supply. Finally, the dewar that housed the magnet held more helium ($\approx$ 100 liters), so that boiloff off from heat leak or Ohmic heating was not a problem during measurement.

4.2. Saturation Magnetization (M_{sat}) Measurements

The average saturation magnetization (M_{sat}) of the pins was measured by myself and Dr. J.Q. Wang using the Quantum Design SQUID magnetometers located at the University of Connecticut, Brown University, and Columbia University. To measure samples in these systems, they must be attached to the end of a rod that is then inserted into the dewar where the SQUID is located. Our method of SQUID sample preparation is briefly described below.

A standard method was used to attach samples to the rod: the wire was put inside a clear plastic straw that was then shoved onto the end of the rod. A clear straw was chosen so that there would not be any magnetic background signal from the material used to color the straw. A piece of the wire between 5 and 30 cm in length -- enough to ensure a good signal -- was cut up into smaller pieces of order 3 mm in length, and stacked together using Duco cement (diluted by acetone). The sample volume was limited to about 2 mm^3.

Fortunately, Dunkin Donuts™ had clear plastic straws of sufficient diameter ($d_{straw} \approx 5$ mm). (It is probably possible to buy special straws and cement from Quantum Design, but it has been well established by those who frequently use SQUIDs that the paramagnetic signal from any clear straws and from Duco cement are insignificant when measuring large ferromagnetic volumes.) The sample was oriented with the field perpendicular to the wire axis -- the same orientation as for the I_c measurements. However, the field orientation was not crucial, since measurements with the field oriented parallel to the wire axis gave the same value of M_{sat} as for the perpendicular field orientation.

Initially, the Cu matrix surrounding the filaments was etched away before cutting and stacking the wire in order to avoid a possible large paramagnetic background signal from the Cu. Eventually, wires were measured with the Cu left on which showed the paramagnetic contribution from the Cu was insignificant compared to the signal from the ferromagnet. The Cu was then left on for the rest of the measurements. (This made the samples a lot easier to prepare.)

Once the samples were made, determination of M_{sat} was quite easy. The magnetic moment m of the samples was measured in fields H from 1 to 5.5 T, at temperature of 12 K, well above the T_c of NbTi ($T_c \approx 9$ K). For most samples, the moment saturated at a field between 1.5 T and 2 T, although m still increased slightly with field because of the paramagnetic background. The paramagnetic background was removed using a plot of m vs. H. A least squares linear fit to the data in the saturation region has the value of the saturated m with the paramagnetic background removed as the m-axis intercept of the fit. M_{sat} was this value divided by the volume of ferromagnet in the sample, determined from the wire length used to make the SQUID sample and the known *ferromagnetic* volume percentage in the wire. (The Cu sleeve is not part of the ferromagnetic volume. See Appendix A.)

4.3. Transport Measurements on Single Filaments

I also made transport measurements on single filaments of the APC wires to determine their basic superconducting and normal state properties, such as the critical temperature (T_c), the upper critical field (H_{c2}), and the normal state resistivity (ρ_N). Single filaments were measured, instead of the total wire that contained thousands of filaments, primarily to avoid having the measuring current shunt through the Cu matrix instead of the NbTi. Obviously, measuring the normal state resistivity of the filaments required removal of the parallel current path provided by the Cu. Since T_c and H_{c2} were also measured resistively, these measurements involved passing a current through the sample. If total wires were measured, the low resistance Cu matrix ($R_{Cu} \sim \mu\Omega$) would have shunted current before the superconducting transition had been completed. As a result, the resistive transition used to determine T_c and H_{c2} would have been affected. Perhaps the most practical reason for measuring single filaments was that their measurement required the fewest modifications to the variable temperature cryostat.

4.3.1. Single Filament Sample Preparation

The single filaments were obtained by cutting a length (~ 2 cm) of wire, etching away the Cu on half of this length, and leaving the Cu on the other half to hold the exposed filaments together. Tweezers were then used (along with a keen eye) to yank out a single filament, usually about 1 cm in length. This process could be done with the unaided eye for filament sizes down to about 1 μm. The filament was then placed on an oxidized Si wafer that was approximately 1 cm^2 in area. Electrical contact was made to the filaments using Ag paint. Voltage and current leads were painted in the standard four-probe configuration, with each corner serving as a contact pad. The center to center spacing of

the voltage taps (used in the calculation of resistivity) was typically 2 mm and the tap width was typically 1 mm.

4.3.2. Variable Temperature Cryostat

The single filament samples were measured using a variable temperature cryostat constructed at Yale (see Fig. 4.3 and McCambridge (1995)). The cryostat was inserted directly into the helium bath and could be used in either magnet system that was discussed previously. A Cu block served as the variable temperature stage inside a brass can at the lower end of the cryostat. A Teflon spacer thermally isolated the block from a Cu rod, part of which was exposed to the helium bath outside the can. Using a pumping port at the top of the cryostat, the can was evacuated before measurement to a pressure of less than 1 mTorr, as measured by a thermocouple pressure gauge at the top of the cryostat. Therefore, the block was thermally isolated from the can walls by vacuum, as well. The block had a weak thermal link to the helium bath provided by the electrical leads to the sample and the thermometer. Approximately 20 twisted pairs of 38 gauge Cu wires were wrapped many times around the upper Cu rod, over the spacer, and the lower Cu block. The leads were attached to two 10-pin connectors at the top of the cryostat.

The block temperature was varied using a 1/4 Watt 1 kΩ metal film resistor inserted into a hole in the block as the heater. With the can under vacuum, only 10 to 20 mW of power was necessary to raise the block above 10 K. The block temperature was measured using a calibrated RuO_2 thin film resistance thermometer. The resistance was determined with a four wire measurement using either a home-made thermometer box [Dalrymple (1987)] or an HP 34401 DVM operating in four wire resistance measurement mode. The thermometer excitation currents were between 1 and 5 μA giving μW in dissipation, for which there was no evidence of thermometer self-heating.

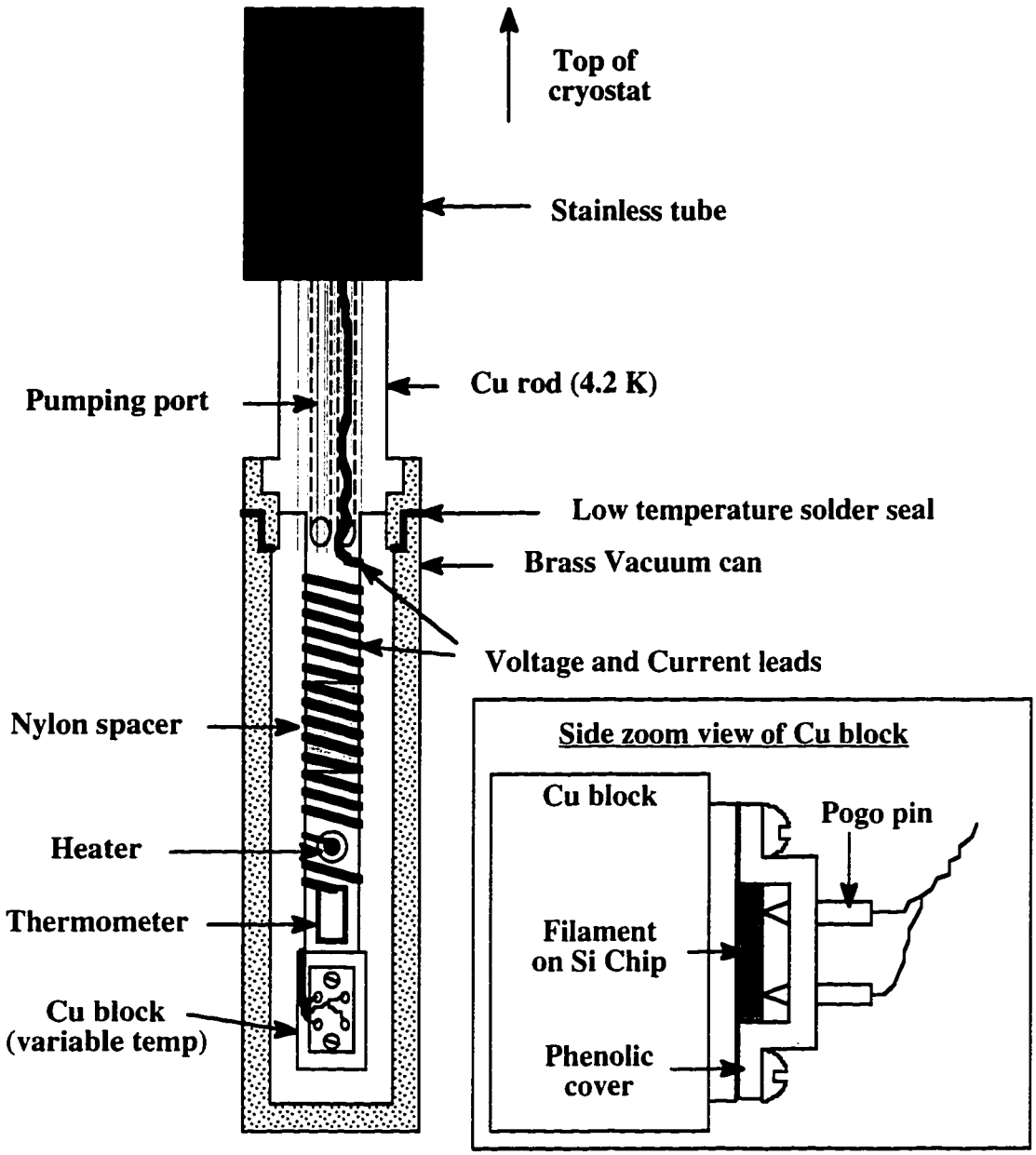

Fig. 4.3. *Variable Temperature Cryostat used to make transport measurements on single filaments of APC wires.*

The Si wafers with the filaments on top were pressed onto the variable temperature Cu block with Apiezon N grease on the back of the wafer to make them stick. Electrical contact to the sample was made using a phenolic block that had pogo pins (pins with spring loaded tips) in holes in each corner, with each pin connected to 38 gauge wires . The cover

was screwed down into the Cu block, and over the wafer so that the pogo pins compressed into the Ag contact pads located in each corner of the wafer.

4.3.3. AC and DC Measurement Techniques

T_c and H_{c2} were determined resistively using standard AC techniques. A small AC current was supplied by applying a 1 kHz reference signal of magnitude between 1 to 5 mV across both the filament and a 100 kΩ resistor. The normal state filament resistance was typically 100 Ω so that the AC current of 10 to 50 nA was independent of the filament resistance to within about 0.1%. The current densities in the filament were between 0.05 A/cm^2 to 0.2 A/cm^2. (Current densities less than 1 A/cm^2 should not significantly affect resistive T_c or H_{c2} measurement [Collings(1986)].) A PAR 124 lock-in amplifier was used to detect the AC voltage across the filament, thus giving the resistance by Ohm's law.

The 50% point on the transition between the superconducting and normal state resistance was used to define T_c in transverse magnetic field fields from 0 to 8 T. At each field, the T_c was measured for both heating (T_c[up]) *and* cooling (T_c[down]) of the sample through the superconducting transition.; the thermal hysteresis of the transition between heating and cooling was typically 30 mK. The average of T_c[up] and T_c[down] was used as the best value of T_c.

The filament normal state resistance was measured by taking a DC I-V curve. In calculating the normal state resistivity ρ_N, the length was taken as the center-to-center distance between the voltage taps and the area was the total filament area in the wire (known from the measured superconductor percentage) divided by the number of filaments. The voltage was measured with the Keithley 127 nanovolt null detector and the current supplied by a Yokogowa 30V/120mA power supply.

Chapter 5. Experimental Results

In this chapter, the results of the transport and magnetization measurements on the NbTi wires with ferromagnetic artificial pins are reported and discussed. Although all the wires had an approximate ferromagnetic pin volume of 2% along with a similar pin geometry, significant differences existed between the F_p of the wires. These differences are understood as being caused by the different filament sizes in the wires and the different amounts of pin material becoming nonmagnetic in the wires. The overall shapes of the F_p vs. B curves are different from those of conventional wires. The difference in shape is understood as an effect of the lower pin density in our APC wires. Finally, the results of measurements made on single filaments of wire C to determine T_c, H_{c2}, and ρ_N are presented. These measurements were used to extract the superconducting parameters for the NbTi and to examine proximity effects from the ferromagnetic pins.

5.1. Critical Current Density (J_c) and Bulk Pinning Force (F_p)

A description of the four wires that were produced is given again in Table 5.1, for convenience. For all four different types of wires, J_c was measured at 4th stack wire diameters ranging from 1.8 mm to 0.15 mm. For the range of 4th stack wires measured, the pin spacing d_p ranged from 140 nm down to approximately 12 nm; The optimum d_p (giving maximum J_c) was found to be between 25 to 30 nm in all the wires. The results of J_c measurements on wire C for various d_p are shown in Fig. 5.1 and are typical of all the wires.

To examine the pinning force that holds the vortices, a more useful quantity to display is the bulk pinning force density $F_p = J_c B$. Recall that in a direct summation of pin strengths, $F_p = n_p f_p$ where n_p is the effective pin number density and f_p

Table 5.1. *Description of wires made.*

Wire	Pin Material (vol. %)	Pin type	Filament type	Filament diameter at F_p^{max} (μm)
A	Ni/Cu (2/1)	interstitial	large	3
B	Ni/Cu (2/1)	interstitial	small	0.3
C	Ni/Cu (2/3)	gun-drilled	large	3
D	Fe/Cu (2/1)	interstitial	small	0.3

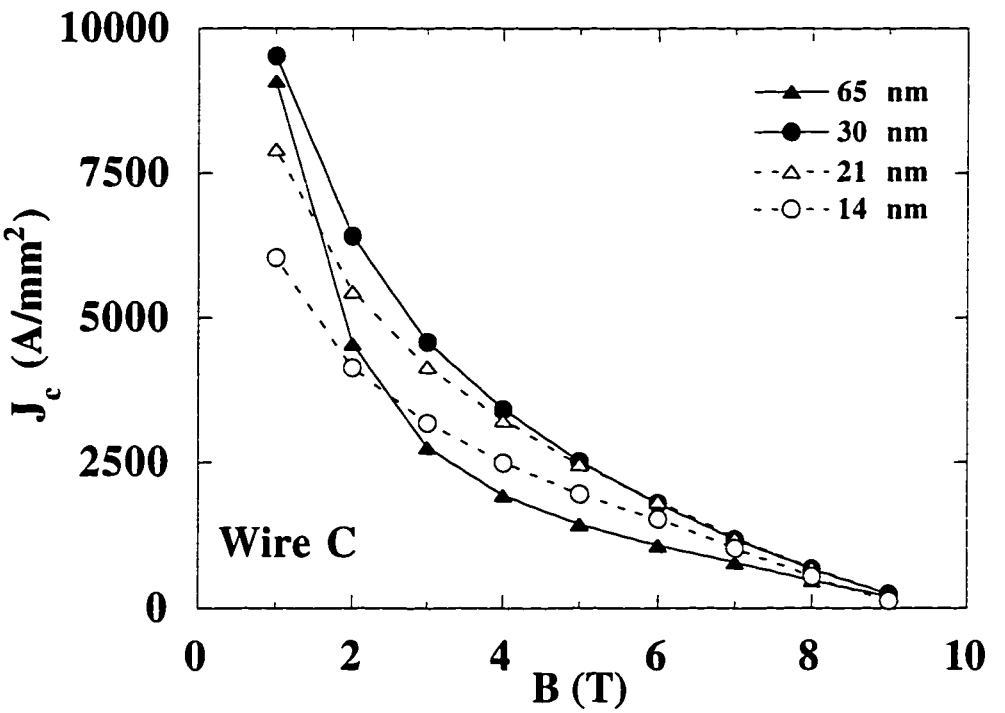

Fig. 5.1. *Critical current density (J_c) vs. magnetic field (B) for wire C at various pin spacings (d_p).*

is the force of one pin (elementary pinning force). Therefore, the effects of pin strength and of pin density are more easily determined by plotting F_p vs. B. In Fig. 5.2 and Fig. 5.3, F_p vs. B is shown for all four wires for various d_p.

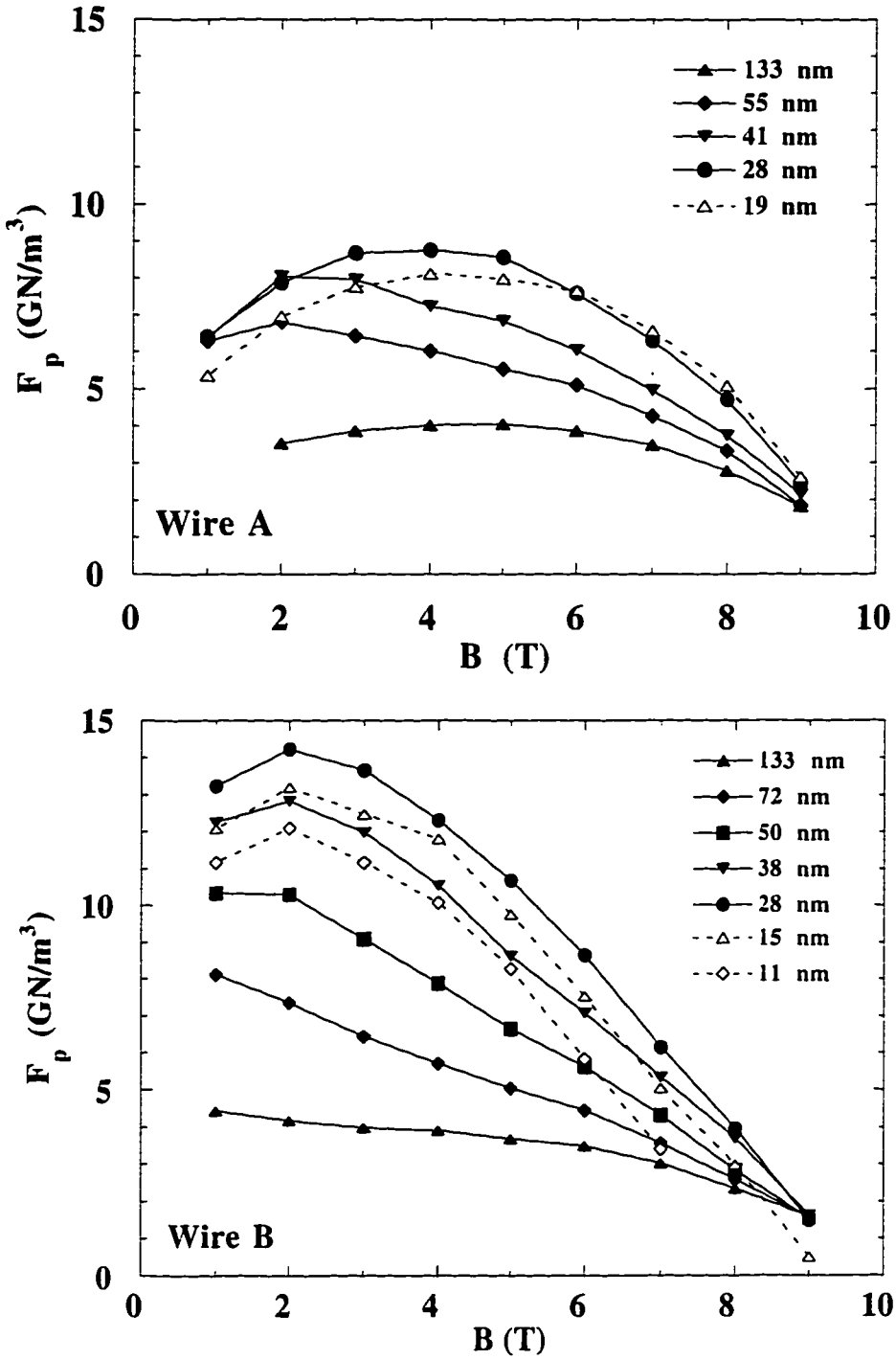

Fig. 5.2. *Bulk Pinning Force Density (F_p) vs. magnetic field (B) for large filament (wire A) and small filament (wire B) wires that have interstitial Ni pins. The pin spacings (d_p) are listed in the legend.*

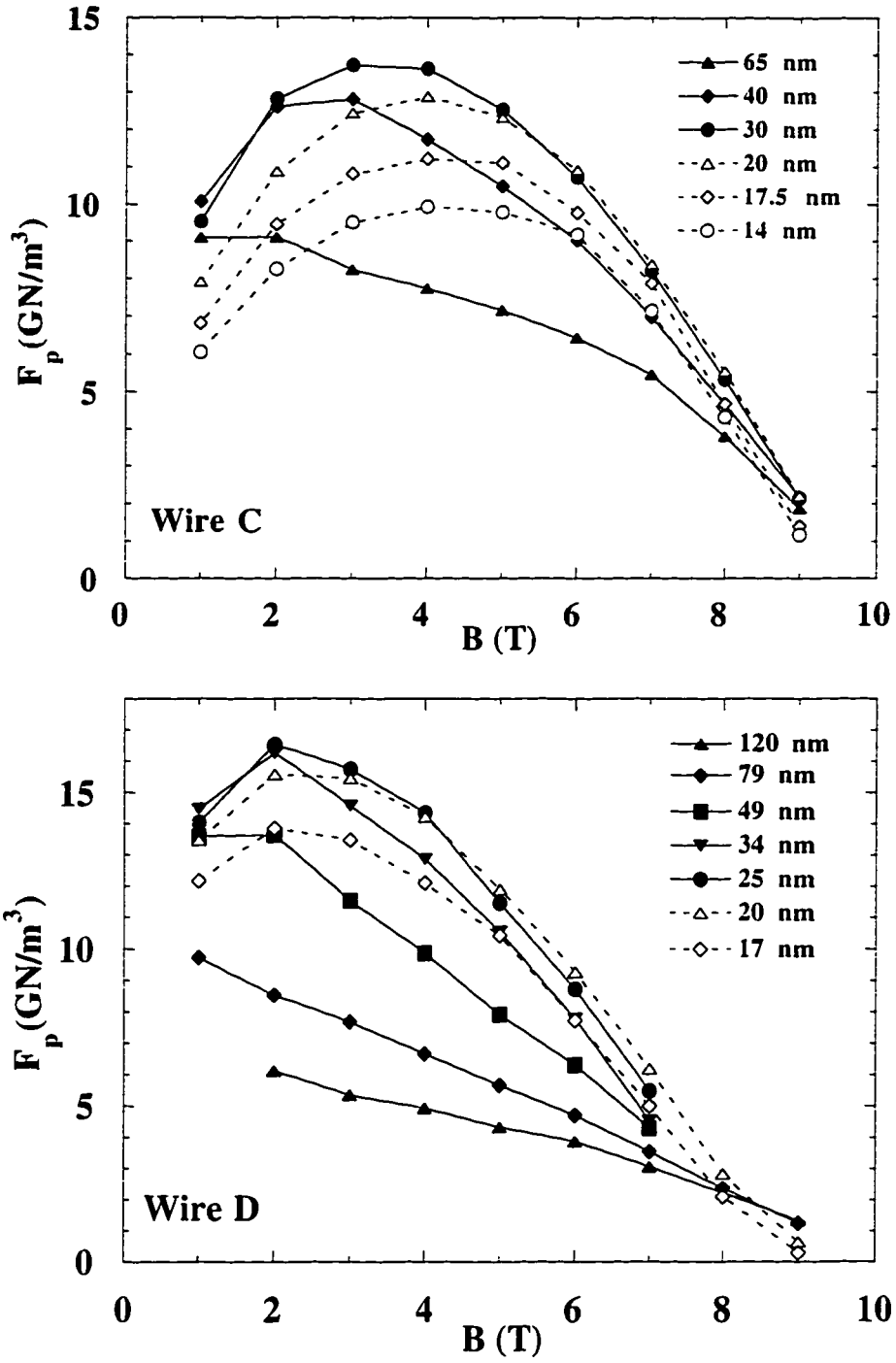

Fig. 5.3. *F_p vs. B for wire C (large filament with gun-drilled Ni pins) and wire D (small filament with interstitial Fe pins. The pin spacing (d_p) for the wires are listed in the legend.*

For each type of wire at optimum pin spacing, F_p has a well-defined maximum in the mid-field region (from 3 to 5 T) where the vortex density and the pin density are comparable. F_p decreases as B approaches H_{c2} because of the field dependence of $f_p \propto (1-b)$. Notice that the shape of the F_p curves does not follow the general form of $F_p \propto b(1-b)$ derived earlier in chapter 2, but rather has a peak at fields lower than $0.5H_{c2}$. This dependence of F_p on B is discussed in more detail below.

The general trend for the wires is that the overall F_p increases as n_p increases (d_p decreases), eventually reaches a maximum, then decreases once again. This trend is more easily seen in Fig. 5.4, where F_p vs. d_p is plotted for wire C. Although n_p is continually increasing, eventually f_p begins to decrease significantly, thereby reducing the overall F_p. Two factors probably contribute to this decrease f_p. When the pin diameter becomes small ($d_{pin} \sim \xi_{FM}$), the order parameter can penetrate into the pin, particularly at low fields (See Fig. 2.2.) In this case, the effective volume of the pin is reduced and, consequently, f_p is reduced. Additionally, the ferromagnetic pins are eventually so close together that T_c and H_{c2} are reduced from proximity effects; Therefore, condensation energy is lost and f_p is again reduced, particularly at high fields. Proximity effects are discussed in more detail below.

5.1.2. F_p Comparison

A comparison between the F_p vs. B for the four different wires at optimum pin spacing is shown in Fig. 5.5. Although all the wires had approximately the same volume of ferromagnet (2%), wires B and D had additional pinning because of small filament size. A comparison between wires A and B showed that the reduced filament size increased F_p by 5-7 GN/m^3 for $B \sim$ 1-3 T; the magnitude of this increase was comparable to that observed in other wires that had sub-micron NbTi filaments separated by Cu [Cooley (1993)]. The additional pinning is attributed to the interfaces between the Cu cladding

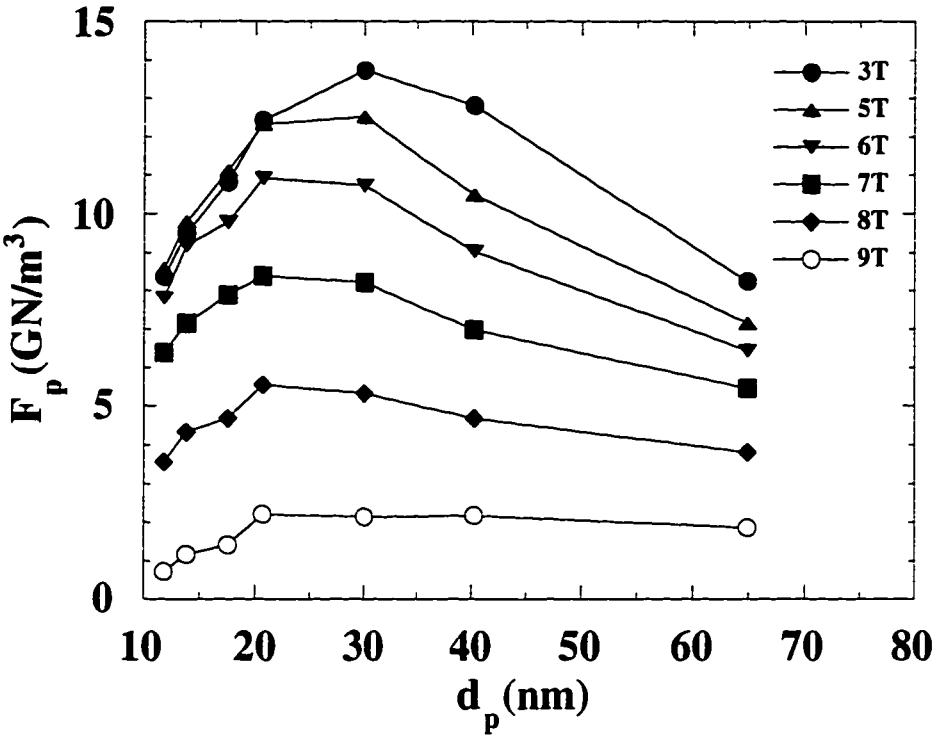

Fig. 5.4. *F_p vs. d_p for wire C at various magnetic fields (B) shown in the legend.*

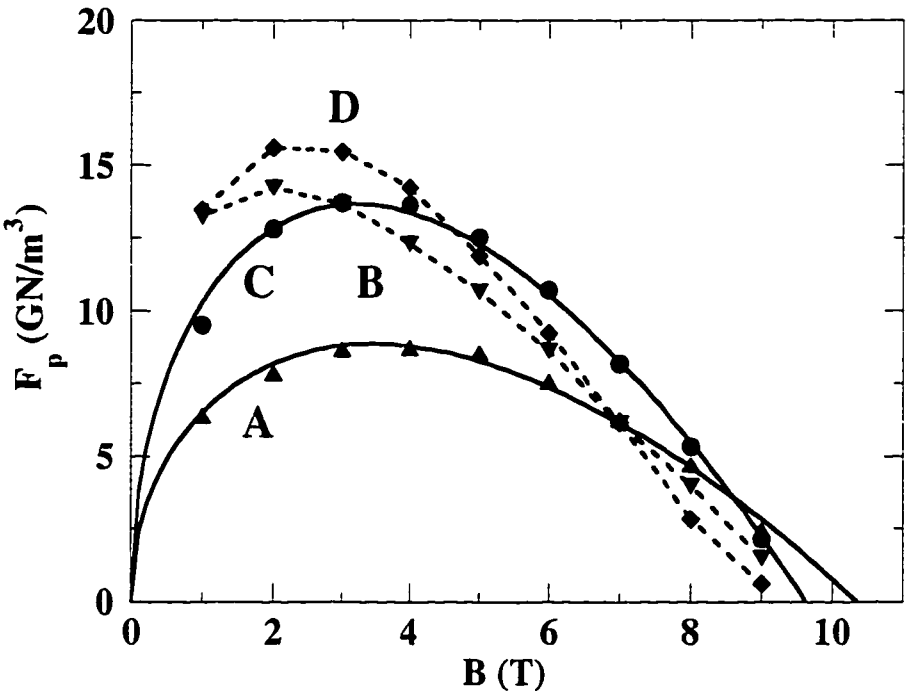

Fig. 5.5. *F_p vs. B for the four different wires at optimum pin spacing. The dotted lines for wires B and D are guides to the eye. The solid lines for wires A and C are fits to the function $F_p \propto b^{1/2}(1-b)$.*

(from the extrusion can) and the small NbTi filaments of wires B and D (d_{fil} ~ 0.3 μm). For wires A and C (d_{fil} ~ 3 μm), the interfaces were far enough apart (had lower density) so that they did not contribute significantly to F_p. (The surface pinning contribution to F_p for wires A and C was at most 0.5-0.7 GN/m^3, assuming $F_p \propto 1/d_{fil}$; See below.) Therefore, the gun-drilled Ni pins produce larger F_p than the interstitial Ni or Fe pins alone. This is discussed below.

5.1.3. Surface Pinning and Size Effects

The additional pinning at the Cu-NbTi interface can be understood as a Bean-Livingston type surface barrier to the vortices [Bean (1966), de Gennes (1966), Clem (1974)]. (See the discussion on surface pinning in chapter 2.) Recall that a vortex inside a superconductor and near the surface is attracted to its image vortex outside the superconductor, but is also repelled by the Meissner shielding currents. These effects combine to create a surface barrier to vortex entry into the superconductor. The effects of this surface barrier pinning in our wires can be estimated by approximating the NbTi-Cu geometry with Clem's (1974) model system of alternating slabs of type-II superconductor and insulator discussed in chapter 2. There it was found that a superconductor/insulator repeat distance of $D \sim \lambda \sim d_{fil} \sim 0.3$ μm provides a surface pinning strength of $F_p \approx 6$ GN/m^3; This is approximately the enhancement of F_p that was observed for the small filament wires.

If the additional pinning occurs at the filament surfaces, then F_p should increase with an increase in the linear density of the surfaces. Clem's model predicts $F_p \propto 1/d_{fil}$. As before, the surface pinning force in our wires can be determined by subtracting F_p of wire A from that of wire B at comparable pin spacings; this difference in F_p versus $1/d_{fil}$ is shown in Fig. 5.6 at several different fields.

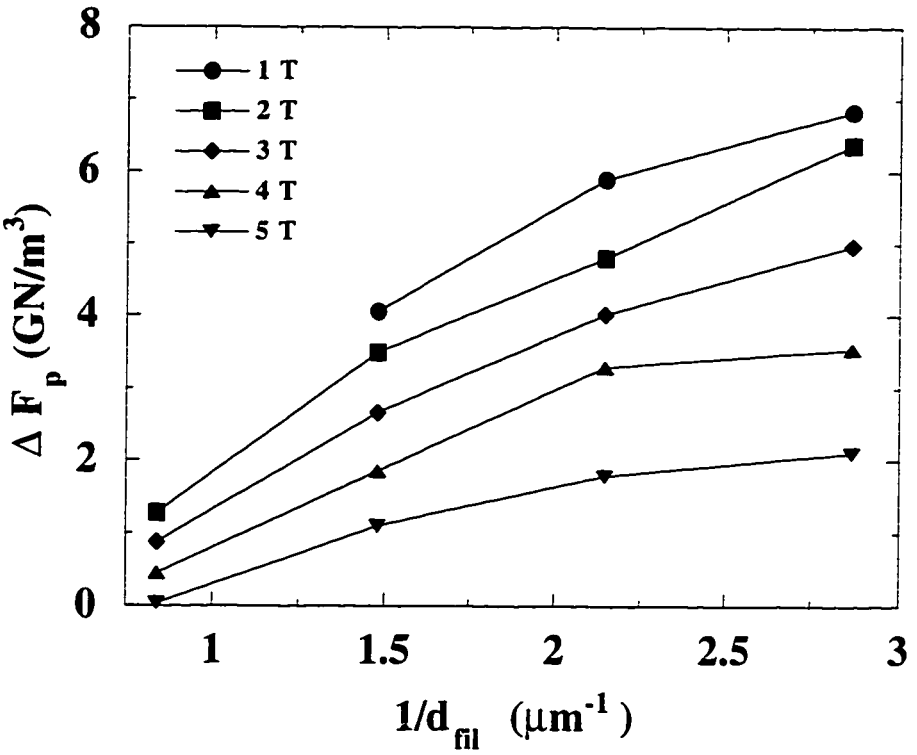

Fig. 5.6. *ΔF_p vs. $1/d_{fil}$ for various fields. ΔF_p is the difference between the F_p of wires A and B at comparable pin spacings. d_{fil} is the small filament diameter of wire B.*

Although there is not a huge amount of data available, the general trend is an approximate linear dependence of ΔF_p on $1/d_{fil}$, as expected.

Obviously Clem's model does not simulate the surface pinning in the wires exactly. For example, as seen in Fig. 5.6, ΔF_p, and hence the surface pinning in the wires, decreases with field. The model predicts the surface pinning to be constant in intermediate fields B, defined as $\Phi_o/\lambda^2 < B << H_{c2}$. Then for fields $B \geq 3$ T $\approx 0.3H_{c2}$, the model may no longer be valid. In addition, the model assumed $d_{fil} \geq \lambda$, which was necessary to define equilibrium values of the magnetic field in the slabs away from the surface. Therefore, the smallest filaments are also at the size limit for the validity of the model.

In fact, calculations have shown that a thin slab of NbTi ($D \leq \lambda$) of superconductor can have a one-dimensional vortex lattice up to fields as large as 1 T [Takacs (1988)]. The field dependence of the surface pinning strength is more easily understood in this scenario.

At low fields, a 1-d vortex lattice sits symmetrically in the center of the slab, being repelled equally from each surface by the Meissner currents. As the field is increased, the lattice becomes 2-dimensional (i.e., the slab has more than one row of vortices) and the repulsion between the vortices forces them away from the center of the slab and up the potential well [Takacs (1988), Stejic (1994), Mawatari (1994)]. Thus, the surface pinning force is reduced.

A more exact model of the surface pinning would need to account for having Cu, a clean normal metal, rather than an insulator (or vacuum) between the NbTi filaments. The order parameter can penetrate into the Cu and decay over a length ξ_{Cu}. Thus, there is not a sharp superconducting boundary as at an insulator. In this case, the image force will be reduced since the current can flow normal to the boundary. In addition, the field dependence of the proximity-induced superconductivity in the Cu may affect the field dependence of the surface pinning [Takacs (1986)]. However, in general, Clem's model provides a good simple understanding of the observed size effects in our wires as caused by surface pinning.

5.1.4. F_p Comparison between Ferromagnetic and Nonmagnetic pins

In Fig. 5.7, the F_p of wire C at optimum d_p is compared with that of optimized conventional wires and two other APC wires with Nb pins at optimum pin spacing. MRI is conventional wire used to make resonance imaging magnets while SSC is conventional wire that would have been used to make magnets for the Superconducting SuperCollider (The data is for typical wires manufactured by IGC-Advanced Superconductors.) Both of these conventional wires contain a precipitated Ti pin volume of 17-20% [Lee (1990)].

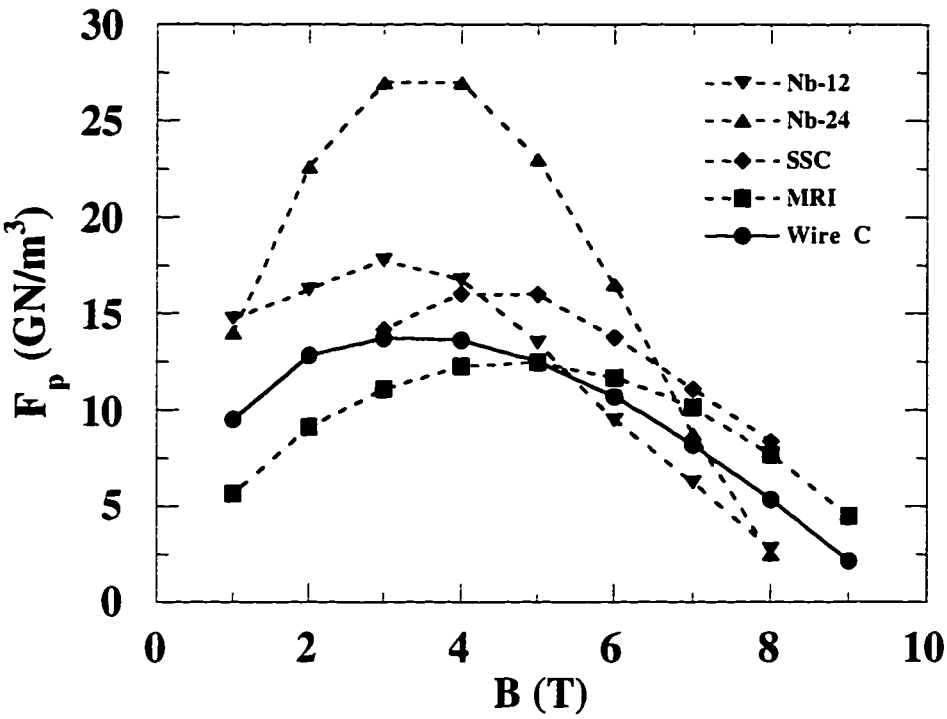

Fig. 5.7. *F_p vs. B for wire C, two conventional wires (MRI and SSC) with a pin volume of approximately 20 % Ti, and two APC wires with a pin volume of 12% $Nb_{0.98}Ti_{0.02}$ (Nb-12) and 24% Nb (Nb-24). All wires either have large filaments ($d_{fil} \geq 3$ μm) or have had the contribution to F_p from filament size effects removed.*

Nb-12 and Nb-24 are two APC wires (described in chapter 1) that contain artificial pins with a volume of 12% $Nb_{0.98}Ti_{0.02}$ [Cooley (1993)] and 24% Nb [Heussner (1997a, 1997b)], respectively. (For reference, the Nb-24 wire has the highest F_p at 5 T and 4.2 K of any APC wire, to date.) In contrast, the ferromagnetic pin volume is only 2% Ni in wire C. (The 3% Cu diffusion barrier probably made no significant direct contribution to F_p. A Ti pin volume of 2.5% in a conventional wire provided at most an additional 2 GN/m^3 [Lee (1990)]. Cu is an even weaker pin than Ti [Motowidlo (1992a, 1992b)].) Therefore, ferromagnetic pins are more effective than nonmagnetic pins for a given volume percent.

These results are consistent with our discussion of pin strength in chapter 2. There it was proposed that small ferromagnetic pins can create large effective pin volumes because of their strong suppression of superconductivity as reflected by their extremely

short coherence lengths (ξ_{FM} ~ 1 nm). In contrast, nonmagnetic materials are not as effective at suppressing superconductivity and more material is needed for large effective pin volumes.

These results can be compared with those of Koch and Love (1969) who also examined the effectiveness of ferromagnetic and nonmagnetic pins. They measured the J_c of Nb that contained dispersions of either ferromagnetic Gd particles or nonmagnetic Y particles. It was found that three different samples -- $Nb_{0.995}Gd_{0.005}$, $Nb_{0.95}Gd_{0.05}$ and $Nb_{0.98}Y_{0.01}$ -- all had J_c's that were approximately 20 times that of pure Nb, but that there was relatively little difference in J_c between the samples. They concluded that there was no significant difference in pin strength between ferromagnetic Gd and nonmagnetic Y.

The probable reason that they observed no difference was because of the large size of the Gd and Y particles. The dispersions were found to consist of particles ranging in diameter from 0.2-0.6 μm; this size is much larger than the size of the vortex core in their Nb, where $2\xi \approx 0.04$ μm. Therefore, the vortices are more likely to pinned by the particles through a surface pinning mechanism, rather than through core pinning. For surface pinning, the fact that a ferromagnet has a shorter coherence length than a nonmagnetic material is less significant, as long as the pin is large enough so that the order parameter can decay to zero inside the pin. A large ferromagnetic pin or a large nonmagnetic pin will then behave equally well as a nonsuperconducting surface, and can provide similar pin strengths.

The results of this thesis can also be compared with those of Yetter *et al.* (1982), who measured the pinning force of antiferromagnetic Cr layers in thin films of superconducting $Pb_{0.82}Bi_{0.18}$ (H_{c2} = 0.63 T, T_c = 7.8 K). They found that Cr layers only 2 nm thick and spaced 60 nm apart increased the F_p of the films almost a factor of 10 compared to unlayered films. Thicker Cr layers did not give any further increase which indicated that the PbBi layers were already decoupled by 2 nm of Cr. This is consistent with the value $\xi_{Cr} \approx 0.5$ nm, determined by Hauser (1966). They also found the pin

strength of a single Cr in the film to be comparable to that of a Cr layer on the surface of an unlayered film. These results indicate that the increase in F_p was probably due to surface pinning at the Cr layers, rather than the core pinning that is expected to be dominant in our wires.

In any case, they did not measure any films with nonmagnetic layers to compare the relative pin strengths of magnetic and nonmagnetic layers. If they had made such measurements, they would probably have found that the nonmagnetic layers must be much thicker than 2 nm to decouple the PbBi layers and provide strong surface pinning comparable to that of the 2 nm thick Cr layers. Exact comparison with the results stated here would have been complicated by the differences in pin geometry between the films and wires. An experiment that would have probably yielded results similar to those of this thesis would have been to measure and compare the F_p of films that had dispersions of either Cr or nonmagnetic particles of nanometer size, so that core pinning would be dominant as in our wires.

5.2. Saturation Magnetization (M_{sat}) versus Pin Diameter

Despite their relative strength, the effectiveness of the ferromagnetic pins was probably reduced by some pin material becoming nonmagnetic at optimum size. If a pin becomes partly nonmagnetic, then it will not depress the order parameter as much as if it were fully ferromagnetic and the *effective* pin volume will be reduced. The evidence for the loss of ferromagnetic material is shown in Fig. 5.8. The average saturation magnetization (M_{sat}) of the pins was measured using a SQUID magnetometer at a temperature of 12 K, well above the T_c of NbTi (T_c ~ 9 K). Since the M_{sat} of bulk Fe and Ni is a well-known constant at low temperatures, any drop in M_{sat} reflects a loss of ferromagnetic material in the pin volume. The loss of magnetization for Fe was much larger than that for Ni. However, the bulk M_{sat} of Fe is three times greater than that of Ni

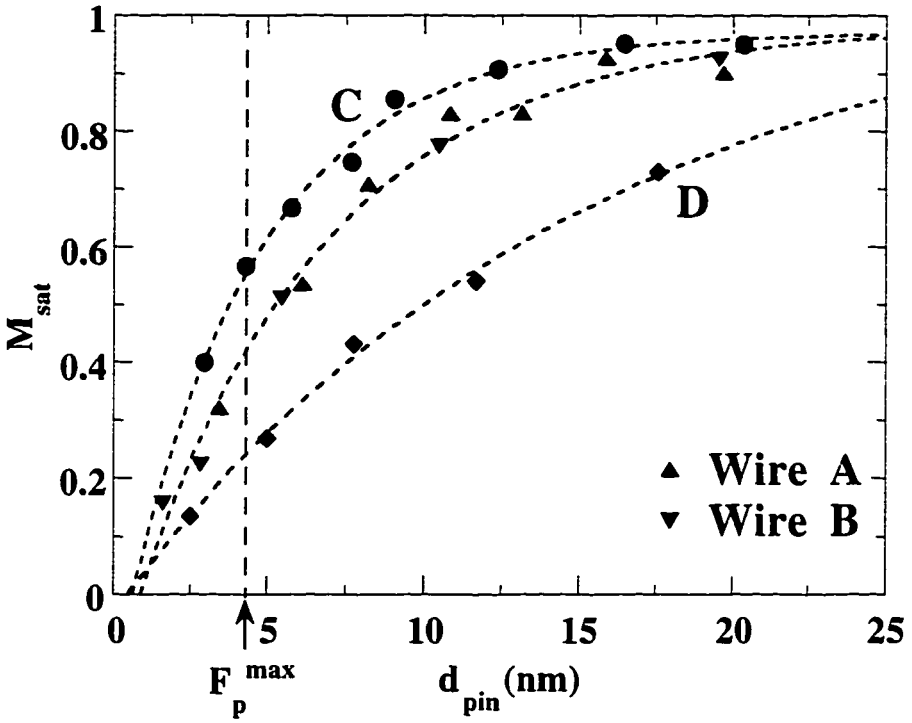

Fig. 5.8. *Average Saturation Magnetization (M_{sat}) vs. ferromagnetic pin diameter (d_{pin}); M_{sat} for each type of pin is normalized to the value for the largest measured pin diameter (≥1500 nm), which was usually within 5% of the bulk value for M_{sat}.*

[Kittel (1986)]; this may explain why F_p is comparable for wires B and D. At optimum pin size (d_{pin} ~ 4 nm), almost 50% more Ni remained ferromagnetic in wire C than in wires A and B. This correlates with the larger F_p of wire C compared to wire A.

Because of the nanometer pin sizes, the reasons for the loss of magnetic material were difficult to determine. It may be possible that as a result of cold-work, some mechanical mixing of the ferromagnet and the NbTi occurred at the nanometer size scale, thus producing a nonmagnetic (or less strongly magnetic) alloy. The Fe pins deformed under mechanical strain even at intermediate size, while the Ni pins maintained a relatively uniform shape (see Fig. 3.7). This would explain the more severe loss of magnetization for Fe compared to Ni. The gun-drilled Ni pins had a thicker Cu barrier and a rounder shape at intermediate size than the interstitial Ni pins; consequently, M_{sat} of wire C was higher than that of wires A and B at optimum pin spacing.

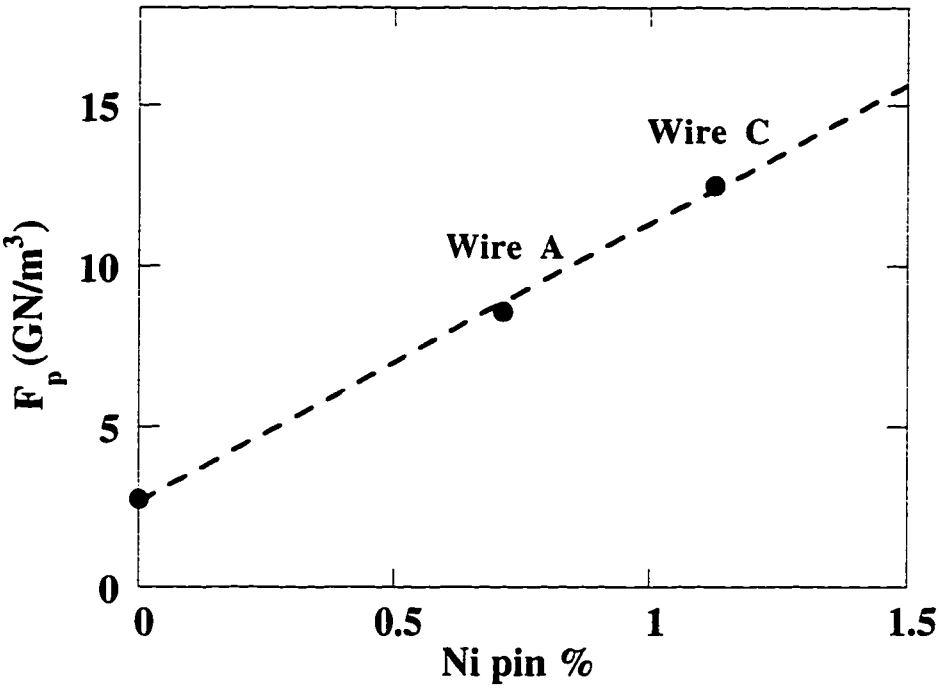

Fig. 5.9. *F_p at 5 T vs. the volume percentage of Ni that remained ferromagnetic (derived from M_{sat} measurements) in wires A and C. F_p for 0% Ni is from measurements of cold-worked NbTi [Lee (1990)].*

There was still a significant drop in M_{sat} even for wire C. Adding more Cu around the pin may better isolate the ferromagnet and help to maintain M_{sat}. However, a thicker Cu barrier would also create a high local ratio of soft Cu to harder Ni, which is a bad geometry for drawing. Therefore, some loss of ferromagnetic material seems unavoidable in order to maintain a good pin geometry.

By combining the M_{sat} results with the F_p measurements, the dependence of F_p on the Ni volume percentage remaining ferromagnetic can be observed (see Fig. 5.9); the trend shown is very promising. It is clear that a further increase of F_p may be possible with an increase in the volume of Ni in the wires. Wires with larger Ni volumes are currently being fabricated. However, the linear increase of F_p with Ni vol.% is not expected to continue indefinitely. Eventually, proximity effects from the ferromagnet will reduce the T_c and H_{c2} of the NbTi, so that the F_p will also be reduced. It is expected that F_p will reach an

optimum peak value for some Ni volume larger than 2% and then fall off for even larger Ni volumes. The goal of the future samples is to find the Ni vol.% that gives the maximum F_p. The optimum percentage will certainly be less than the optimum pin volume of 25% for nonmagnetic Niobium, although the exact optimum Ni volume probably cannot be predicted accurately.

5.3. The shape of F_p vs. B

The peak in F_p for our APC wires at optimum pin spacing occurred at lower fields (H_p ~ 2-3 T) than for conventional wires (H_p ~ 5 T ~ $0.5H_{c2}$; see Fig. 5.7). In fact, most APC wires at optimum pin spacing also have H_p ~ 2-3 T. This shift in H_p to lower fields can be understood as a result of the smaller pin number densities in our optimum wires. In optimized conventional wires, the pins are elongated Ti ribbons that are closely spaced (~ 3-6 nm) [Meingast (1989)]. In contrast, our APC wires had round pins (d_{pin} ~ 4 nm) with a larger optimum pin spacing (d_p ~ 30 nm). Since the maximum F_p is usually achieved when the pin and vortex densities (or spacings) are comparable, the peak in F_p will occur at lower fields (i.e., larger vortex lattice spacings) for the APC wires than for the conventional wires.

To approximate the dependence of F_p on B more quantitatively, a direct summation of pin strengths is assumed. Recall that in direct summation, $F_p = n_p f_p$, where n_p is the effective number of pins/unit volume and f_p is the force of one pin. One can define n_p = (vortices/unit area)(pins/unit vortex length). As B increases, the vortex spacing eventually becomes less than the pin spacing; when this occurs, a simple model of the vortex pin geometry shows the average number of pins/unit vortex length will decrease as $B^{-1/2}$ (see Fig. 5.10) . The vortices/unit area increase as B, so that $n_p \propto b^{1/2}$, where $b = B/H_{c2}$ and H_{c2} is the upper critical field of the superconductor. Assuming core pinning also gives $f_p \propto (1-b)$, which reflects the condensation energy loss as B approaches H_{c2}. Thus, it is

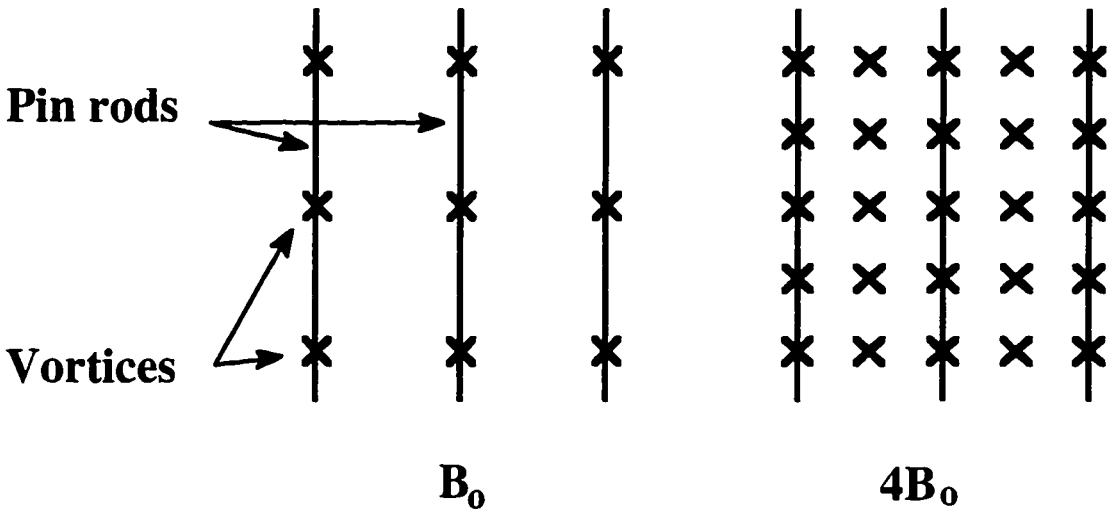

Fig 5.10. *A simple model to determine a quantitative form for the decrease in the number of pins on each vortex. At field B_0, the vortex and pin spacing are equal and each vortex sits on a pin. At field $4B_0$, one half of the vortices are not on pins, so that the average number of pins/ vortex has also decreased by one half. Therefore, the pins/vortex decrease as $B^{-1/2}$.*

expected that $F_p \propto b^{1/2}(1\text{-}b)$. A fit of this functional form for F_p to the data for wires A and C is shown in Fig. 5.5 and is quite good.

Within this analysis, as the pin density increases the dependence of F_p on B will approach the symmetrical shape of $F_p \propto b(1\text{-}b)$ observed for conventional wires, where because of the large pin densities, the pins/vortex length is constant. As shown in Fig. 5.11, this trend was indeed observed for wire C. The dotted lines are fits of $F_p \propto b^n(1\text{-}b)$ to the data where the exponent n is a fitting parameter. As d_p decreases and pin density increases, n is also increasing. Presumably, n would approach 1 if d_p decreased even further. (Wires with smaller d_p were not measured.) This trend of H_p shifting to higher fields (~ $0.5H_{c2}$) for increasing pin densities was also observed for other APC wires, as well [Cooley (1993), Heussner (1995), Heussner (1997a)].

The above analysis also requires there to be a increase in H_p when there is a increase in temperature. As the temperature is increased and H_{c2} is reduced, the dependence of F_p on B should again approach $F_p \propto b(1\text{-}b)$, since the pin spacing remains

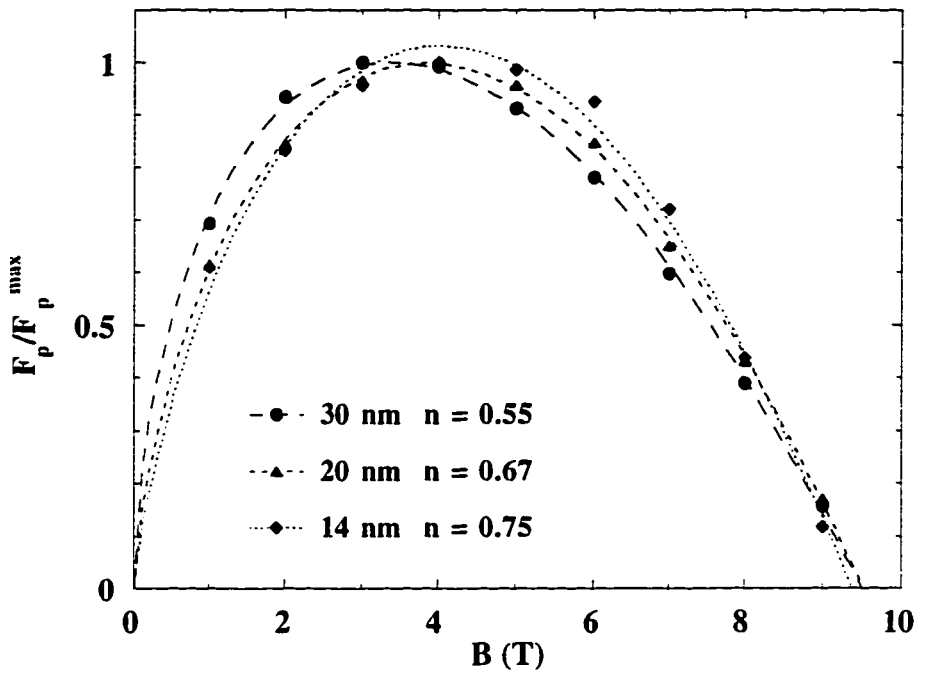

Fig. 5.11. *F_p/F_p^{max} vs. B for wire C at decreasing pin spacings d_p. F_p^{max} is the maximum in F_p as a function of field for a given d_p. The dotted lines are fits to the function $F_p = b^n(1-b)$, where n is a fitting parameter. The values of n are shown in the legend.*

constant but the vortex spacing is larger at lower fields. This general trend with temperature was observed in APC wires that had pins made of a $Nb_{0.98}Ti_{0.02}$ alloy [Cooley (1996)]. Measurements on our wires were made at 4.2 K only.

In deriving the form for $F_p \propto b^{1/2}(1-b)$, it was implicitly assumed that the vortices do not bunch up on the pins with spacing less than the equilibrium lattice spacing. This is probably a reasonable assumption, since a rough estimate of the elastic compression energy cost of bunching shows it to be much larger than the pinning energy gained from it. From Fig. 5.10, it is apparent that bunching would require a vortex to be displaced a distance a (the vortex lattice constant) from its equilibrium lattice position. Assuming that every other row of vortices will be displaced, the wavevector for the displacement will be $k = \pi/a$.

(See chapter 2 for a discussion of the vortex lattice elasticity.) Then using Eq. 2.16, the compression energy (E_{comp}) can be estimated to be:

$$E_{comp} \approx \frac{1}{2} C_{11}(a)^2 \left(\frac{\pi}{a}\right)^2 a^3 \approx \frac{B^2 a^5}{8\pi\lambda^2}(1-b) \tag{5.1}$$

where the volume for the compression was assumed to be V ~ a^3. The core pinning energy (E_{pin}) for a strong pin of dimension $d_{pin} = 2\xi$:

$$E_{pin} = \frac{H_{c2}^2}{16\pi\kappa^2}(2\xi)^3(1-b) \tag{5.2}$$

where we have used the relation $H_{c2} = (2)^{1/2}\kappa H_c$, in the expression for the condensation energy [Tinkham (1996)]. Comparing the two energies shows $E_{comp}/E_{pin} \sim (a/\xi)^5 >> 1$; It can be concluded that bunching is unlikely.

Of course, the previous analysis does not explain *why* the optimum pin spacings and sizes are larger in APC wires than in conventional wires. APC wires with nonmagnetic pins will not be discussed here. For our wires, it is not surprising that the optimum d_p is larger. The loss of ferromagnetic material with decreasing d_{pin} reduces the effective pin volume. Also, as is discussed next, ferromagnetic pins that are too closely spaced can significantly depress T_c and further reduce F_p .

5.4. Single Filament Measurements

In addition to determining the F_p of the total wires, transport measurements were made on single filaments of wire C to examine the basic superconducting properties of the NbTi in the presence of ferromagnetic pins. From these measurements, the perpendicular upper critical field H_{c2}(T), critical temperature T_c, and normal state resistivity ρ_N of the filaments were directly determined. In addition, the GL coherence length ξ and GL parameter κ were extracted using standard relations for type-II superconductors. Our results are compared with the standard values expected for $Nb_{0.36}Ti_{0.64}$.

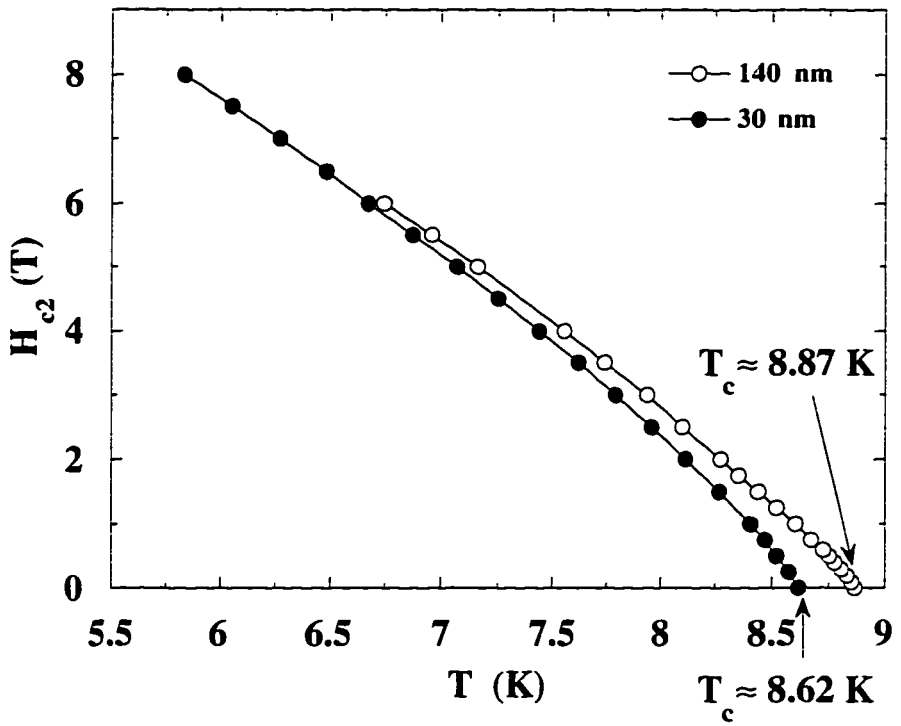

Fig. 5.12. *Upper critical field (H_{c2}) vs. temperature for single filaments of wire C at large pin spacing (d_p = 140 nm) and optimum pin spacing (d_p = 30 nm). The critical temperatures (T_c) are also shown.*

In Fig. 5.12, H_{c2} vs. T is shown for filaments with d_p = 30 nm and d_p = 140 nm. By using the slope dH_{c2}/dT near T_c and the measured value of ρ_N, the Ginzburg-Landau parameter κ was estimated using the following relation for dirty superconductors [Collings (1986)]:

$$\kappa = 35.4\left(-\rho_N \left.\frac{dH_{c2}}{dT}\right|_{T_c}\right)^{1/2} \tag{5.3}$$

where ρ_N is in units of Ω cm and the slope is in cgs units. For d_p = 140 nm, a least squares linear fit to the data near T_c yields dH_{c2}/dT = 2.91 T/K. From the measured I-V curve at T = 10 K, we have ρ_N = 36 μΩ cm. Therefore, we find that κ = 36. This value for κ is smaller than the typical value of κ ~ 50 for $Nb_{0.36}Ti_{0.64}$ [Meingast (1988)]. The lower value is probably due to the low value measured for ρ_N, which is much less than the standard value of $\rho_N \approx$ 60 μΩ cm for $Nb_{0.36}Ti_{0.64}$ [Meingast (1989)]. The presence of the

pins are probably the cause of the lower measured value for ρ_N. Since Cu and Ni have much lower bulk values of ρ_n than NbTi, the pins provide low resistance current paths in parallel with the high resistance NbTi, so that the average resistivity of the total filament is smaller than for homogeneous NbTi.

The zero temperature coherence length $\xi(0)$ can also be determined from the linear fit using the following relation for H_{c2} near T_c [Tinkham (1996)]:

$$H_{c2} = \frac{\Phi_o}{2\pi\xi(0)^2}\left(1 - T/T_c\right) \tag{5.4}$$

Again, for d_p = 140 nm we have $\xi(0) \approx 3.4$ nm. This value estimated for $\xi(0)$ is comparable to the standard values measured for homogeneous cold-worked $Nb_{0.36}Ti_{0.64}$ [Collings (1986)]. (κ and ξ are not estimated for d_p = 30 nm since the closely spaced pins are significantly affecting the slope of H_{c2} near T_c, as well as depressing T_c.) In Table 5.2, the normal state resistivity and superconducting properties of the filament with d_p = 140 nm are compared with those of homogeneous bulk NbTi.

5.4.1. Proximity Effect Reduction of T_c and H_{c2}

Although T_c for d_p = 140 nm is close to the standard value of $T_c \approx 9$ K for $Nb_{0.36}Ti_{0.64}$, the T_c for d_p = 30 nm is being depressed from the bulk value by the closely spaced ferromagnetic pins (see Fig. 5.12). The observed T_c reduction can be compared to the theoretical prediction given by Jin and Ketterson (1989) for the case of a superconducting slab of thickness d_s sandwiched between two slabs of ferromagnet. For temperatures near T_c, the order parameter ψ is small so that the linearized form of the 1st GL equation (Eq. 2.3) may be used (with zero magnetic field):

$$\frac{\hbar^2}{4m}\left(\frac{\partial^2\psi(x)}{\partial x^2}\right) = \alpha(T)\psi(x) \tag{5.5}$$

The order parameter is assumed to be pulled to zero by the ferromagnet at $x = \pm d_s/2$. Subject to this boundary condition, Eq. 5.5 has the solution $\psi(x) = A\ cos\ (kx)$ and the

Table 5.2. *The normal state resistivity and superconducting properties of a single filament of wire C at large d_p compared to the properties of homogeneous bulk $Nb_{0.36}Ti_{0.64}$.*

	ρ_N (μΩ cm)	κ	$\xi(0)$ (nm)	T_c (K)
d_p = 140 nm	36	36	3.4	8.87
$Nb_{0.36}Ti_{0.64}$	60	50	3.6	9

following relation for *k*::

$$k^2 = \frac{n^2\pi^2}{d_s^2} = \frac{4m\alpha}{\hbar^2}(T_{c0} - T) \tag{5.6}$$

where n is an integer and we have explicitly written the temperature dependence for α(T), so that α is a temperature independent constant. T_{c0} is the bulk critical temperature in the absence of the ferromagnet.

The new critical temperature T_c is the temperature that has the smallest nonzero temperature difference from T_{c0}, and for which a solution ψ(x) exists. Taking n = 1 in Eq. 5.6 and defining $T = T_c$ yields:

$$T_c / T_{c0} = 1 - \left(\frac{\pi\xi(0)}{d_s}\right)^2 \tag{5.7}$$

where the definition of the zero temperature GL coherence length $\xi(0)$ has been used. Hence, a 15% drop in T_c is predicted for d_s = 30 nm and using $\xi(0)$ = 3.5 nm, much larger than the 3% drop in T_c that was actually observed in wire C at a comparable pin spacing.

The smaller observed reduction in T_c is not surprising for several reasons. In the wire cross-section, there is a 2-dimensional array of point pins compared to the planes of ferromagnet considered in the model. Therefore, in the wires the order parameter is depressed over a smaller fraction of the superconductor, so that the T_c reduction is also less. Unfortunately, this 2-d system is also more difficult to solve analytically. In addition, in deriving Eq. 5.7, it was assumed that ψ was exactly zero at the superconductor boundary. This assumption probably is not accurate for our ferromagnetic pins, since the

Table 5.3. *Results of T_c and H_{c2} measurements for wires A and C compared with the reference values for bulk homogeneous $Nb_{0.36}Ti_{0.64}$. T_c was measured resistively using single filaments of the wires (see sec. 4.3). H_{c2} was extracted from fits of $F_p \propto b^{1/2}(1-b)$ to the F_p vs. B data (see sec 5.3).*

	d_p (nm)	T_c (K)	H_{c2} (T)
Wire C	140	8.87	--
Wire C	30	8.62	9.6
Wire A	28	--	10.4
$Nb_{0.36}Ti_{0.64}$	--	9	11

pin thickness is $d_{pin} \sim 4$ nm, and ψ can penetrate a distance $\xi_{Ni} \sim 1$ nm into the pin (see Fig. 2.2).

H_{c2}(4.2K) was also depressed for $d_p \approx 30$ nm, compared to the reference value of H_{c2}(4.2K) $\approx$ 11 T for homogeneous $Nb_{0.36}Ti_{0.64}$ [Meingast (1989)]. H_{c2} was extracted from the fit of $F_p \propto b^{1/2}(1-b)$ to the F_p vs. B data for wire C, yielding H_{c2} (4.2K) $\approx$ 9.6 T. A similar fit to the F_p data for wire A gave H_{c2}(4.2K) $\approx$ 10.4 T, The smaller value of H_{c2} for wire C is consistent with its larger value of Ni remaining ferromagnetic: the superconducting order parameter is more fully depressed by the pins and hence H_{c2} is reduced more from the larger loss of condensation energy.

The results of the T_c and H_{c2} measurements for wires A and C are summarized in Table 5.3. The reduction of T_c and H_{c2} was relatively small for these wires with 2% Ni at optimum pin spacing. This suggests that slightly larger amounts of Ni should not cause severe drops in T_c or H_{c2}, and, as shown previously (see Fig. 5.9), should give enhanced F_p.

Chapter 6. Conclusions

6.1. Summary of Results

Ferromagnetic artificial pinning centers were used to increase the J_c of superconducting NbTi wires. The large values of J_c that were achieved with a relatively small ferromagnetic pin volume ($\approx 2\%$) indicate that ferromagnetic pins are more effective than nonmagnetic pins for a given volume percent. Although there has been some previous research on the pin strength of a ferromagnet in a type-II superconductor, this thesis research has resulted in the first direct observation of the difference between the effectiveness of magnetic and nonmagnetic pin materials. This greater effectiveness of the ferromagnet is understood as a result of its strong suppression of superconductivity, so that even a small ferromagnetic pin produces a large *effective* pin volume.

Magnetization measurements on the wires have also indicated that an increase in J_c correlates with an increase in the volume of Ni remaining ferromagnetic in the wires. Transport measurements on single filaments of the optimum wire with Ni pins showed that the proximity effect depression of T_c and H_{c2} was fairly small. These results indicate that wires with a moderate increase in the Ni volume might not have severe proximity effects, and may have even larger values of J_c (particularly at lower fields, away from H_{c2}).

The optimum wires with large superconducting filaments had the peak in the F_p vs. B curve at lower fields than for optimized conventional wires. The peak shifted to higher fields for smaller pin spacing. This trend is interpreted as an effect of the optimum pin spacing being larger in our APC wires than that of conventional wires. A simple theoretical argument gives the approximate form $F_p \propto b^{1/2}(1\text{-}b)$ for APC wires with pin spacing near optimum ($d_p \sim 30$ nm). This functional form fits the F_p data for our wires quite well.

Wires with small superconducting filaments displayed additional pinning at low fields in addition to that observed for large filament wires with identical APC

nanostructure. The additional pinning is attributed to the interfaces between the Cu and the NbTi filaments. The pinning mechanism is understood as a Bean-Livingston type surface barrier [Bean (1966), Mawatari (1994), Takacs (1988), Clem (1974)]; the magnitude of the surface pinning is in agreement with that predicted by a simple model system [Clem (1974)].

Finally, a reliable method was developed to produce the APC wires with ferromagnetic pins. The processing consisted of a standard restack and draw procedure, to which were added some modifications to improve wire drawability. Hot processing, including HIPs and hot extrusions, were used to establish good bonding between the wire elements. A good wire geometry was maintained by reducing the local ration of Cu to harder material (such as NbTi or Ni). In addition, high reduction dies were used to minimize strength differences between the hard NbTi and the soft Cu. The end result of these changes the creation of a fairly robust process for making APC wires, in general.

6.2. Future APC designs

There are possibilities for future APC designs that not only might further enhance J_c, but also might enhance the general understanding of the physics of pinning. The results of this thesis have indicated several promising possibilities for new APC wire designs that could further enhance J_c. As mentioned previously, samples with larger amounts of Ni should increase J_c and are currently being made. It may also be possible to enhance J_c using the size effect that gave additional surface pinning. Independent of the thesis results, a nonmagnetic dirty alloy is also an interesting possibility as a new pin material. The latter two possibilities for new pin designs are further discussed below.

One route to enhancing J_c may be through the surface pinning that occurs for small NbTi filaments. In Fig. 6.1, F_p vs. B is shown for two wire samples: one with submicron NbTi filaments surrounded by Cu and one with comparably sized filaments surrounded by

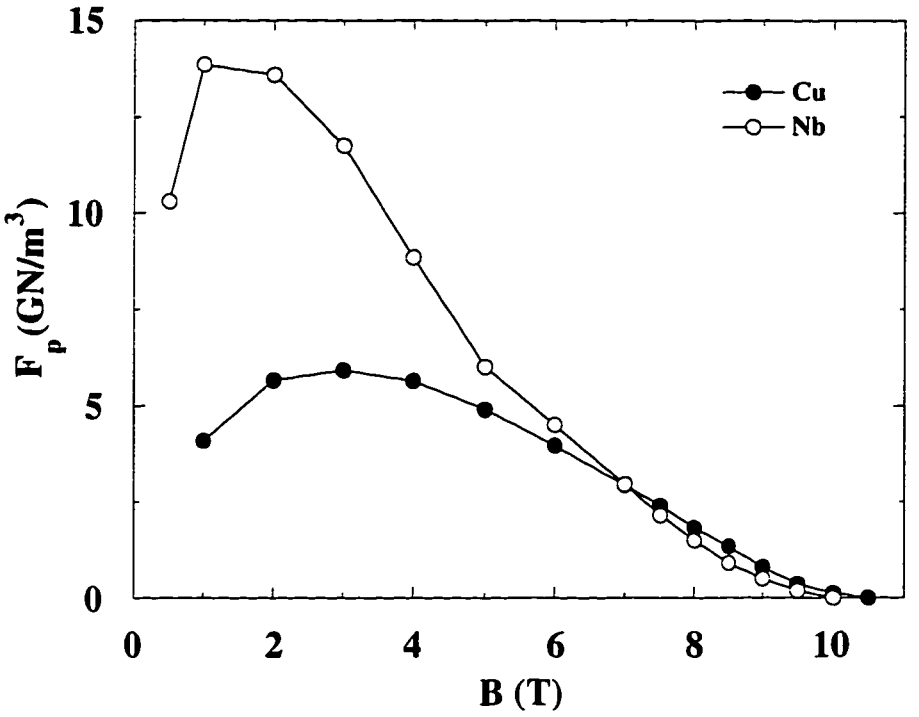

Fig. 6.1. *F_p vs. B for small NbTi filaments (d_{fil} = 0.1 μm) surrounded by either Cu or Nb. The Cu and Nb were both approximately 25% of the total area of NbTi and normal metal. Data courtesy of Dr. L.R. Motowidlo, IGC-Advanced Superconductors.*

Nb. The NbTi is heavily cold-worked in both wires and contains no additional pinning centers other than grain boundaries. The Cu and Nb volumes (25%) are approximately the same as in our small filament wires. The magnitude of F_p for the Cu matrix is comparable to the enhancement in F_p observed for our small filament wires. The larger F_p for Nb might be due to its shorter coherence length (ξ_{Nb} ~ 15 nm) creating a sharper interface between the superconducting and normal region. However, complications from the low field superconductivity of cold-worked Nb are not ruled out as a possible cause of the larger F_p. In any case, it can be concluded that the magnitude of the surface pinning is significantly larger for small NbTi filaments surrounded by Nb rather than Cu.

The additional benefit of using Nb is that its mechanical properties are more compatible with NbTi than are those of Cu. Most filaments in industrially produced NbTi

wires are several microns in diameter. Submicron filaments are difficult to make in long lengths because variations in the small filament diameter (sausaging) cause breaks. The mismatch of strength between Cu and NbTi creates nonuniformity during drawing that could increase the likelihood for a variation in diameter. Such variations would probably be less for filaments surrounded by Nb whose cold-worked strength is closer to that of NbTi.

The possibility then exists that the total bundle of submicron NbTi filaments in Nb could behave as a single large filament, but with the enhanced F_p of the small filaments. If APCs are then added to the NbTi, the F_p could be very large, particularly at lower fields, where large filament APC wires already display large F_p. In the best case scenario, the contribution from the surface pinning would add to the pinning from the APCs. Since large filament Nb island-type APCs have achieved $F_p \sim 30$ GN/m^3 at 2-3 T, it may be possible to increase the F_p to as much as 40 GN/m^3 by using the surface pinning effect. Samples are currently being made to test these ideas.

Another interesting APC design to try would be using a nonmagnetic dirty alloy as the pin material. Previous pin materials have usually been either pure metals (e.g., Nb, Ti or V) whose coherence lengths are relatively long ($\xi_N \geq 20$ nm), or in the case of this thesis, a ferromagnet whose coherence is very short ($\xi_{FM} \sim 1$ nm). It would be of technological interest to determine the magnitude of J_c that can be produced by using pin materials whose ξ_N are between the pure metal and ferromagnet limits. In addition to possibly increasing J_c, the effect of ξ_N on pin strength could also be more closely examined, which would also be of general physical interest. A nonmagnetic dirty alloy can have a ξ_N that is between the ferromagnetic and pure metal limits. For example, $Cu_{0.70}Ni_{0.30}$ has $\rho_N = 36$ μΩ cm [Fickett (1983)] and an electronic specific heat of $\gamma = 4230$ erg/cm^{3}K^2 [Schroder (1961)], so that using Eq. 2.20 yields $\xi_N \approx 7$ nm.

By comparing with the estimate of $\xi_N \approx 20$ nm for Ti that had $\rho_N = 5$ μΩ cm and $\gamma = 3150$ erg/cm^{3}K^2, one can see that the main source of the smaller ξ_N for CuNi is the much

larger ρ_N, i.e. the shorter electronic mean free path. Hence, the distance that the superconducting electron pairs can penetrate into the pin before being scattered and broken apart is shorter in the dirty alloy than in the pure metal. However, if the alloy is nonmagnetic, usually ξ_N will still be larger than ξ_{FM} for a ferromagnet, where the magnetic exchange energy is a very strong pairbreaker (See sec. 2.2.2 and 2.2.3).

It turns out that CuNi is an excellent choice for a pin material that is a nonmagnetic dirty alloy. In general, CuNi alloys have excellent ductility which is a prerequisite for any pin material, given the extensive wire drawing that is required. In addition, a range of nonmagnetic CuNi alloys are commercially available, from $Cu_{0.90}Ni_{0.10}$ to $Cu_{0.60}Ni_{0.40}$ (commonly known as Constantan), so that the pin strength for a range of ξ_N may be examined. For these compositions, ρ_N increases from 10 $\mu\Omega$ cm for $Cu_{0.90}Ni_{0.10}$ to 50 $\mu\Omega$ cm for $Cu_{0.60}Ni_{0.40}$ [Fickett (1983)]. Therefore, assuming γ is approximately constant for the different compositions, ξ_N can be varied from approximately 13 nm down to 6 nm. (In fact, γ increases slightly with increasing Ni % over this range [Touloukian (1970)], so that the range of possible ξ_N is actually slightly larger.) Given the well established drawability of $Cu_{0.70}Ni_{0.30}$ [Ozeryansky (1996)], a wire containing APCs of this composition is currently being made as a starting point for the study of the CuNi system.

6.3. Coda

The nature of this thesis research was probably not typical. In addition to measuring the wires and developing experimental techniques at Yale, I also had to spend a good deal of time at IGC making the wires. When this project began, I (along with probably everyone else at Yale) had absolutely no idea how to successfully make an APC wire. I began to work on the factory floor at IGC and made several poor attempts and subsequent failures at making a wire. I eventually decided to use the resources around me and began to ask the engineers and scientists (mainly G.A. Ozeryansky and Dr. L.R.

Motowidlo) questions about the fine art of wiremaking; The result was that I learned not only how to successfully make a wire, but also how research was conducted in an industrial environment. The combination of working and learning both at IGC and at Yale -- in industry and in academia -- has given me invaluable experience as a researcher.

Appendix A. Determining the Superconductor Volume Percentage and Pin Volume Percentage

The percentage of superconductor (with the pin percentage included) in the final wires was determined using an etch and weigh technique. This technique consists of weighing a length of wire, removing the Cu in a H_20:$HN0_3$ solution, and then weighing the remaining filaments. The weight before (W_B) and after (W_A) etching can be related to the NbTi and pin area through the following formulas:

$$L\left(\rho_{NbTi}A_{NbTi}+\rho_{pin}A_{pin}+\rho_{Cu}A_{Cu}\right)=W_B \tag{A.1}$$

$$L\left(\rho_{NbTi}A_{NbTi}+\rho_{pin}A_{pin}\right)=W_A \tag{A.2}$$

where ρ designates density, A is area, and L is the length of the wire that was cut. After some algebraic manipulation, one gets the following formula for the ratio of superconductor area ($A_{SC}=A_{NbTi}+A_{Cu}$) to Cu area:

$$\delta=\frac{A_{SC}}{A_{Cu}}=\left(\frac{W_B}{W_A}-1\right)^{-1}\left(\frac{\rho_{NbTi}(1-\beta)+\rho_{pin}(\beta)}{\rho_{Cu}}\right)^{-1} \tag{A.3}$$

where $\beta=A_{pin}/A_{SC}$ is the fractional pin volume in the wire. Then the superconductor percentage in the wire is $SC = 100(\delta/(1+\delta))$. These formulas generalizes in an obvious way for wires with multiple types of pins.

Obviously, these formulas rely on accurately knowing the pin volume percentage in the wires. The ferromagnetic pin percentage was also needed to calculate M_{sat}. The pin percentage for the gun-drilled pins could be determined accurately from the dimensions of the initial billet assembly that had one round pin filling a round hole. In contrast, the interstitial pins did not totally fill the interstitial spaces between the rods, making the actual pin percentage more difficult to predict after compaction during HIP and extrusion. To determine the actual pin percentage for the interstitial wires, a cut and weigh technique was used. An optical microscope was used to take a picture of the first stack cross-section after extrusion. The picture was copied and enlarged using a photocopier. Then the pin rods

and NbTi rods were cut out of the picture separately and weighed. Thus, the ratio of the pin area to the total filament area was determined.

Appendix B. Cleaning During Wire Processing

Several different methods were used to create clean oxide-free surfaces on the materials during wire processing. Rough cleaning was usually done by rubbing Scotch-brite abrasive sponge over the surface. For the post-extrusion cleaning of Cu, a sand-blaster was very effective in removing the extrusion grease and oxidation. For smaller scale grease and particulate removal, the materials were placed in an ultrasonic bath of Microclean soap and water, followed by a bath of Acetone, followed by a bath of Isopropanol. The final cleaning step was always a chemical etch of the materials to remove any remaining oxides and dirt, and to roughen the surfaces for enhanced bonding. The etching solutions used for the different materials are listed below (all water was hot):

Nb or NbTi $\Rightarrow$ H_20:HNO_3:HF 3:1:1

Cu or Ni: $\Rightarrow$ H_20:HNO_3 between 1:1 to 1:2

Fe $\Rightarrow$ HCl:H_20 1:1

References

Alden, T.H. and J.D. Livingston,"Ferromagnetic Particles in a Type-II Superconductor," J. Appl. Phys. **37**, 3551 (1966).

Ashcroft, N.W., and N.D. Mermin, *Solid State Physics*, (Holt, Rinehart and Winston, Orlando, FL, 1976).

Autler, S.H.,"Fluxoid Pinning in Superconductors by a Periodic Array of Magnetic Particles," J. Low Temp. Phys. **9**, 241 (1972).

Avitzur, B., *Handbook of Metal Forming Processes*, (Wiley and Sons, New York, 1983).

Bean, C.P., and J.D. Livingston,"Surface Barrier in Type-II Superconductors," Phys. Rev. Lett. **12**, 14 (1964).

Brandt, E.H.,"Elastic Energy of the Vortex State in Type-II Superconductors. I. High Inductions," J. Low Temp. Phys. **26**, 709 (1977a).

Brandt, E.H.,"Elastic Energy of the Vortex State in Type-II Superconductors. II. Low Inductions," J. Low Temp. Phys. **26**, 735 (1977b).

Brandt, E.H.,"Elastic and plastic properties of the flux-line lattice in type-II superconductors," Phys. Rev. B **34**, 6514 (1986).

Brongersma, S.,"Vortex configurations in superconducting films and multilayers," Ph.D. thesis, Vrije Universiteit, (1996).

Campbell, A.M., and J.E. Evetts,"Flux Vortices and Transport Currents in Type-II Superconductors," Adv. Phys. **21**, 199 (1972).

Clem, J.R.,"A model for flux pinning in superconductors," in *Low Temperature Physics-LT 13*, K.D Timmerhaus, W.J. O'Sullivan, and E.F. Hammel, eds. (Plenum, New York, 1974), Vol 3., p. 102.

Collings, E.W., *A Sourcebook of Titianium Alloy Superconductivity* (Plenum Press, New York, 1983a), Vol. 1.

Collings, E.W., *A Sourcebook of Titianium Alloy Superconductivity* (Plenum Press, New York, 1983b), Vol. 2.

Cooley, L.D., P.D. Jablonski, P.J. Lee, and D.C. Larbalestier,"Strongly enhanced critical current density in Nb47wt%Ti having a highly aligned microstructure," Appl. Phys. Lett. **58**, 2984 (1991).

Cooley, L.D.,"The Scaling Rule and Fluxon Core Pinning in a High Field Superconductor with Artificially Introduced Pins," Ph.D. thesis, University of Wisconsin (1993).

Cooley, L.D., P.J. Lee, and D.C. Larbalestier,"Flux-Pinning mechanism of proximity-coupled planar defects in conventional superconductors: Evidence that magnetic pinning is the dominant pinning mechanism in niobium-titanium alloy," Phys. Rev. B **53**, 6638 (1996).

Cooley, L.D, P.D. Jablonski, R.W. Heussner, and D.C. Larbalestier,"Nb-Ti Composite wires with Artificial Ferromagnetic Pins," Adv. Cryo. Eng.(Mat.) **42**, 1095 (1996).

Dalrymple, B.J., Ph.D. thesis, Yale University (1987).

de Gennes, P.G., *Superconductivity of Metals and Alloys*, (W.A. Benjamin, New York (1966), reprinted by Addison-Wesley, New York, (1989)).

Dorofejev, G.L., E.Y. Klimenko, S.V. Frolov, E.V. Nikolenkov, E.I. Plashkin, N.T. Salunin, and V.Y. Filkin,"Current-carrying capacity of superconductors with artificial pinning centers," in *Proceedings of 9th International Conference on Magnet Technology*, eds. C. Marinucci and P. Weymuth (Swiss Inst. for Nuc. Res., Switzerland, 1985), p. 564.

Fickett, F.R., "Electrical Properties," in *Materials at Low Temperatures*, eds. R.P.Reed and A.F. Clark (Am. Soc. Met., Metals Park, Ohio, 1983), p.163.

Ginzburg, V.L., and L.D. Landau,"On the Theory of Superconductivity," Zh. Eksp. Teor. Fiz. **20**, 1064 (1950).

Gurevich, A. and L.D. Cooley,"Anisotropic flux pinning in a network of planar defects," Phys. Rev. B **50**, 13563 (1994).

Hauser, J.J., H.C. Theuerer, and N.R. Werthamer,"Proximity Effects between Superconducting and Magnetic Films," Phys. Rev. **142**, 118 (1966).

Heussner, R.W., P.D. Jablonski, P.J. Lee, and D.C. Larbalestier,"Properties of Rod-Based Artificial Pinning Center Nb-Ti Superconductors," IEEE Trans. Appl. Supercond. **5**, 1705 (1995).

Heussner, R.W., C. Bormio-Nunes. L.D. Cooley, and D.C. Larbalestier,"Artificial Pinning Center Nb-Ti Superconductors with Alloyed Nb Pins," to appear, IEEE Trans. Appl. Supercond., (1997a).

Heussner, R.W., C. Bormio-Nunes. L.D. Cooley, and D.C. Larbalestier,"Increased critical current density in Nb-Ti wires having Nb artificial pinning centers," Appl. Phys. Lett. **70**, 901 (1997b).

Hosford, W.F.,"Microstructural Changes During Deformation of [011] Fiber-Textured Metals," Trans. Metall. Soc. (AIME) **230**, 12 (1964).

Jablonski, P.D., P.J. Lee, and D.C. Larbalestier,"Development and Characterization of Artificial Microstructures in Long Lengths of Superconducting Wire," Mat. Res. Soc. Symp. Proc. **351**, 455 (1994).

Jin, B.Y. and J.B. Ketterson,"Artificial metallic superlattices," Adv. Phys. **38**, 189 (1989).

Kittel, C., *Introduction to Solid State Physics*, 6th edition (Wiley and Sons, New York, 1986).

Koch, C.C., and G.R. Love,"Superconductivity in Niobium Containing Ferromagnetic Gadolinium or Paramagnetic Yttrium Dispersions," J. Appl. Phys. **40**, 3582 (1969).

Koorevaar, P., Y. Suzuki, R. Coehoorn, and J. Aarts,"Decoupling of superconducting V by ultrathin Fe layers in V/Fe multilayers," Phys. Rev. B **49**, 441 (1994).

Koorevaar, P., R. Coehoorn, and J. Aarts,"Critical fields in vanadium-based superconducting/ferromagnetic multilayers," Physica C **248**, 61 (1995).

Landau, L.D., and E.M. Lifshitz, *Theory of Elasticity*, 3rd edition (Pergamon Press, New York, 1986).

Lee, J.A., D. Armstrong, P.E. Madsen, J.P. Charlesworth, and R.F. Hills, UK Patent Appplication 2038532, filed 1978.

Lee P.J., J.C. McKinnell and D.C. Larbalestier,"Restricted, Novel Heat Treatments for Obtaining High J_c in Nb46.5wt%Ti," Adv. Cryo. Eng. (Mat.), **36**, 287 (1990).

Lee P.J., J.C. McKinnell and D.C. Larbalestier,"Restricted Novel Heat Treatments for Obtaining High J_c in Nb46.5wt%Ti: II. Prestrain Dependence," Adv. Cryo. Eng. (Mat.), **40**, 725 (1994).

Matsumoto, K., H Takewaki, Y. Tanaka, O. Miura, K Yamafuji, K. Funaki, M. Iwakuma, and T. Matsushita,"Enhanced J_c properties in superconducitng NbTi composites by introducing Nb artificial pins with a layered structure," Appl. Phys. Lett. **64**, 115 (1994).

Matsushita, T.,"Elementary pinning force of normal precipitates in a superconductor," J. Appl. Phys. **54**, 281 (1983).

Mawatari, Y., and K. Yamafuji,"Critical current density in thin films due to the surface barrier," Physica C **228**, 336 (1994).

McCambridge, J.D.,"The Superconducting Properties of Niobium-Titanium Alloy Multilayers," Ph.D. thesis, Yale University (1995).

Meingast, C.,"Flux Pinning by ΔH_c and $\Delta\kappa$ mechanisms in Niobium-Titianium Superconductors," Ph.D. thesis, the University of Wisconsin - Madison (1988).

Meingast, C., P.J. Lee and D.C. Larbalestier,"Quantitative description of a high J_c Nb-Ti superconductor during its final optimization strain: I. Microstructure, T_c, H_{c2}, and resistivity,"J. Appl. Phys. **66**, 5971 (1989a).

Meingast, C. and D.C. Larbalestier,"Quantitative description of a very high critical current density Nb-Ti superconductor during its final optimization strain: II. Flux pinning mechanisms," J. Appl. Phys. **66**, 5962 (1989b)

Motowidlo, L.R., B.A. Zeitlin, M.S. Walker, and P. Haldar,"Multifilamentary NbTi with artificial pinning centers: the effect of alloy and pin material on the superconducting properties," Appl. Phys. Lett. **61**, 991 (1991).

Motowidlo, L.R., B.A. Zeitlin, M.S. Walker, P. Haldar, J.D. McCambridge, N.D. Rizzo, X.S. Ling, and D.E. Prober,"Multifilamentary NbTi with artificial pinning centers: the effect of alloy, pin material and geometry on the superconducting properties," IEEE Trans. Appl. Supercond. **3**, 1366 (1993).

Ozeryansky, G.M., Private Communications, IGC-Advanced Superconductors, 1875 Thomaston Ave., Waterbury, CT, 06704 (1996).

Peck, J.F., and D.A. Thomas,"A Study of Fibrous Tungsten and Iron," Trans. Metall. Soc. (AIME) **221**, 1240 (1961).

Radovic, Z., L. Dobrosavljevic-Grujic, A.I. Buzdin, and J.R. Clem,"Upper critical fields of superconductor ferromagnet multilayers," Phys. Rev. B **38**, 2388 (1988).

Radovic, Z., M. Ledvij, L. Dobrosavljevic-Grujic, A.I. Buzdin, and J.R. Clem,"Transition temperatures of superconductor ferromagnet superlattices," Phys. Rev. B **44**, 759 (1991).

Rizzo, N.D., J.Q. Wang, D.E. Prober, L.R. Motowidlo, and B.A. Zeitlin,"Ferromagnetic artificial pinning centers in superconducting $Nb_{0.36}Ti_{0.64}$ wires," Appl. Phys. Lett. **69**, 2285 (1996).

Rudziak, M.K., J.M. Seuntjens, C.V. Renaud, T. Wong, and J. Wong,"Development of APC Nb-Ti Composite Conductors at Supercon, Inc.," IEEE Trans. Appl. Supercond. **5**, 1709 (1995).

Saint-James, D., G. Sarma, and E.J. Thomas, *Type-II Superconducitvity*, (Pergamon Press, Oxford, 1969).

Schroder, K.,"Effect of Magnetic Clusters on the Specific Heat of Ni-Cu and Fe-V Alloys," J. Appl. Phys. **32**, 880 (1961).

Stejic, G., A. Gurevich, E. Kadyrov, D. Christen, R. Joynt, and D.C. Larbalestier,"Effect of geometry on the critical current of thin films," Phys. Rev. B **49**, 1274 (1994).

Taillard, R., J. Foct, C.E. Bruzek, and Hoang-Gia-Ky,"Mechanisms of formation of intermetallic compounds at the interface of niobium-shielded filaments," IEEE Trans. Appl. Supercond. **3**, 1346, (1993).

Takács S.,"Properties of Superfine Superconducting Filaments Embedded in Normal Matrix," Czech. J. Phys. B **36**, 524 (1986).

Takács S.,"Pinning force in thin superconductors with small number of flux-line rows," Czech. J. Phys. B **38**, 1050 (1988).

Ternovskii, F.F. and L.N. Shekhata,"Structure of the Mixed State Near the Boundary of a Semi-Infinite Type-II Superconductor of the Second Kind," Sov. Phys. JETP **35**, 1202 (1972).

Thornton, P.A., and V.J. Colangelo, *Fundamentals of Engineering Materials*, (Prentice-Hall Inc., Englewood Cliffs, New Jersey, 1985).

Tinkham, M., *Introduction to Superconductivity*, 2nd edition. (McGraw Hill, New York, 1996).

Touloukian, Y.S., and E.H. Buyco, *Thermophysical Properties of Matter, vol. 4: Specific Heat -- Metallic Elements and Alloys*, (Plenum, New York, 1970).

Wang. J.Q., N.D. Rizzo, D.E. Prober, L.R. Motowidlo, and B.A. Zeitlin,"Flux Pinning in Multifilamentary Superconducting Wires with Ferromagnetic Artificial Pinning Centers," to appear in IEEE Trans. Appl. Supercond. (1997).

Yetter, W.E., E.J. Kramer, and D.G. Ast,"Flux Pinning by Thin Chromium Layers," J. Low Temp. Phys. **49**, 227 (1982).